KIZILTEPE LOW-SULPHIDATION EPITHERMAL DEPOSIT (SINDIRGI, BALIKESİR): AN EXAMPLE FOR RELAY-RAMP-HOSTED EPITHERMAL GOLD MINERALIZATION IN WESTERN TURKEY

A THESIS SUBMITTED TO
THE GRADUATE SCHOOL OF NATURAL AND APPLIED SCIENCES
OF
MIDDLE EAST TECHNICAL UNIVERSITY

BY

BERKİN UĞURLU

IN PARTIAL FULFILLMENT OF THE REQUIREMENTS
FOR
THE DEGREE OF MASTER OF SCIENCE
IN
GEOLOGICAL ENGINEERING

SEPTEMBER 2019

Approval of the thesis:

KIZILTEPE LOW-SULPHIDATION EPITHERMAL DEPOSIT (SINDIRGI, BALIKESİR): AN EXAMPLE FOR RELAY-RAMP-HOSTED EPITHERMAL GOLD MINERALIZATION IN WESTERN TURKEY

submitted by **BERKİN UĞURLU** in partial fulfillment of the requirements for the degree of **Master of Science in Geological Engineering Department, Middle East Technical University** by,

Prof. Dr. Halil Kalıpçılar
Dean, Graduate School of **Natural and Applied Sciences**   _____

Prof. Dr. Erdin Bozkurt
Head of Department, **Geological Engineering**   _____

Prof. Dr. Erdin Bozkurt
Supervisor, **Geological Engineering, METU**   _____

Examining Committee Members:

Prof. Dr. Gürol Seyitoğlu
Geological Engineering Dept., Ankara University   _____

Prof. Dr. Erdin Bozkurt
Geological Engineering, METU   _____

Assoc. Prof. Dr. Erman Özsayın
Geological Engineering Dept., Hacettepe University   _____

Assist. Prof. Dr. Ulaş Avşar
Geological Engineering Dept., METU   _____

Assist. Prof. Dr. Selman Aydoğan
Geological Engineering Dept., Balıkesir University   _____

Date: 12.09.2019

I hereby declare that all information in this document has been obtained and presented in accordance with academic rules and ethical conduct. I also declare that, as required by these rules and conduct, I have fully cited and referenced all material and results that are not original to this work.

Name, Surname: BERKİN Uğurlu

Signature:

ABSTRACT

KIZILTEPE LOW-SULPHIDATION EPITHERMAL DEPOSIT (SINDIRGI, BALIKESİR): AN EXAMPLE FOR RELAY-RAMP-HOSTED EPITHERMAL GOLD MINERALIZATION IN WESTERN TURKEY

Uğurlu, BERKİN
Master of Science, Geological Engineering
Supervisor: Prof. Dr. Erdin Bozkurt

September 2019, 138 pages

Kızıltepe, located 50 km southeast of Balıkesir in western Turkey, has a long history of precious metal mining back to 2000 years and hosts numerous low sulfidation epithermal quartz veins. In the modern times, subsequent to 25 years of mineral exploration activities, first gold silver mining operation has started on the vein sector called Arzu South in 2017, and 3 other sectors; Arzu North, Derya and Banu on the line.

Kızıltepe low sulfidation epithermal gold mineralization is hosted by early Miocene dacitic volcanics/volcanoclastics and directly associated with the recent extensional tectonic regime of western Turkey.

The study of the stress field orientations based on the available fault surfaces identified 3 domains; (A) E–W- trending northern boundary faults, (B) southern boundary faults and (C) NW–SE-trending normal faults observed in Arzu South open pit.

Relative sense of motion of the blocks are studied by utilizing the orientation data of the fault plains and paleostress analysis are performed to determine the tectonic stress. The interpretation of all the results suggest to characterize Kızıltepe deposit as a relay ramp hosted epithermal gold mineralization.

ÖZ

KIZILTEPE DÜŞÜK SÜLFİDASYON ALTIN YATAĞI (SINDIRGI, BALIKESİR): AKTARIM YOKUŞUNA YERLEŞMİŞ EPİTERMAL ALTIN CEVHERLEŞMESİNE BATI ANADOLU'DAN BİR ÖRNEK

Uğurlu, BERKİN
Yüksek Lisans, Jeoloji Mühendisliği
Tez Danışmanı: Prof. Dr. Erdin Bozkurt

Eylül 2019, 138 sayfa

Balıkesir'in 50 km güneydoğusunda bulunan Kızıltepe sayısız düşük sülfidasyon epitermal kuvars Damarına ev sahipliği yapar ve madencilik tarihi günümüzden 2000 yıl öncesine dayanır. 25 yıla yakın süren arama faaliyetlerinin sonunda ilk modern altın gümüş maden işletmesi Arzu Güney Damarı üzerinde 2017 yılında üretime başlamıştır ve Arzu Kuzey, Derya ve Banu Damarları üretim için sırasını beklemektedir.

Kızıltepe düşük sülfidasyon epitermal altın cevherleşmesi Miyosen yaşlı dasitik volkanik ve volkanoklastik birimleri içerisinde batı Anadolu'yu etkisi altında bırakan gerilme tektonizmasına bağlı gelişmiştir.

Mevcut fay yüzeylerinin kuvvet yönlerinin çalışılmasıyla 3 alan belirlenmiştir; (A) kuzeyi sınırlayan D–B-uzanımlı normal faylar, (B) güneyi sınırlayan D–B-uzanımlı normal faylar ve (C) Arzu Güney açık ocağında gözlenen KB–GD-uzanımlı normal faylar.

Fay yüzeylerinden toplanan verilerle blokların bağıl hareket yönü çalışılmış, tektonik kuvvetlerin belirlenmesi için paleostres analizleri yapılmıştır. Tüm bu çalışmalar

ışığında Kızıltepe cevherleşmesinin aktarım yokuşuna yerleşmiş epitermal altın Damarları olduğu öne sürülmüştür.

Anahtar Kelimeler: Altın, Düşük Sülfidasyon, Epitermal, Yapısal Kontrol, Aktarım Yokuşu, Kızıltepe, Batı Anadolu

To My Family

ACKNOWLEDGEMENTS

TABLE OF CONTENTS

LIST OF TABLES

LIST OF FIGURES

FIGURES

Figure 1.3. Simplified conceptual models of high temperature hydrothermal systems, showing the relationship between epithermal environments, magmatic intrusions, fluid circulation paths, and volcanic and basement host rocks. (A) The epithermal environment forms in a magmatic-hydrothermal system dominated by acid hydrothermal fluids, where there is a strong flux of magmatic liquid and vapor, containing H_2O, CO_2, HCl, H_2S, and SO_2, with variable input from local meteoric water. This type of environment is analogous to those existing in modern volcanoes (e.g., Hedenquist et al. 1993; Christenson & Wood 1993). (B) The epithermal environment forms in a geothermal system dominated by near-neutral pH chloride waters, where there is a strong flux of deeply circulated water (mostly of meteoric origin), containing CO_2, $NaCl$, and H_2S. The inferred location of the underlying

CHAPTER 1

INTRODUCTION

Mineral deposit is an unusually natural anomalous accumulation/concentration of aggregate of one or more minerals with economically important elements, typically base and precious metals, that can be economically extracted from the deposit. They occur as fairly continuous small, localized rock masses and contain sufficiently rich (high grade) ore mineral(s) plus admixtures of valueless (gangue) minerals. If the ore element/mineral grade and concentration, the size of the deposit reach to a level so that it is and accessible and producible to yield a profit; the mineral deposit is called an ore deposit and the assemblage of ore and gangue minerals, the ore (rephrased from Encyclopaedia Britannica and Wikiwand at https://www.britannica.com/science/mineral-deposit & https://www.wikiwand.com/en/Ore).

Ore deposits are complex (layered, disseminated, veins, folded and deformed) due to a wide range of genetic factors. Important factors include tectonic setting, host rock, structure, source and fluid composition, ore-forming process, and post-depositional modifications. Ore deposits are classified according to various criteria (such as fluid sources, type of metal, type of host rock, ore-forming processes, depth of ore formation, styles of vein texture, chemistry, tectonic environments and timing relative to an orogenic event or tectonic activity) and therefore different schemes are used to classify them: **(1)** type of metal or material they produce (e.g., copper deposits, gold deposits, uranium deposits, gold-silver deposits, etc.); **(2)** types of rocks that host the ore deposits or on the geological context (tectonic classification of ore deposits): volcanogenic massive sulfide deposits (Cu, Zn), sedimentary exhalative deposits (Zn, Cu, Pb, Au and Ag), porphyry Cu-Mo deposits, evaporites, sedimentary Cu deposits, fault-controlled mineralization, etc.; **(3)** ore-forming process: intrusion-related deposits, skarn deposits, magmatic deposits, granite-related deposits, volcanic-related

deposits, sedimentary deposits, metamorphically reworked deposits, orogenic gold deposits, hydrothermal deposits, vein-hosted deposits, deposits related to surficial processes/weathering; **(4)** depth of ore formation; one of the most popular classification scheme of hydrothermal mineral deposits (Lindgren 1933; Evans 1993): accordingly the mineral deposits are classified as Telethermal, Epithermal, Mesothermal, Hypthermal, and Xenothermal.

Among these different classification schemes and types of mineral deposits, the most relevant one to the main scope of the present thesis is 'epithermal deposits'; an overview of the literature will be given in the following section.

1.1. Epithermal Deposits Overview

The term epithermal (Buchanan 1981) deposits is used to describe mineralization (Au ± Ag ± Cu deposits) by warm to hot fluids at shallower crustal levels. The term is derived from Greek word 'epi' meaning shallow and the term 'thermal' relating to 'heat'; thus epithermal means 'shallow heat' and refers to warm to hot fluid (circulation) required for the deposit's formation. The term 'epithermal' was coined by Lindgren (1922) to define an environment that is shallow in depth typically hosts deposits of Au, Ag, and base metals.

Epithermal deposits commonly form at: **(i)** a temperature range of about 160° to 270°C, whereas maximum temperature is recorded at about 300°C; and **(ii)** a depth range below the paleowater table of about 50 to 700 m, respectively although there are few examples that formed at depths below 1000 m (Hedenquist *et al.* 1996; Sillitoe 1999; Hedenquist *et al.* 2000). They usually form through boiling and concomitant rapid cooling of ore-bearing hydrothermal fluids that originates from active magmatic and/or geothermal activity within the brittle upper crust (e.g., Buchanan 1981; Hedenquist *et al.* 1996; Sillitoe 1999; Hedenquist *et al.* 2000).

The source of hydrothermal fluids is commonly considered as either **(i)** a closed system of cooling and crystallizing water-rich magma body at shallow depths (a few km to over 10 km) (volcanic hydrothermal systems or intrusion-related hydrothermal

systems or magmatic hydrothermal systems) or **(ii)** high enthalpy geothermal systems associated with areas of volcanic and plutonic activity at convergent and divergent plate boundaries or **(iii)** non- magmatic fault (fracture)-controlled intermediate-high enthalpy geothermal systems in extensional tectonic regimes (rift-related geothermal systems). The latter two types of geothermal systems are also known as meteoric hydrothermal systems (e.g., Henley & Ellis 1983; White & Hedenquist 1990, 1995; Pirajno 1992; Hedenquist & Lowenstern 1994; Hedenquist *et al.* 2000; Sillitoe & Hedenquist 2003; Sillitoe 2015) (Figure 1.1-1.4).
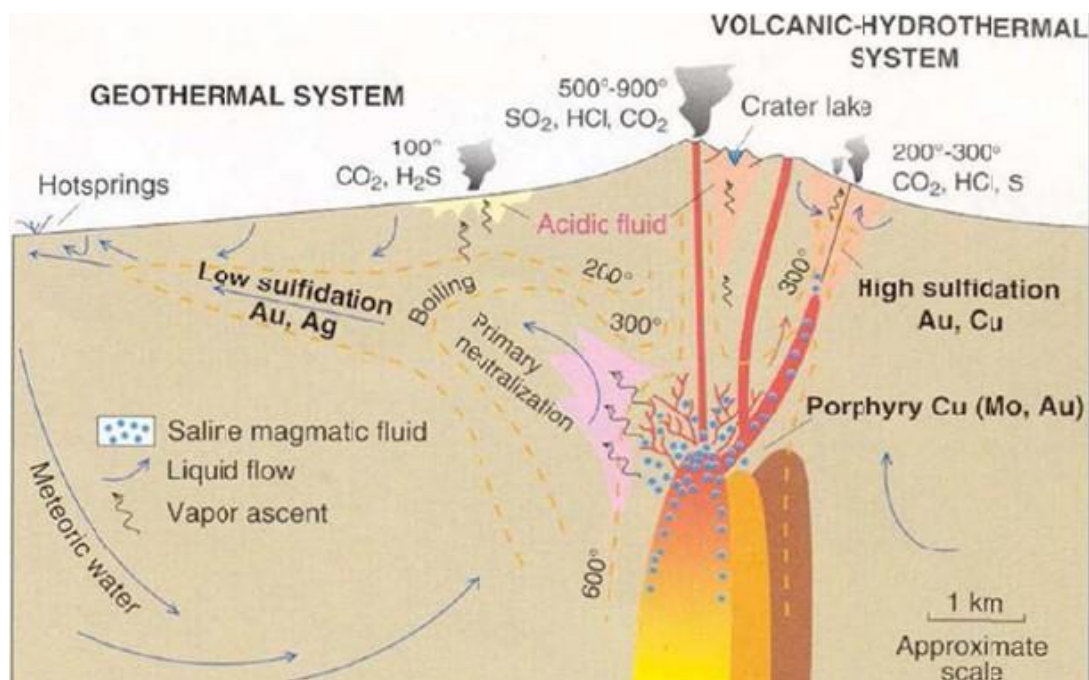
Figure 1.1. Schematic cross-section showing the relationship between volcanic-hydrothermal and geothermal systems. The diagram also illustrates the processes related two major types of epithermal environments. Note respective environments of high-sulfidation and low- sulfidation styles of epithermal ore deposits and their possible relation to shallow-seated intrusion(s). Note also that shallow-seated parent intrusion(s) are associated with a strato-volcano at the from Hedenquist & Lowenstern (1994), redrawn by Taksavasu (2017).

The precipitation from solution in epithermal environments occurs either **(1)** by gentle boiling if fluid enthalpy is sufficiently high to produce a small vapor fraction upon ascent or **(2)** by flash vaporization as a result of sudden transient pressure drop, through faulting or fracturing-related dilation, that converts most of the original liquid into a low density vapor phase (Moncada et al. 2012; Simmons et al. 2005; Weatherley

& Henley 2013; Sanchez-Alfaro et al. 2016). The metal (gold) mineralization usually occurs in open spaces, closely-spaced veins or vein swarms and stockworks; replacements, hydrothermal breccia bodies and disseminated forms are also common (Figure 1.5; Sillitoe 1993). The styles and geometries of epithermal ore bodies are mostly controlled by the host rock lithology, structure and hydrothermal processes (cf. Sillitoe 1993a; Hedenquist et al. 2000). Open space-vein are filled mainly with quartz, chalcedony and carbonates; veined- or brecciated-structures are also common. The veins display crustiform, cockade, colloform and comb textures, which are typical of open-space filling and boiling (Figure 1.6; Buchanan 1981; Morrison et al. 1990; White & Hedenquist 1995; Hedenquist et al. 2000; Moncada et al. 2012). In addition to metals (Ag, Au, As, Sb, Hg, Mo, Pb, Sn, W, Zn), epithermal deposits consists of silica (quartz, vuggy quartz, chalcedony and opal), carbonates (calcite and aragonite), sulfides (chalcopyrite, arsenopyrite, sphalerite, galena, cinnabar, stibnite, pyrite, and molybdenite), sulfates (alunite, barite, celestite and gypsum), adularia, fluorite and zeolit. Gold and silver form the most important metals exploited from epithermal deposits whereas galena and sphalerite also are common.

Various terms are proposed to describe and classify the epithermal deposits (Table 1.1). The most widely accepted and employed nomenclature suggests that there are broadly two main types of epithermal deposits, based on their contrasting sulfide assemblages and style of characteristic associated hydrothermal alteration (Figure 1.1, 1.7-1.9; Table 1.1-1.3): (i) low sulfidation (LS) or quartz-adularia-sericite type formed by reduced, neutral-pH fluids in association with low salinity, gas-rich geothermal systems and (ii) high sulfidation (HS) or acid-sulphate type (quartz-alunite type), produced by oxidized, strongly acidic fluids, typical of acidic springs near volcanoes (e.g., Heald et al. 1987; Hedenquist 1987; Sillitoe 1993a, b; White & Hedenquist 1990; Hedenquist & Lowenstern 1994; Hedenquist et al. 1994, 1998, 2000; Sillitoe & Lorson 1994; Arribas 1995; White & Hedenquist 1995; Corbett & Leach 1998; Hedenquist et al. 2000; Cooke & Simmons 2000; John 2001; Corbett 2002; Sillitoe & Hedenquist 2003; Simmons et al. 2005; Tosdal et al. 2009).
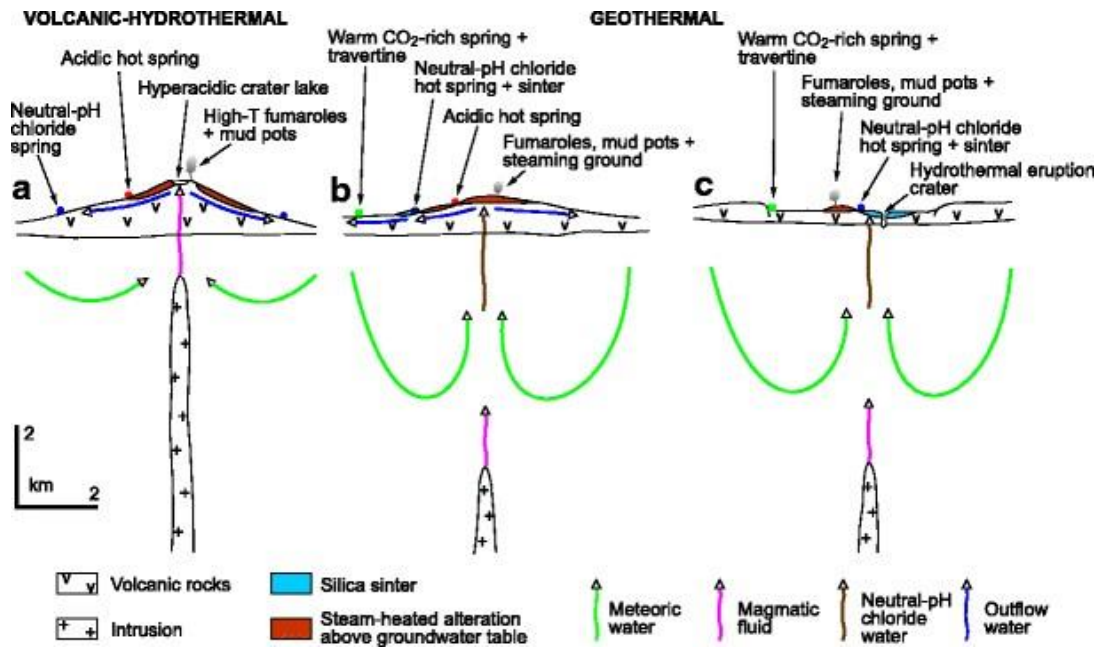
Figure 1.2. Schematic representation of active, high-temperature hydrothermal systems and their principal surface features (Sillitoe 2015). (a) Volcanic-hydrothermal system above shallow intrusion and dominated by magmatic fluids. (b) Geothermal system above deep intrusion in high-relief terrain, with ascendant neutral-pH, alkali chloride water unable to attain the surface except in outflow zones. (c) Geothermal system above deep intrusion in low-relief terrain, with deep neutral- pH, alkali chloride water reaching the surface.

The hydrothermal system in low-sulfidation environments is mostly dominated by meteoric water and the magma has limited role in their genesis whereas magma tic components are considerably involved in high sulfidation systems. A third group of epithermal deposits that contain sulfide mineral assemblages transitional between high- and low-sulfidation deposits (type 1 low-sulfidation deposits; John 1999, 2000; John et al. 1999) is termed as intermediate- sulfidation (Table 1.4 and 1.5; Hedenquist et al. 2000; Sillitoe & Hedenquist 2003; Sillitoe 2015). The two-end members and the subtype in-between differs from one another in their ore mineralogy, associated magmatism, and tectonic environment of formation.

A *Magmatic-Hydrothermal* **B** *Geothermal*

volcanic rocks

basement

intrusion

— water table   ↑ magmatic fluid

⟍⟋ meteoric water   epithermal deposit

Figure 1.3. Simplified conceptual models of high temperature hydrothermal systems, showing the relationship between epithermal environments, magmatic intrusions, fluid circulation paths, and volcanic and basement host rocks. (A) The epithermal environment forms in a magmatic-hydrothermal system dominated by acid hydrothermal fluids, where there is a strong flux of magmatic liquid and vapor, containing H_2O, CO_2, HCl, H_2S, and SO_2, with variable input from local meteoric water. This type of environment is analogous to those existing in modern volcanoes (e.g., Hedenquist *et al.* 1993; Christenson & Wood 1993). (B) The epithermal environment forms in a geothermal system dominated by near-neutral pH chloride waters, where there is a strong flux of deeply circulated water (mostly of meteoric origin), containing CO_2, NaCl, and H_2S. The inferred location of the underlying magma chambers in both (A) and (B) are portrayed to show the different path lengths that dee p fluids traverse before encountering the ore-forming environment. The relatively short path to the epithermal environment in (A) means there is minimal water-rock interaction during ascent, whereas the relatively long path to the epithermal environment in (B) means there is considerable water-rock interaction during ascent. The maximum pressure-temperature gradient under hydrostatic conditions is represented by boiling point f or depth (BPD) temperatures, which are also shown for reference. From Simmons *et al.* (2005).
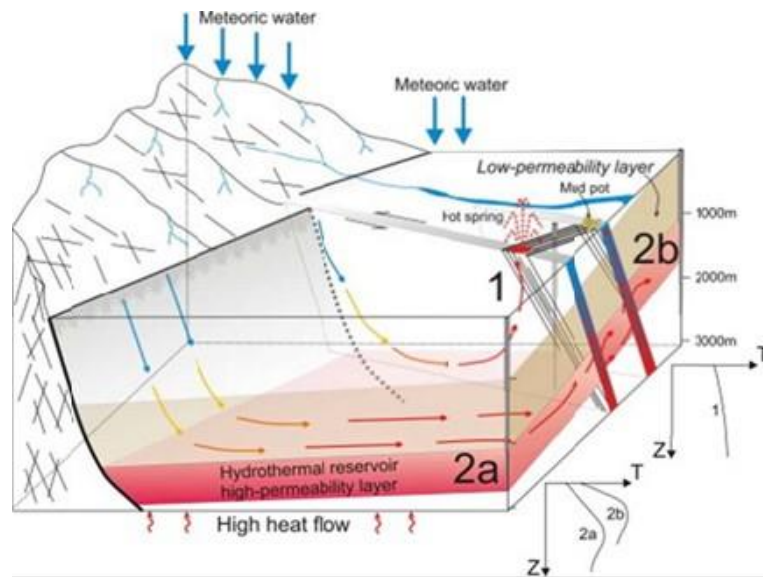
Figure 1.4. Illustration of a non-magmatic geothermal system in active extensional terrains, like those in western Turkey (Moeck, 2014). Type 1 - a convection cell from infiltration to discharge along one fault where temperature gradient is gradually increasing at wellsite 1. Type 2a and 2b - fault leakage controlled system where temperature gradient o f a well drilled into such an area rises up to the permeable layer and drops below the layer (well 2a and 2b).

High-sulfidation (HS) deposits are typical of Au-Cu-bearing epithermal deposits, with high contents of S, Se and Te, sometimes Hg. They are produced by moderate-low salinity (<2-5 wt%, up to 20-30 wt% NaCl equiv.; Hedenquist & Lowenstern 1994), presumably acidic gas (mainly SO_2, H_2S, HCl and CO_2)-rich, relatively higher pH (<2; Stroffregen 1987) strongly acidic oxidized waters (cf. White & Hedenquist 1990; Giggenbach 1992; Hedenquist *et al.* 1993, 2000; Hedenquist & Lowenstren 1994; Corbett & Leach 1998; Corbett 2002). They mostly occur in association with calc-alkaline andesitic-dacitic arcs (stratovolcanoes); those associated with more felsic rocks, such as quartz latite, are also reported. Rhyolitic rocks generally lack any appreciable HS mineralization (Sillitoe 1993a; Hedenquist *et al.* 2000; Sillitoe & Hedenquist 2003; Simmons *et al.* 2005).
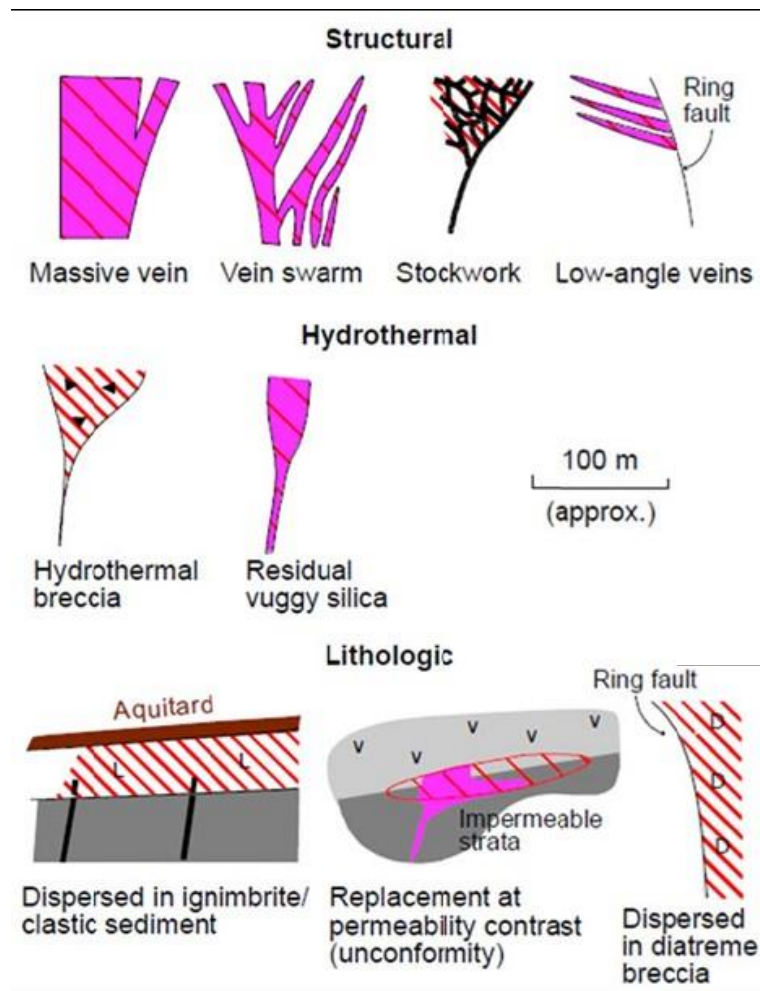
Figure 1.5. Selected styles and geometries of epithermal deposits. Typical examples include massif vein, vein swarm, stockwork, shallowly-dipping veins abutting a ring fault, hydrothermal dispersed in permeable rock beneath and breccia, residual vuggy silica, aquitard, replacement linked to permeability contrast and dispersed in diatreme breccia (from Sillitoe 1993).
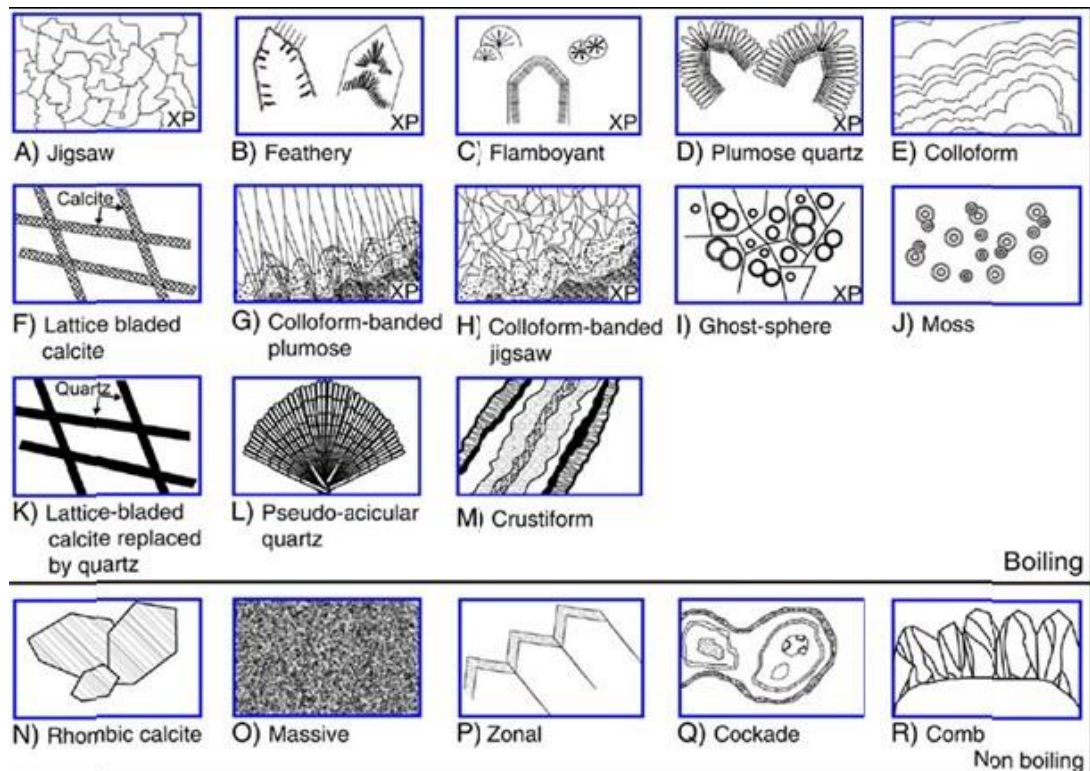
Figure 1.6. Summary of the various silica and calcite textures observed in the epithermal environment (from Moncada *et al.* 2012): (a) Jigsaw texture quartz; (b) feathery texture quartz; (c) flamboyant texture quartz; (d) plumose quartz; (e) colloform texture quartz; (f) lattice bladed calcite; (g) colloform-banded plumose texture quartz; (h) colloform-banded jigsaw texture quartz; **(i)** ghost-sphere texture quartz; (j) moss texture quartz; (k) lattice-bladed calcite replaced by quartz; (l) rhombic calcite; (m) massive quartz; (n) zonal quartz; (o) cockade quartz; (p) comb quartz. XP- view under crossed polars. Textures A–M are characteristic of rapid deposition, such as might occur during boiling, whereas textures N–R indicate that the fluids precipitating the mineral were not boiling.

The HS deposits genetically linked to, and display commonly a close relationship with, relatively deep-seated (ca. 5-6 km from surface; Hedenquist *et al.* 2000) porphyry copper- gold deposits (Hedenquist & Lowenstern 1994; Sillitoe 2002). That is why HS ore deposits display characteristic features that indicate involvement of magmatic components in their formation (cf. Rye 1993); extensive leaching of the host rocks results in O- and H-isotope compositions similar to that of magmatic vapour (Giggenbach 1992; Hedenquist & Lowenstern 1994).
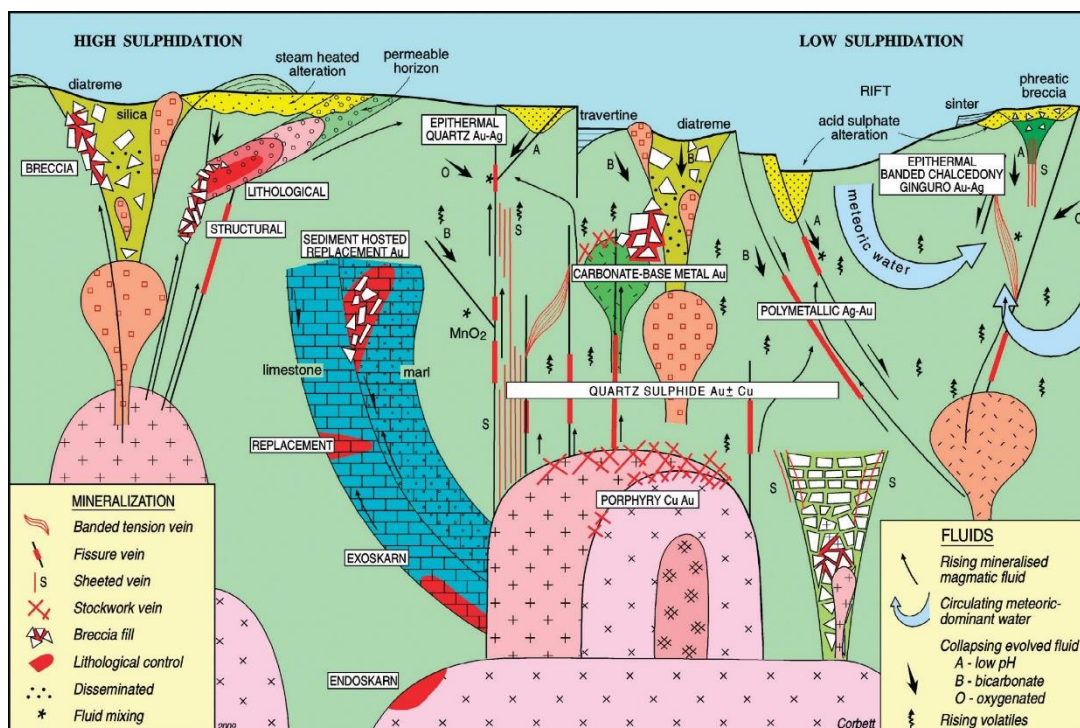
Figure 1.7. Conceptual model illustrating styles of magmatic arc porphyry Cu-Au and epithermal Au-Ag mineralization (from Corbett 2002, 2013).
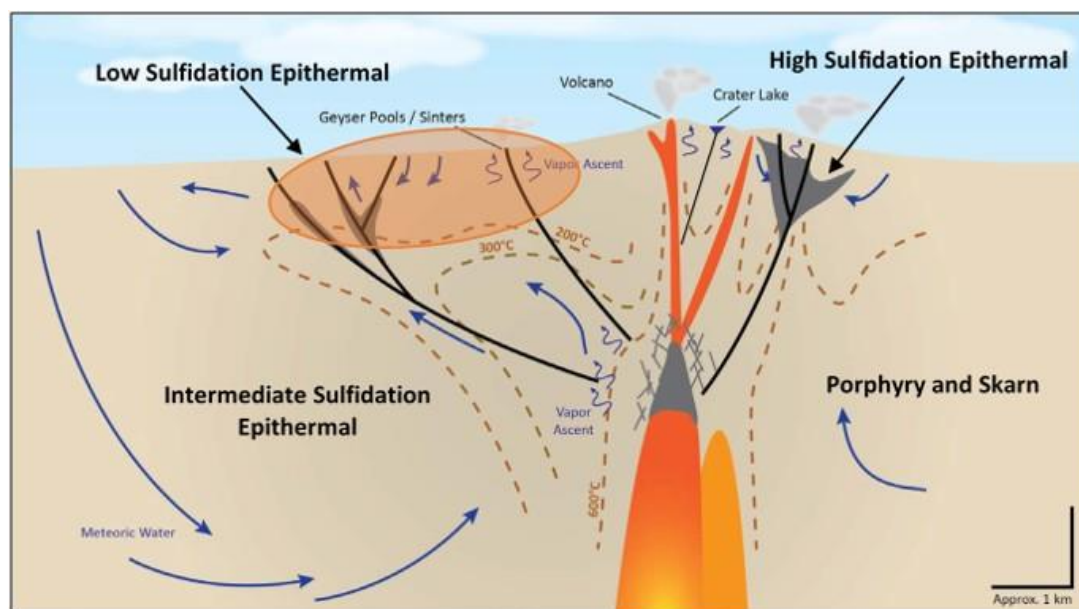
Figure 1.8. Conceptual model illustrating three styles of epithermal mineralization (http://www.ama.org.uk/wp-content/uploads/2013/11/LS-Epithermal2013_07_AMA.pdf).

10

Table 1.1. *Evolution of classification schemes applied to epithermal deposits (from Simmons et al. 2005).*

Reference	Type					
Sillitoe (1977)	Acid		Alkaline			
Buchanan (1981)	Epithermal					
Ashley (1982)	Enargite gold					
Giles and Nelson (1982)			Hot-spring type			
Bonham (1986, 1988)	High sulfur		Low sulfur		Alkalic deposits	
Hayba *et al.* (1985), Heald *et al.* (1987)	Acid sulfate		Adularia-sericite			
Hedenquist (1987), White & Hedenquist (1990, 1995)	High sulfidation		Low sulfidation			
Berger and Henley (1989)	Alunite-kaolinite		Adularia-sericite			
Albino and Margolis (1991)			Type 1 adularia-sericite		Type 2 adularia-sericite	
Sillitoe (1989, 1993a)	High sulfidation		Low sulfidation			
			High sulfide + base metal		Low sulfide + base metal	
White & Poizat (1995)	High sulfidation		Low sulfidation			
	Au-Ag-Cu deposits with vuggy quartz alteration	Au-Ag-Cu deposits with pyrophyllite-sericite alteration	Sn-Ag-base metal deposits	Ag-Au-base metal deposits	Au-Ag deposits With calc-alkaline volcanic rocks	With alkaline volcanic rocks
Hedenquist *et al.* (2000), Einaudi *et al.* (2003), Sillitoe & Hedenquist (2003)	High sulfidation		Intermediate sulfidation	Low sulfidation	Alkalic	
Cooke and Deyell (2003)	Descriptive nomenclature based on ore metals, deposit form, diagnostic hypogene gangue and alteration minerals, and dominant Cu-bearing mineral					

Table 1.2. *Summary of hydrothermal alteration assemblages forming in epithermal environments (from Simmons et al. 2005).*

Alteration	Mineralogy	Occurrence and origin
Propylitic	Quartz, K-feldspar (adularia), albite, illite, chlorite, calcite, epidote, pyrite	Develops at >240°C deep in the epithermal environment through alteration by near-neutral pH waters
Argillic	Illite, smectite, chlorite, inter-layered clays, pyrite, calcite (siderite), chalcedony	Develops at <180°C on the periphery and in the shallow epithermal environment through alteration by steam-heated CO2-rich waters
Advanced Argillic (steam-heated)	Opal, alunite (white, powdery, fine-grained, pseudocubic), kaolinite, pyrite, marcasite	Develops at <120°C near the water table and in the shallowest epithermal environment through alteration by steam-heated acid-sulfate waters; locally associated with silica sinter but only in geothermal systems
Advanced Argillic (magmatic hydrothermal)	Quartz, alunite (tabular), dickite, pyrophyllite, (diaspore, zunyite)	Develops at >200°C within the epithermal environment through alteration by magmatic-derived acidic waters
Advanced Argillic (supergene)	Alunite, kaolinite, halloysite, jarosite, Fe oxides	Develops at <40°C through weathering and oxidation of sulfide-bearing rocks

Table 1.3. *Reassignment of early epithermal classification Schemes (from Sillitoe & Hedenquist 2003).*

High Sulfidation	Intermediate	Low sulfidation	Reference
Goldfield type			Ransome (1907)
Alunitic-kaolinitic gold veins	Sericitic zinc-silver veins	Gold-silver-adularia veins	Emmons (1918)
		Fluoritic tellurium-adularia gold veins	
Gold-alunite deposits	Gold quartz veins in andesite		Lindgren (1933)
	Argentite-gold quartz	Gold quartz veins in	
	Argentite veins	Gold telluride veins	
	Base metal veins	Gold selenide veins	

Table 1.4. *Characteristics of low- and high-sulfidation epithermal deposits (from Foster 1993).*

Characteristics	Low Sulfidation (LS) (Adularia-sericite)	High Sulfidation (HS) (Alunite-sericite)
Structural setting	Structurally complex volcanic environments, commonly in calderas	Intrusive centers, 4 out of the 5 studied related to the margins of calderas
Size (length: width ratio)	Variable; some very large usually 3:1 or greater	Relatively small equidimensional
Host rocks	Silicic to intermediate and alkalic volcanics	Rhyodacite typical
Timing of ore and host	Similar ages of host and ore	Similar ages of host and ore (~ 0.5 m.y.)
Mineralogy	Argentite, tetrahedrite, tennantite, native silver and gold, and base-metal sulfides	Enargite, pyrite, native gold, electrum, and base-metal sulfides
	Chlorite common, selenides present, Mn gangue present, no bismuthinite	Chlorite rare, no selenides, Mn minerals rare, sometimes bismuthinite
Production data	Both gold- and silver-rich deposits	Both gold- and silver-rich deposits
	variable base-metal production	noteworthy Cu production
Alteration	Propylitic to argillic	Advanced argillic to argillic (± sericitic)
	Supergene alunite, occasional kaolinite,	Extensive hypogene alunite, major hypogene kaolinite, no adularia
Temperature	100-300 °C	200-300 °C
Salinity	0-13 wt % NaCl equiv.	1-24 wt % NaCl, probably related to the intense acid-sulfate alteration which preceded ore deposition.
Source of fluids	Dominantly meteoric	Dominantly meteoric, possibly significant magmatic component
Source of sulfide sulphur	Deep-seated magmatic or derived by leaching wall rocks deep in system	Deep-seated, probably magmatic
Source of lead	Precambrian or Phanerozoic rocks under volcanics	Volcanic rocks or magmatic fluids
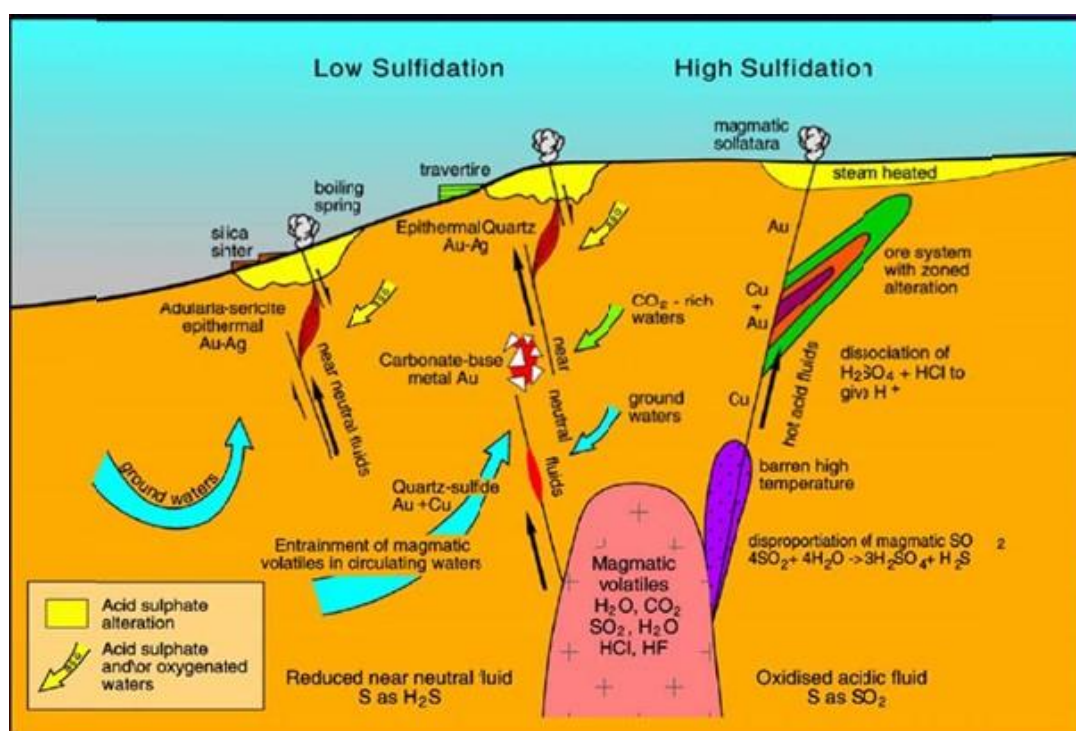
Figure 1.9. Derivation of low and high sulfidation fluids including arc- and rift-type low sulfidation (from Corbett 2002).

Table 1.5. *Summary characteristics of epithermal deposit types (from Sillitoe 2015).*

Epithermal type	High-sulfidation (HS)	Intermediate-sulfidation (IS)	Low-sulfidation (LS)
Main mineralization styles	Steep and shallowly inclined replacement bodies, hydrothermal	Veins, stockworks	Veins, stockworks, disseminated
Main proximal alteration types	Silicification, vuggy residual quartz, quartz-alunite	Silicification, quartz-sericite/illite	Silicification, quartz- adularia-illite
Main gangue minerals	Quartz, alunite, barite	Quartz, calcite, manganoan carbonates, rhodonite, adularia	Quartz, chalcedony, adularia
Sulfide abundance	High (10-80 vol.%)	Moderate (5-30 vol.%)	Low (1-5 vol.%)
Sulfidation-state indicators	Enargite/luzonite/famatinite	Tetrahedrite, chalcopyrite, low-Fe sphalerite	Pyrrhotite, arsenopyrite, high-Fe sphalerite
Typical metal signature	Au-Ag-Cu $\pm$ Bi $\pm$ Te	Ag-Au-Zn-Pb-Mn $\pm$ Cu	Au $\pm$ Ag $\pm$ Se $\pm$ Mo

The HS deposits contain more sulfide-rich assemblages, such as pyrite (Fe sulfide), enargite-luzonite (Cu-As sulfides) with rare tetrahedrite-tennantite (Cu-Fe-Zn-As sulfide) together with gold and copper. Some deposits may have only gold with negligible enargite but some are lack of gold. HS deposits are mostly rich in pyrite; they also contain Cu sulfides as digenite, chalcocite and covellite; advanced argillic alteration halo is composed of quartz- alunite ± pyrophyllite ± dickite ± kaolinite with local zones of silicic alteration.

Vuggy (porous) silica forms one of the other most prominent characteristic features of the HS epithermal deposits and results from extreme base leaching by strongly magmatic acidic hydrothermal fluids along their flow paths (sub-vertical fumarolic conduits) through, and chemical reactions with, the reactive host rock (cf. Zhu *et al.* 2011 and references therein). The vugs (pores) may later be filled with Au-bearing Cu- and Fe-sulfides (Arribas *et al.* 1995; Hedenquist & Lowenstern 1994). Vuggy quartz forms erosional resistant ledges as hilltops with surrounding typically zone advanced argillic alteration halo of quartz-alunite and quartz-pyrophyllite-dickite-kaolinite; vuggy silica is at the core of the alteration system.

Low-sulfidation (LS) deposits are typical of Au-Ag-bearing epithermal deposits, produced by low salinity (<1-2 wt% NaCl equiv.), presumably gas (mainly CO_2, minor H_2S and N_2)- rich, near neutral-pH, alkali chloride and reducing (sulfide dominant) dilute (with ground water) mostly meteoric waters (cf. White & Hedenquist 1990; Giggenbach 1992; Hedenquist & Lowenstren 1994; Corbett & Leach 1998; Corbett 2002). They mostly occur in association with bimodal (alkalic to calc-alkalic, and/or tholeiitic) volcanic suits (basaltic or basaltic andesitic to rhyolitic- rhyodacitic lavas and pyroclastic rocks) and fluvio-lacustrine sedimentation in normal fault-bounded rifts (grabens) in extensional tectonic settings (continental and island-arc rifts - near-, intra-, and back arc settings) (Sillitoe 1993; Sillitoe & Hedenquist 2003). They are associated with typical saline geothermal systems where magmatic signatures are more elusive since they form distant from their inferred magmatic source (cf. Hedenquist & Lowenstren 1994). In such systems, intrusions are located at a depth of

about 5-6 km from surface (Hedenquist *et al.* 2000), whereas deposits at about 1-2 km at temperatures of 200-300°C (Hedenquist & Henley 1985; Heald *et al.* 1987; Sillitoe 2015).

The LS epithermal deposits are classified, based on metal assemblage, as: **(i)** Au-rich deposits with trace base metals and form in association with low-salinity (1−2 wt% NaCl) gas-rich (up to 4 wt% CO_2 and H_2S) fluids; and **(ii)** Ag-rich deposits with economical Zn and Pb and form in association with relatively more saline (10−15 wt% NaCl) fluids (Hedenquist & Hanley 1985; Simmons *et al.* 1988; White & Hedenquist 1900). The most important characteristic of LS epithermal deposits is cited as absence of copper (cf. Hedenquist & Lowenstren 1994). Au-rich LS deposits from at shallow depths in low temperature environments, commonly show crustiform vein textures with dominant chalcedony and are typically hosted by rhyolitic- dacitic rocks in extensional settings (cf. Sillitoe 1993). Adularia is the most common gangue mineral and illite typically occurs in alteration halo. Pyrite, pyrrhotite and high Fe-sphalerite are minor sulfide minerals. Ag-rich LS deposits from at moderate depths in relatively high temperature environments, commonly show crystalline, massive and comb vein textures and are typically hosted by andesite-rhyodacitic rocks in arc settings (cf. Sillitoe 1993). Sericite is the most common gangue and alteration mineral whereas adularia is rare. This sulfide assemblage may represent an intermediate sulfidation state (Hedenquist *et al.* 2000).

Corbett (2002) classified, based on mineralogy, depth of environment of formation, and tectonic setting, the LS epithermal deposits as **(i)** arc-type low sulfidation and **(ii)** rift-type low sulfidation. The former forms in association with shallow-seated intrusions in the upper crust and is composed of varying ore (pyrite, sphalerite, galena, chalcopyrite, arsenopyrite), gangue (quartz, carbonate, clay) and wall rock (clay, chlorite) mineralogies. They are further classified as, with decreasing depth conditions, as quartz-sulfide gold ± copper, polymetallic gold-silver, carbonate-base metal gold and epithermal quartz gold-silver deposits. The second LS deposits comprise Au-rich adularia-sericite type and occurs in veins with gangue mineralogies

(chalcedony, adularia, quartz pseudomorphing platy carbonate) that are deposited from circulating dilute (meteoric dominated) geothermal waters in rift-related geothermal systems. They are fault (fracture)-controlled intermediate-high enthalpy geothermal systems in extensional tectonic regimes that develops in back-arc environments or in post-orogenic collapse of previously overthickened crust. Deposition commonly takes place in dilatant zones where faults intersect and interact structures. There appears a transition between arc-type LS and HS systems whereas it is very rare between rift- and arc-type LS stems.

Intermediate-sulfidation (IS) deposits are typically of vein and/or breccia-hosted Au- and Ag-bearing epithermal deposits. They are generally classified as mineralogically intermediate between the HS and LS types. The IS deposits occur mostly in association either with calc-alkaline andesitic-dacitic volcanic (stratovolcano) activity in arc settings or with andesitic-dacitic domes in pure extensional settings; those associated with more felsic rocks and displaying spatial association with porphyry systems are also reported (cf. Sillitoe 1989; Hedenquist *et al.* 2000; Sillitoe & Hedenquist 2003). Because both HS and IS deposits and LS and IS deposits can be closely associated and even transitional to one another, the IS deposits appear to have broadly similar fluid composition, ore and gangue minerals, style and type of alteration (John *et al.* 1999; Sillitoe 1999; Hedenquist *et al.* 2000; Sillitoe & Hedenquist 2003; Camprubí & Albinson 2007; Sillitoe 2015 and many references therein). In this regard, characteristics of IS deposits will not be covered here (see Table 1.10 for more recent information). On the other hand, HS and LS deposits normally appear to be incompatible (Sillitoe 2015). This is why, the epithermal deposits, in widely accepted and employed nomenclature, are represented by two end-members as low-sulfidation and high- sulfidation.

Epithermal deposits may form in variable tectonic settings involved in supercontinent cycle of rifting, ocean formation, convergence and collision. Therefore, they commonly occur in arc settings during both subduction of oceanic crust and continent-continent collision and post- collisional settings (Table 1.6; Figure 1.10 and 1.11).

16

Many form in near-, intra-, and back- arc extensional settings (both continental and island-arc rifts) during subduction where bimodal volcanic suites form. Post-arc environments following termination of subduction, and post-orogenic extensional environments characterized by normal fault-bounded grabens termination are also cited as suitable sites for epithermal mineralization.

Table 1.6. *Summary of relationships between sulfidation state of ore-forming environment, related igneous rock compositions, and tectonic setting proposed by Sillitoe & Hedenquist (2003) (from Simmons et al. 2005)*

Sulfidation State	Igneous Rock Composition	Tectonic
High	Calc-alkaline, andesite-dacite	Magmatic arc in a neutral to mildly extensional stress state; compressive stress state uncommon but serves to suppress volcanic
Intermediate	Calc-alkaline, andesite-rhyolite	Magmatic arc in a neutral to mildly extensional stress state; compressive stress state rare
Low	Calc-alkaline, alkaline, tholeiitic bimodal basalt-rhyolite	Magmatic arc undergoing extension leading to rifting; postcollisional rifting

The epithermal deposits commonly form in association with faults and/or shear zones. They play crucial role in controlling and localizing epithermal mineral deposit formation in shallow parts of the brittle upper crust. Faults enhance both porosity and permeability and can act as excellent pathways for passage, flow and circulation of mineralizing hydrothermal fluids from deep levels in the crust to relatively shallower levels where it boils, cools and precipitates the mineral content (e.g., Walsh & Watterson 1988; Evans 1990; Caine et. al. 1996; Knipe *et al.* 1998; Rowland & Sibson 2004; Corbett 2005, 2012, 2018; Shipton *et al.* 2006; Fredman *et al.* 2007; Wibberley *et al.* 2008; Braathen *et al.* 2009; Childs *et al.* 2009; Torabi & Berg 2011; Walsh *et al.* 2011; Bastesen *et al.* 2013; Blenkinsop *et al.* 2014; Hutchison *et al.* 2015; Micklethwaite *et al.* 2015; Vielreicher *et al.* 2016; Dimmen *et al.* 2017; Groves & Santosh 2017; Groves & Santosh 2017; Pérez-Flores *et al.* 2017; Funedda *et al.* 2018; Groves *et al.* 2018; Torremans *et al.* 2018; Tuduri *et al.* 2018; Chauvet 2019; Chen *et al.* 2019; Kyne *et al.* 2019). Faults may also act as potential structural and hydrogeological barriers (e.g., Caine *et al.* 1996; Rowland & Sibson 2004) and

therefore form suitable depositional sites for precipitation, accumulation and concentration of ore minerals from circulating hydrothermal fluids.
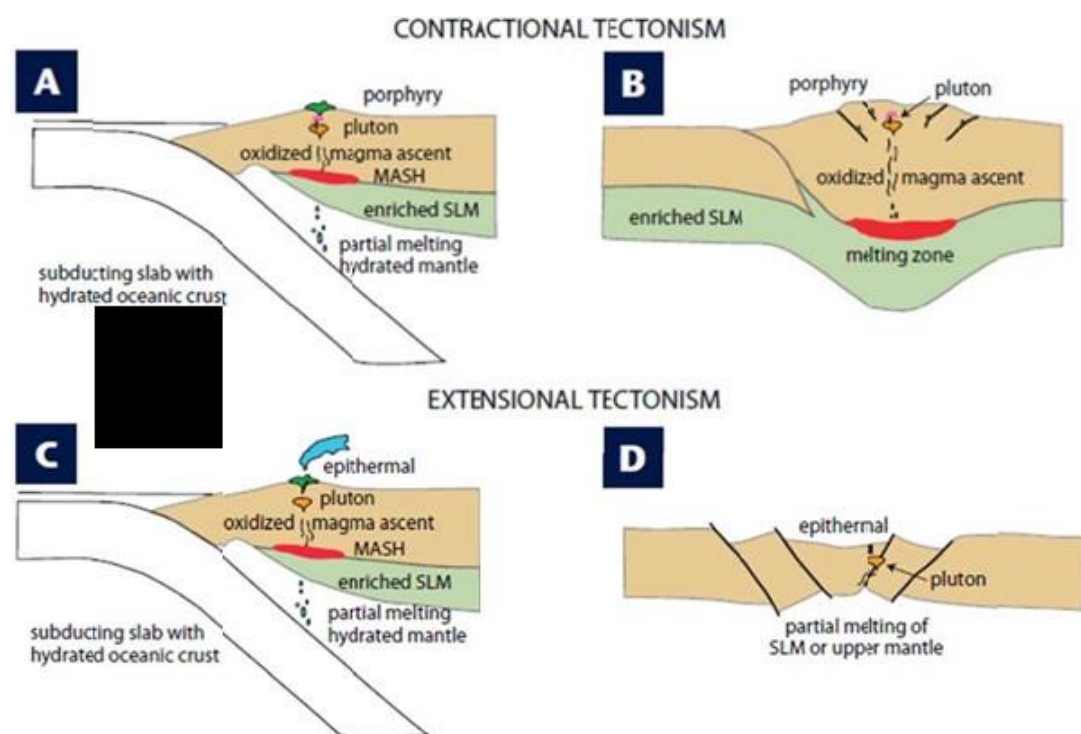
Figure 1.10. Tectonic setting of porphyry Cu and epithermal deposits. Porphyry Cu-Au deposits form at the end of magmatic episodes during contraction, dominantly in a convergent plate margin undergoing collision (A) or soon after collision (B). In contrast, epithermal de posits are associated with extension at the convergent plate margin (C) or (D) in a rift zone. MA SH– zone of crustal melting and assimilation, magma storage, and homogenization. SLM– sublithospheric mantle (from Tosdal *et al.* 2009).

Complexities along fault zones form most favorable structural settings for location and/or localization of hydrothermal fluid activity, and consequently ore formation: (i) stepover or relay ramp or pull-part between two overlapping moderately to steeply dipping en échelon fault segments with multiple minor faults providing hard linkage between two major faults (often named as dilational jogs); (ii) tip or terminations of major faults, whereby faults break up into multiple splays or horsetail; (iii) overlapping, oppositely dipping fault systems that generate multiple fault intersections in the subsurface and (iv) dilational fault intersection between normal and strike-slip or oblique-slip faults (Figure 1.12 & 1.13).

18
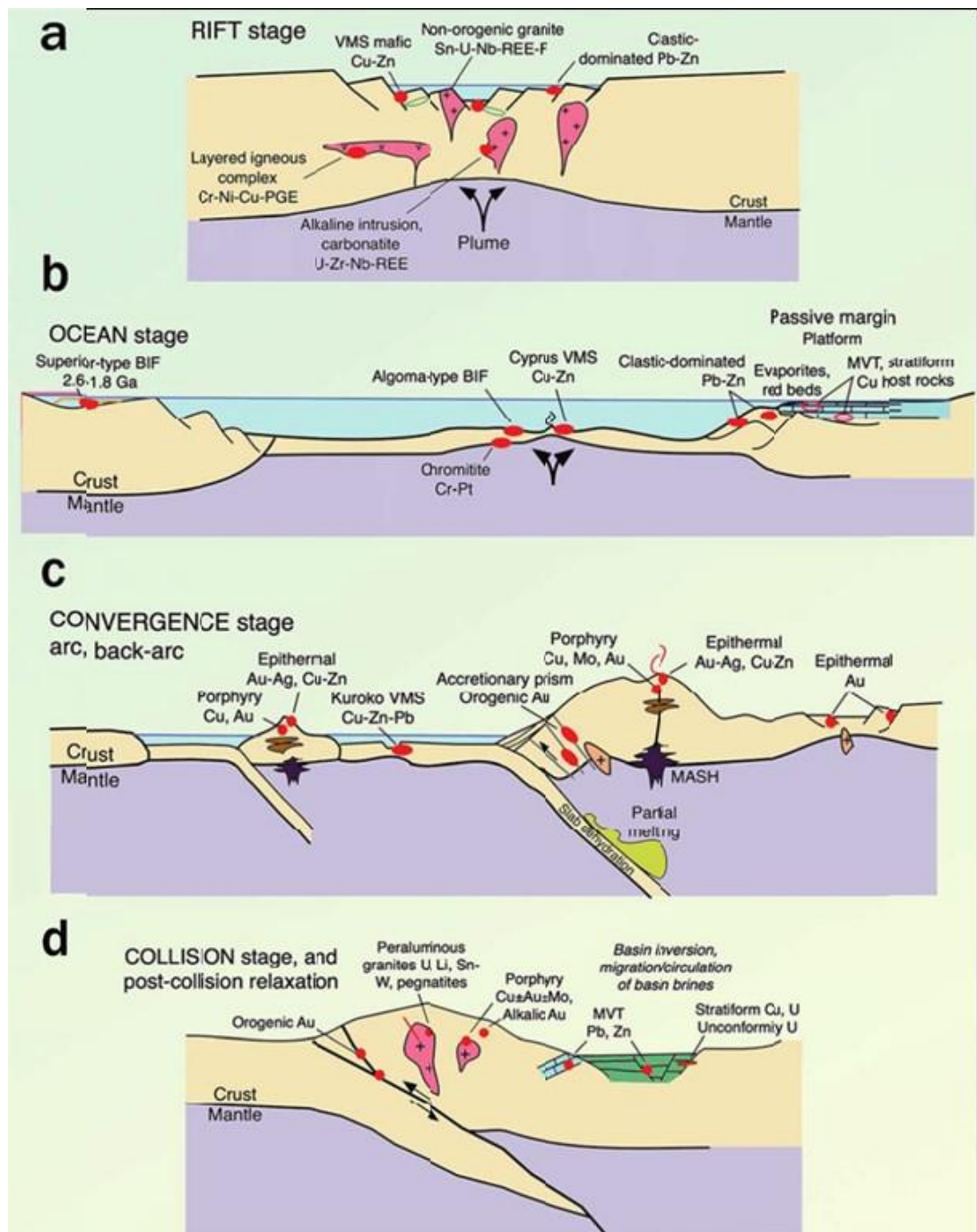
Figure 1.11. Schematic sections showing the association of selected ore deposit types of significance with their plate tectonic settings (a) thinning due to plume ascent and creation of primitive magmas; (b) Ocean stage: generation of new crust, and passive margins; (c) Convergence, subduction and creation of volcanic arcs and back-arcs, both in oceanic and continental settings; and (d) Collision as well as post-collision relaxation (extension), creation of anorogenic magmas and migration of basin-hosted brines in platform sequences. Formation environments of various ore types are shown with red dots (from Arndt *et al.* 2017).

The geological structures in and around the ore bodies have therefore to be studied and understood well in order to have a successful exploration and then mining programme. In particular, fault geometry and pattern, intersecting, interconnecting and interacting faults and their relationships have to be well studied and understood in order to have a successful exploration and mining programme. The better and correct understanding of the structural control(s) within a regional tectonic context provides valuable information about geometry, emplacement style, age, and origin of the ore deposit(s), including its geometry, emplacement style, age, and origin. Thus, structural control on mineral deposit formation should receive a special attention during any exploration programme and mining activity.

Although structural control is funDamental and plays a key role in the formation of economically important ore deposits, it is mostly ignored, not studied sufficiently, and/or given less priority during exploration programs.

In this thesis, a case study from the Kızıltepe low-sulfidation (LS) epithermal Au-Ag deposit (Sındırgı, Balıkesir) will be presented.

1.2. Location of the Study Area

The Kızıltepe low-sulfidation Au-Ag deposit is located in Sındırgı District, about 50 km south east of Balıkesir, and between the villages of Yusufçam to the west and Yolcupınar to the east (Figure 1.14). Çaygören Dam lies to the south of the mineralization. It geologically occurs within the NE–SW-trending early Miocene Bigadiç borate basin (Figure 1.15; cf. Erkül *et al.* 2005a, b) and so-called Bigadiç-Sındırgı volcanic field to the northwest of the İzmir-Ankara Suture Zone (Figure 1.16; cf. Dilek & Altunkaynak 2009). There are active faults in the Sındırgı district and the deposit area is bounded by the WNW–ESE-trending Quaternary Düvertepe normal fault zone in the north, ca. W–E-trending Holocene dextral Simav Fault in the south, and ca. N–S-trending Holocene dextral Gelenbe fault zone in the west (Figure 1.17). The basin and the volcanic field are bounded by NE-SW-trending İzmir- Balıkesir

transfer zone in the west and Uşak-Muğla transtensional transfer zone in the east (Figure 1.18; Karaoğlu & Helvacı 2012).
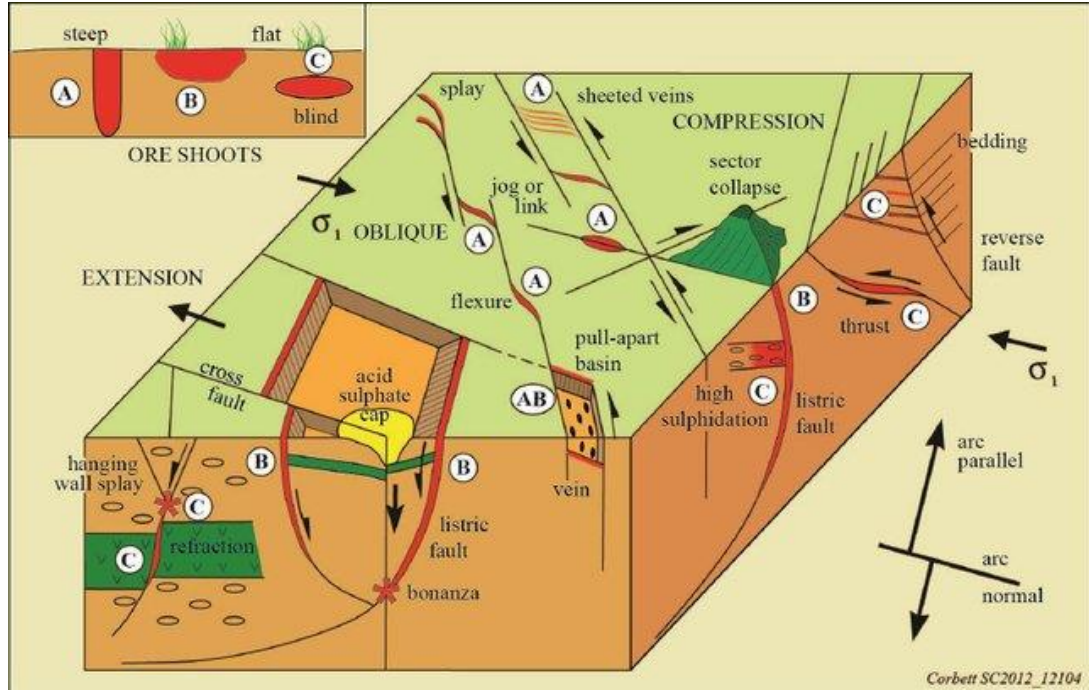
Figure 1.12. Summary of structural controls to epithermal Au deposits showing the relationship between style of deformation and orientation of ore shoots (from Corbett 2012).

The Kızıltepe LS Au-Ag deposit also occurs within so-called NE-SW-Sındırgı gold corridor (cf. Şener *et al.* 2006) to the east of Simav Fault (Figure 1.19 and 1.20). There are four known deposits in this corridor, namely Kızıltepe, Kepez, Karakavak and Kızılçukur. These deposits have been known and studied by mining companies in the frame of exploration programmes for many years but little is documented in the literature. Some of these exploration programmes are mostly concentrated on discovery of new mineral prospect and evaluation of the property for economic mining; many have terminated during reconnaissance stage. The Kızıltepe deposit is now in the mining stage and the exploration programme still continues for augmentation corridor.
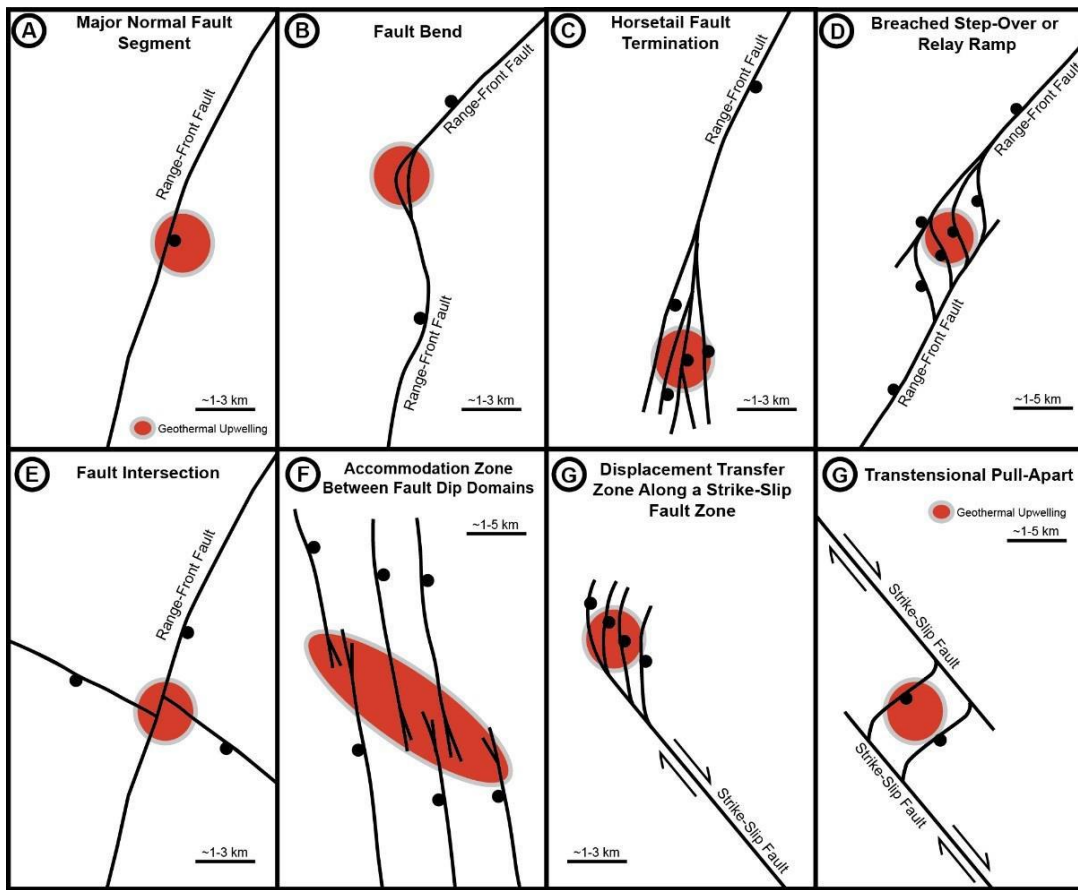
Figure 1.13. Examples of favorable structural settings for geothermal systems: (a) major normal fault segment; (b) bend along major normal fault segment; (c) fault tip or termination with main fault breaking into multiple strands or horse-tailing;,(d) fault step-over or relay ramp breached by minor connecting faults; (e) displacement transfer zone, whereby major strike fault terminates in array of normal faults (leading extensional imbricate fan); (f) fault intersection; (g) dilational fault intersection; (h) accommodation zone, consisting of belt of intermeshing oppositely dip ping normal faults; **(i)** accommodation zone, consisting of belt of oppositely dipping normal faults that generate multiple fault intersections; (j) transtensional pull-apart in major strike- slip fault zone (combined from Faulds *et al.* 2006, 2010; Faulds & Hinz 2015).

The Simav Fault (SF) is considered as the major structural element of the region. Different segments of the SF are interpreted to act as major conduit(s) for fluid circulation in the geothermal system; extensive hydrothermal alteration, presently observed as silicified zones and kaolinite-alunite deposits, is attributed to this system. The hot springs and travertine deposits in Hisaralan and Ilıcaköy suggest that the geothermal system is still active.
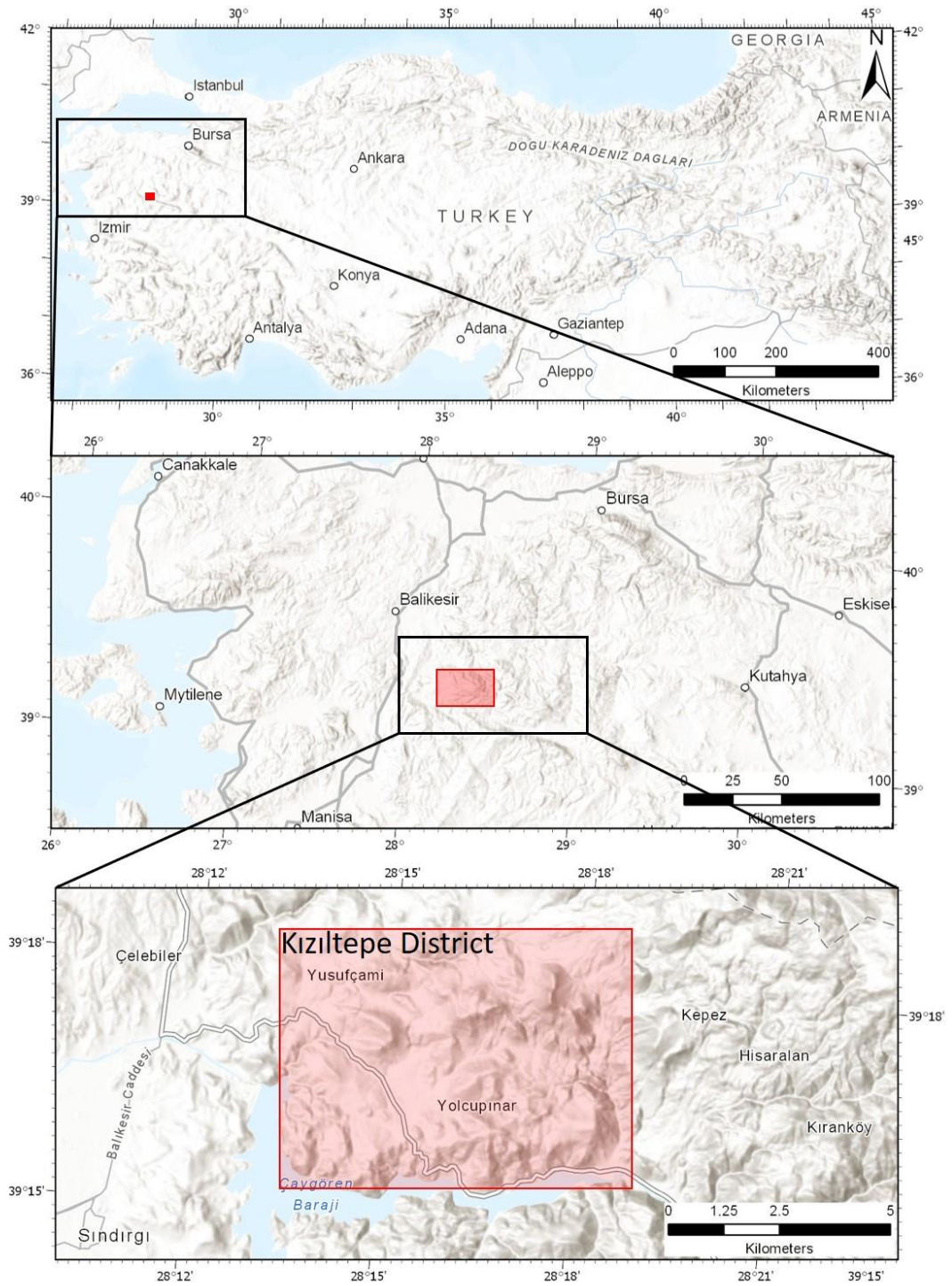
Figure 1.14. Google Earth images showing the location of Kızıltepe low-sulfidation Au-Ag deposit (Sındırgı, Balıkesir).

Figure 1.15. Geological map of the Bigadiç borate basin (from Erkül 2004; Erkül *et al.* 2005a).
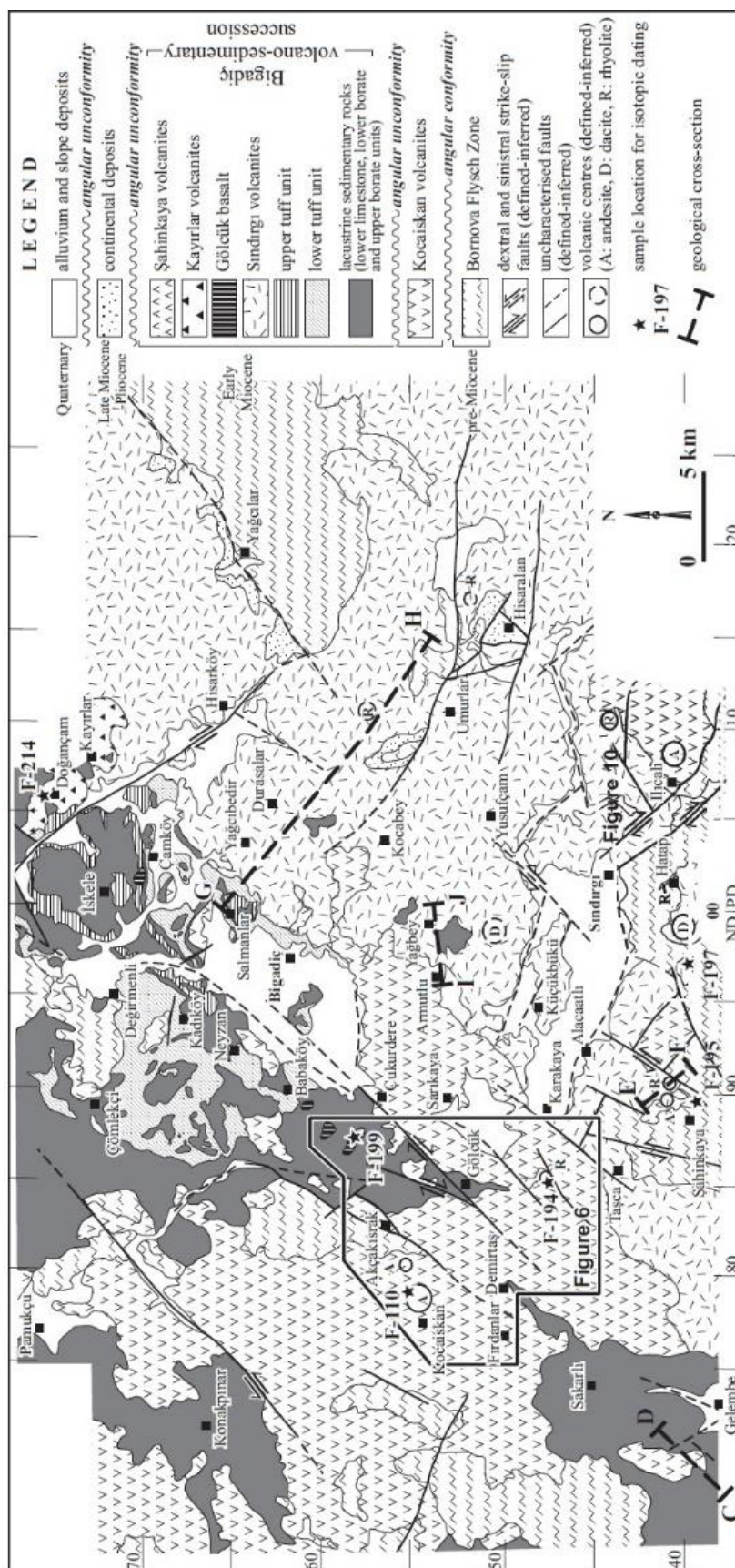
1.3. Purpose and Scope of Thesis

The Kızıltepe Au-Ag mineralization in Sındırgı District (Balıkesir) is interpreted as an example of low-sulfidation vein-type epithermal mineralization in western Turkey. Previous works are mainly concentrated on **(i)** mapping the distribution of gold-hosting quartz veins and, major structures in and around the deposits, **(ii)** studying morphology and texture of ore veins, **(iii)** studying petrography of quartz veins and alteration paragenesis, **(iv)** analyzing geochemistry of veins and host rocks, **(iv)** studying fluid inclusions to understand nature and genesis of main mineralizing fluid phases that may be responsible for ore precipitation, **(v)** dating the timing of mineralization, and finally **(vi)** testing economics of gold reserve and extractive metallurgy of gold in this epithermal system. The work on the structural control of vein formation and localization of epithermal mineral deposition is however very limited.

The present thesis is therefore mainly concerned with structural control on mineralization in this particular epithermal deposit. The aim and objective of the study are to: **(i)** recognize and map different types of structures present within mineralized zone and in the host rocks, **(ii)** gain further understanding of fault architecture and internal structures within the deposit, and finally **(iii)** observe and define how these structures and their development might have influenced, directly or indirectly, ore precipitation and localization of mineralization. This is done by studying faults within and nearby vicinity of the Kızıltepe deposit and within the open-pit mine along the Arzu South vein; and this is conducted by field observations and statistical analysis of the collected fault (slip) data.
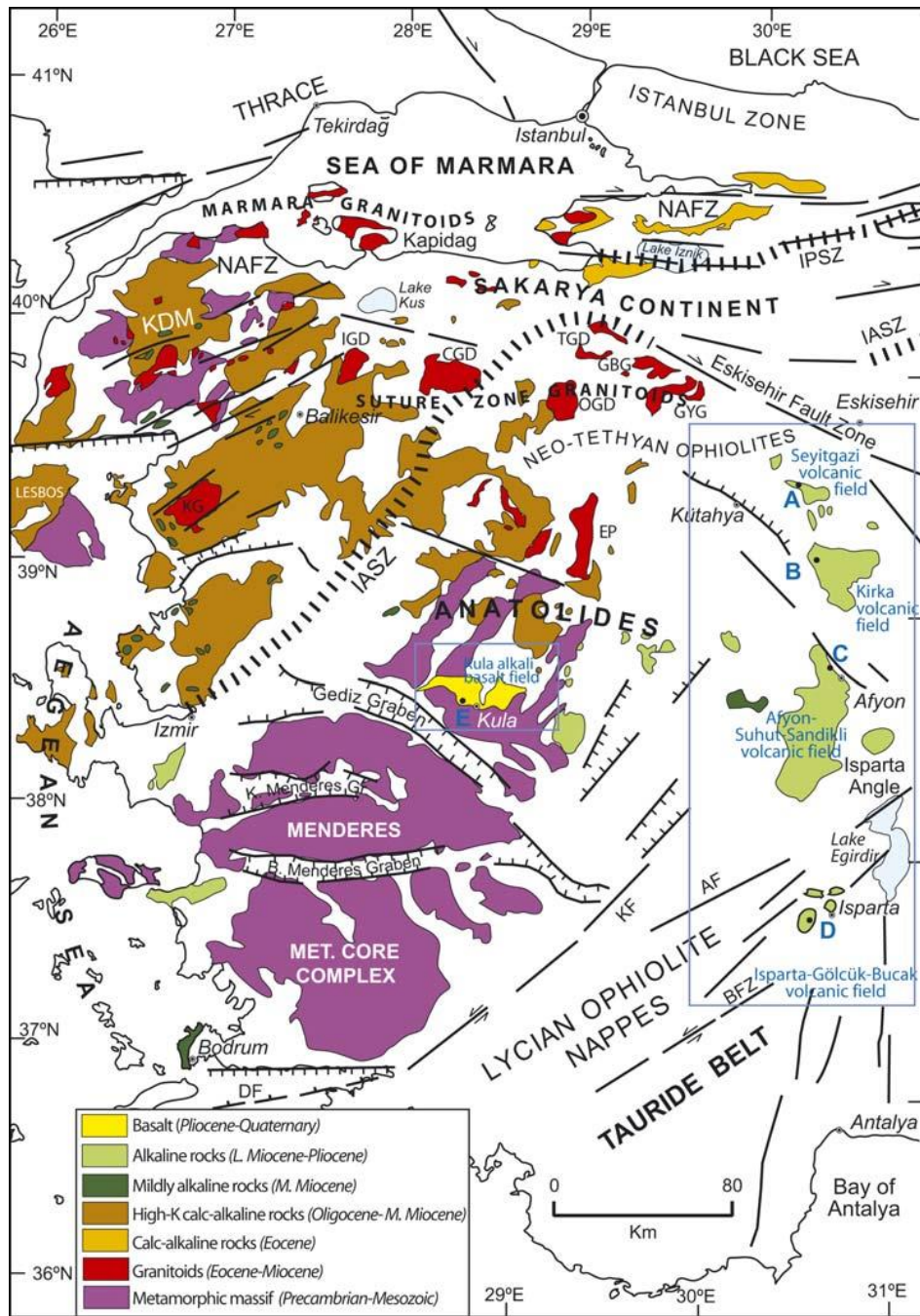
Figure 1.16. Simplified geological map of western Anatolia and the eastern Aegean region. showing the distribution of major Cenozoic igneous provinces and fault systems. AF-Acıgöl fault, BFZ-Burdur fault zone, DF-Datça fault, IASZ- İzmir-Ankara suture zone, KDM- Kazdağ Massif, KF- Kale fault, NAFZ- North Anatolian fault zone (from Dilek & Altunkaynak 2009).

26
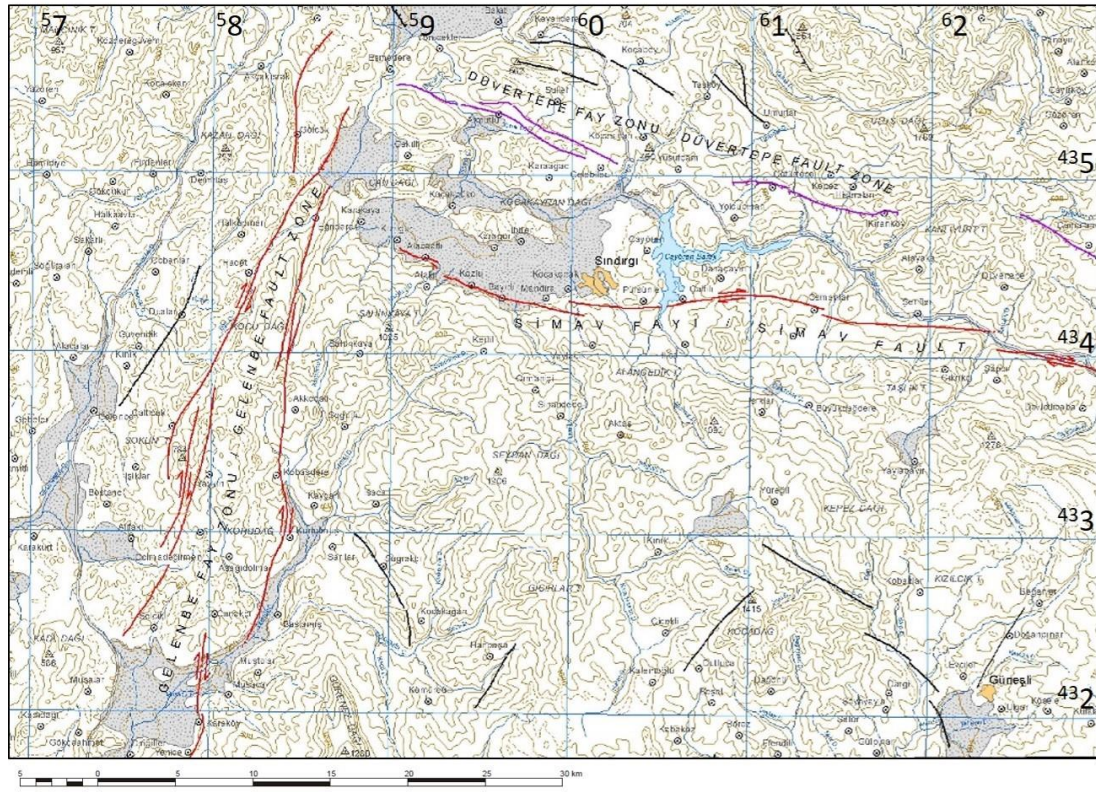
Figure 1.17. Active fault map of the Sındırgı district and its vicinity (from MTA 1:250,000 Scale Active Fault Map of Series Turkey; Balıkesir (NJ 35-3) Quadrangle, Serial No:4).

1.4. Methodology

To accomplish the objectives of the thesis, field mapping was executed on high-resolution images of the open pit taken by a drone camera. Detailed structural mapping of the open pit mine is carried out to: **(i)** understand type and geometry of the faults, fractures and veins; **(ii)** establish relationships between differently-trending fault segments (if exists), and veins; **(iii)** structural and kinematic analysis of faults and fractures to better characterize the geologic and structural setting; **(iv)** interpret slip data on faults and determine (regional) stress field; **(v)** determine the intersection and interaction of fault segments; **(vi)** discuss relative timing of faulting with respect to the veining and mineralization; and **(vii)** understand the structural styles of faults. Fault-slip data is analyzed with Win-Tensor software developed by Damien Delvaux and paleostress configurations are reconstructed.
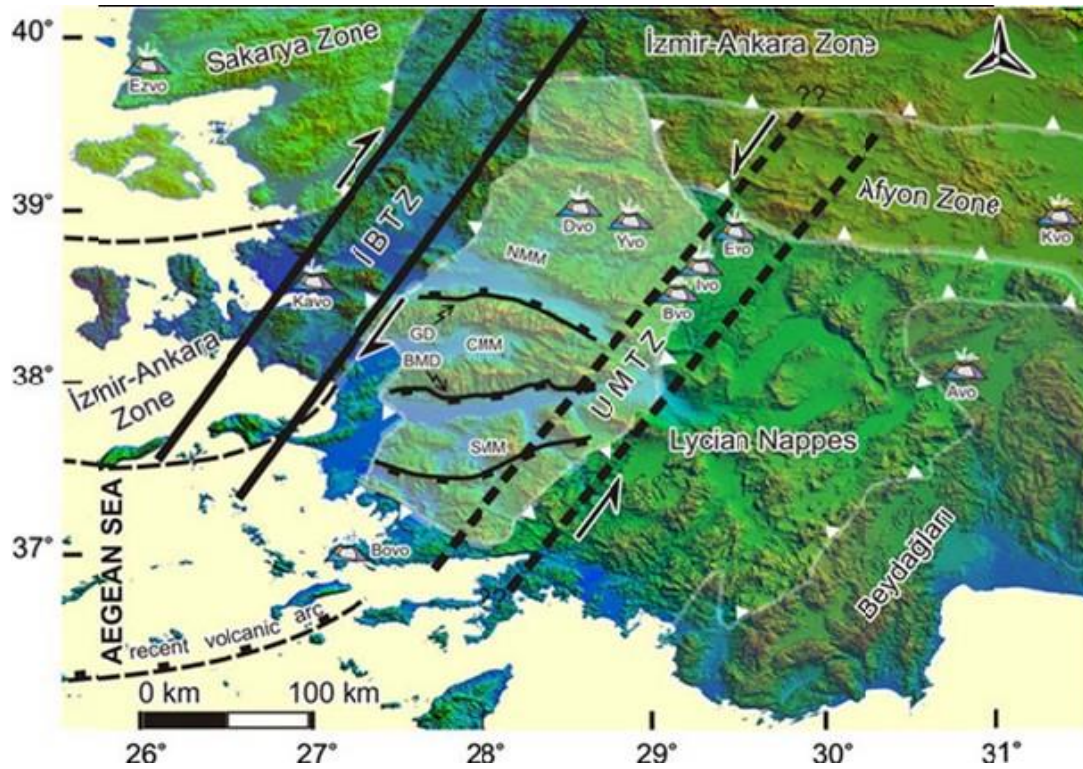
Figure 1.18. Simplified map showing the İzmir-Balıkesir Transfer Zone (İBTZ) and the Uşak-Muğla Transfer Zone (UMTZ). Kvo-Köroğlu, Avo-Afyon, Bovo-Bodrum, Kavo-Karşıyaka, Ezvo-Ezine, Dvo-Demirci, Yvo-Yağcıdağ, Evo-Elmadağ, Ivo-İtecektepe, and Bvo-Beydağı stratovolcanoes (from Karaoğlu & Helvacı 2012).

The structures, similar to those mapped locally at the scale of Kızıltepe LS Au-Ag mineralization, are also identified in other low- to high-sulfidation epithermal deposits in western Anatolia and in the Biga Peninsula. The results of the present thesis therefore would be useful contribute to the better understanding of structural control on local mineralization(s) in and around the Sındırgı district and the so called Kızıltepe Gold Corridor. The better understanding of deposit-forming structural setting would therefore be useful to comment on the regional meaning and significance of epithermal mineralization. A further detailed study is however required in order to understand and establish the relationships between ore-bearing quartz veins and regional structures and to study the interactions between the veins and faults.
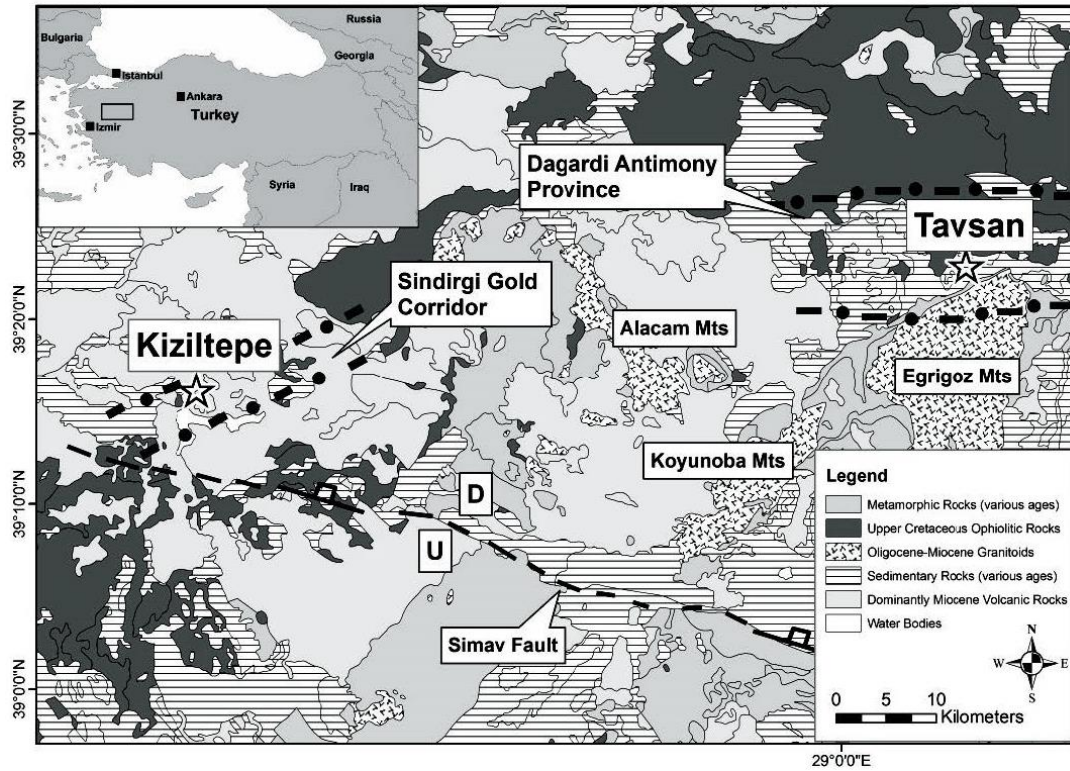
Figure 1.19. Simplified geological map of the Sındırgı to Dağardı region, showing location of Sındırgı gold corridor and its relation to the WNW–ESE-trending Simav Fault (from Şener *et al.* 2009).

1.5. Regional Geology

Turkey lies within the Alpine-Himalayan orogenic belt and is presently located at the boundary between the African and Eurasian plates in the eastern Mediterranean. Many microcontinental fragments (and intervening small oceanic basins), once being parts of two megacontinents - Gondwana in the south and Laurasia in the north, were amalgamated during continent-continent collision that has accompanied the complete demise of Neotethyan oceans when Arabian plate collided with the Anatolian plate in the Late Cretaceous-Tertiary (Bozkurt 2001).

29

The geological evolution of Turkey involves rifting, then opening of Tethyan oceans, widening of these oceanic basins, continent-continent collision, and final closure of these oceans. Literature agrees that there exist two oceans, Paleozoic-Early Mesozoic Paleotethys and Mesozoic-Early Tertiary Neotethys, and their evolution has partly overlapped in time. The closure of Paleotethys and its marginal Karakaya basin is attributed to Cimmerian orogeny. There is a common agreement that Neotethys was a multi-branched ocean but non consensus is reached about the number of these branches; broadly speaking northern Neotethys, southern Neotethys (Bitlis ocean or Peri-Arabic ocean), Intra-Pontide and Inner Tauride oceans form commonly accepted branches. Despite of intense research that lasts for several decades, there is still on-going discussions about the evolution of the Tethyan oceans and their branches. Discussions center around timing of basin opening and closure, number of Neotethyan branches, timing of continent-continent collision, number and polarity of subductions, number and location of sutures. Consequently, many alternative models have been proposed for the evolution Tethys oceans in Turkey. Consequently, several Neotethyan sutures have formed when these oceanic branches were closed during Alpine Orogeny. The suture zones are marked by complete or partial ophiolite complexes and ophiolitic mélanges (Bozkurt 2001).
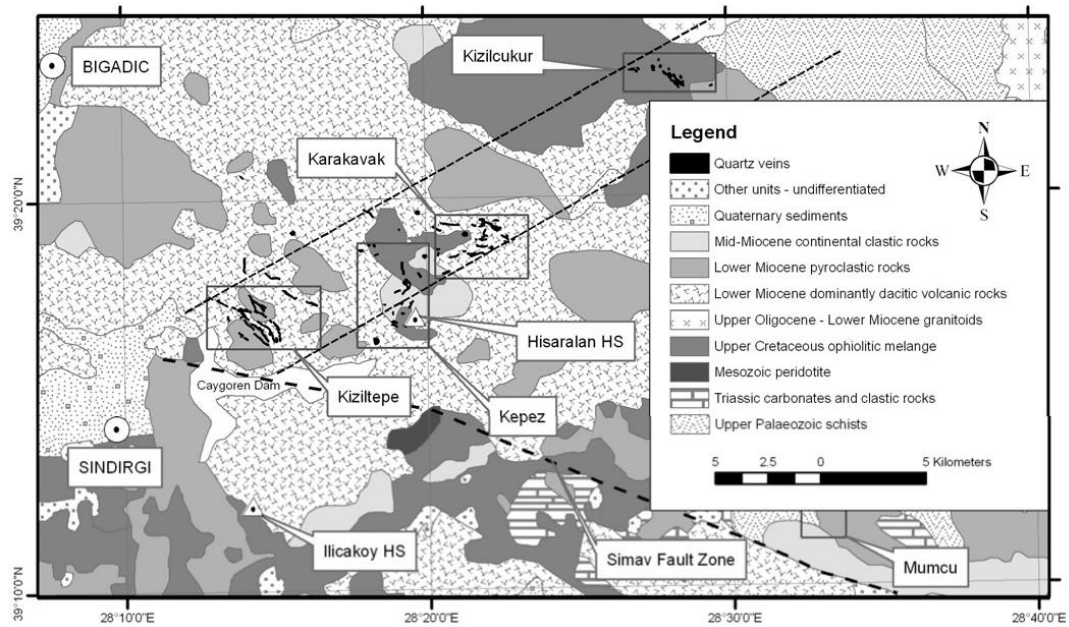
Figure 1.20. Simplified geological map of the NE–SW-Sındırgı gold corridor and its relation to the WNW–ESE-trending Simav Fault. Location of active hot springs Ilıcaköy and Hisaralan are also shown (from Şener *et al.* 2006).

Major Neotethyan suture zones include İzmir-Ankara-Erzincan, Intra-Pontide, Inner Tauride, Antalya and Bitlis-Zagros sutures that are marked by complete or partial ophiolite complexes and ophiolitic mélanges that represent progressive accretion of continental terrains with attached oceanic fragments (Figure 1.21). The major continents (Sakarya/Pontides, Anatolide-Tauride platform and Arabian platform) and many microcontinental fragments many were separated by intervening oceanic subbranches (now represented by suture zones) and, display different and complex history. İzmir-Ankara-Erzincan suture zone marks continent-continent collision between the Sakarya Continent in the north and Anatolides (Anatolide-Tauride platform) in the south and closure of northward subducting northern branch of the Neotethyan ocean. Final collision and suturing along the northern branched have continued till Late Paleocene-late Burdigalian. The Bitlis-Zagros Suture Zone in southeast Turkey marks final closure of the southern Neotethys; continent-continent collision across the Arabian plate in the south and the Eurasian (Anatolian) plate in the north have continued through the late Middle Miocene (Bozkurt 2001).

31

Presently Turkey is cited at the active convergent zone of Arabian, African and Eurasian plates in the Eastern Mediterranean. Anatolia moves (south)-west-ward, with respect to Eurasia and Arabia, along the North Anatolian and East Anatolian faults. Whereas Western Turkey have been experiencing post-orogenic extensional (collapse) tectonics since, at least, the latest Oligocene (Seyitoğlu & Scott 1991). Western Turkey has been experiencing active extensional deformation due to active subduction along the modern Aegean arc, back-arc extension and post-orogenic extensional collapse, and strike-slip related deformation.

Post-orogenic extensional collapse and thinning of previously over-thickened crust is expressed by core-complex formation in the footwall of now low-angle normal faults (detachment faults), associated lower-plate granitic magmatism (e.g., Bozkurt & Park, 1994; Hetzel *et al.* 1995a, 2013; Işık & Tekeli 2001; Hasözbek 2003; Işık *et al.* 2003; Seyitoğlu *et al.* 2004; Ring & Collins 2005; Thomson & Ring 2006; Dilek *et al.* 2007; Glodny & Hetzel 2007; Özgenç & İlbeyli 2008; Akay 2009; Catlos *et al.* 2010, 2012; Erkül 2010; Öner *et al.* 2010; Hasözbek *et al.* 2011, 2012; Altunkaynak *et al.* 2012; Tatar-Erkül 2012; Erkül *et al.* 2013b; Öner-Baran *et al.* 2017; Rossetti *et al.* 2017; Asti *et al.* 2019; Nilius *et al.* 2019) and upper plate fluvio-lacustrine sedimentation in upper plate supradetachment basins (e.g., Seyitoğlu & Scott, 1991, 1992a, b, 1994, 1996; Cohen *et al.* 1995; Emre 1996; Seyitoğlu 1997; Sarıca 2000; Sözbilir 2001, 2002; Purvis & Robertson 2005a, b; Çiftçi & Bozkurt 2008, 2010; Erkül 2010; Emre *et al.* 2011; Ersoy *et al.* 2010a, b, 2011; Karaoğlu *et al.* 2010; van Hinsbergen 2010; van Hinsbergen *et al.* 2010a, b, c; Sözbilir *et al.* 2011; Çiftçi 2013; Özkaymak *et al.* 2013; Sümer *et al.* 2013; Koçyiğit 2015; Kent *et al.* 2017; Tepe & Sözbilir 2017; Asti *et al.* 2018, 2019). This has resulted in exhumation of two crustal-scale core-complexes, the Menderes Massif and Kazdağ Massifs; the Menderes, in fact, comprises several small-scale (sub) core-complex, each of which have a different and complex history (e.g., Bozkurt & Park 1994; Koçyiğit *et al.* 1999; Seyitoğlu *et al.* 2000, 2002, 2009; Glodny & Hetzel 2007; Seyitoğlu & Işık 2009; Hetzel *et al.* 2013; Bozkurt 2001, 2004, 2007; Çiftçi & Bozkurt 2008, 2009a, b, 2010; Hetzel *et al.* 1995a,

b, 2013; Lips *et al.* 2001; Catlos & Çemen 2005; Dilek *et al.* 2007; Öner *et al.* 2010; Tatar-Erkül & Erkül 2012; Erkül *et al.* 2013b; Ören Baran *et al.* 2017; Rossetti *et al.* 2017; Asti *et al.* 2019; Nilius *et al.* 2019). Two different models have been described for the exhumation history of Menderes Massif; (1) during Late Oligocene to Early Miocene symmetrical core complex exhumation (Ring et al. 2003), and alternatively (2) an asymmetric model based on the movements of the Lycian nappes in opposite direction (Seyitoğlu et al. 2004).

Normal fault-bounded E−W grabens (Gökova, Büyük Menderes, Küçük Menderes, Gediz, Bakırçay, Edremit, Kütahya and Simav grabens), form the best expression of active N−S extensional tectonics in Western Turkey. In addition to these grabens, approximately NNE- SSW-trending basins and intervening horsts (e.g., the Gördes, Demirci, Selendi, and Uşak- Güre basins) to the north of the Gediz Graben forms other prominent structural elements of western Turkey. These basins have localized Miocene-Pliocene fluvio-lacustrine sedimentation and accompanying granitic magmatism and calc-alkaline to hybrid volcanism (lava flows and associated pyroclastic rocks). More recently, the role of NE-SW-trending İzmir-Balıkesir transform zone (İBTZ) that localized strike-slip faulting and volcanism (Özkaymak & Sözbilir 2008; Uzel & Sözbilir, 2008; Özkaymak *et al.* 2011, 2013; Sözbilir *et al.* 2011; Uzel *et al.* 2011, 2013, 2015, 2017; Ersoy *et al.* 2012a; Seghedi *et al.* 2015). That is integrated as southern branch of NAFZ (Seyitoğlu & Esat 2019).

Similarly, Uşak-Muğla transtensional transfer zone (UMTZ) is proposed to be during the late Miocene and controlled by NE-SW-trending strike-slip and oblique-slip normal faulting (Karaoğlu & Helvacı 2012). The Menderes Massif is therefore delimited by both the İBTZ in the west and UMTZ in the east (Figure 1.18).
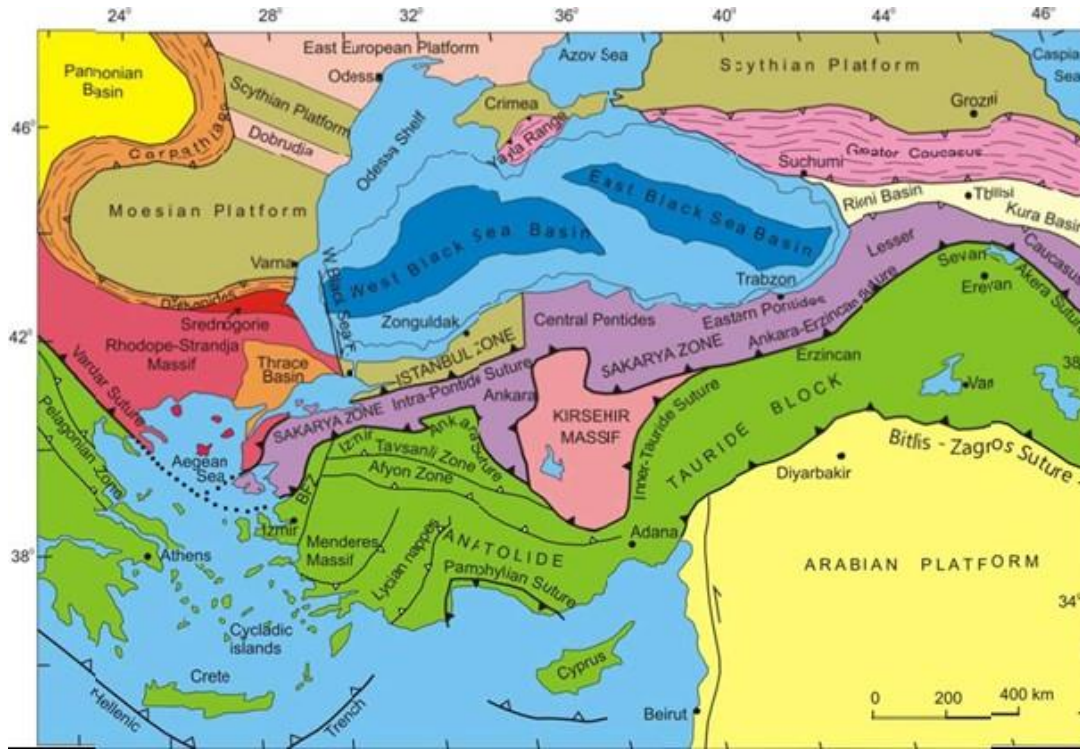
Figure 1.21. Simplified tectonic map showing the location of the main Tethyan sutures and neighboring major continental blocks in Turkey and its surrounding areas (from Okay & Tüysüz 1999). Heavy lines with filled triangles show sutures: the tip of triangles indicate polarity. Heavy lines with open triangles indicate thrust belts: triangles point vergence direction.

The area to the north of Gediz Graben is characterized by widespread magmatism occurred in western Turkey from the Late Oligocene to Early Miocene (e.g., Ercan *et al.* 1984; Yılmaz 1989; McKenzie & Yılmaz 1991; Seyitoğlu & Scott 1992; Seyitoğlu *et al.* 1997; Altunkaynak & Yılmaz 1998; Genç 1998; Karacık & Yılmaz 1998; Aldanmaz *et al.* 2000; Delaloye & Bingöl 2000; Akay & Erdoğan 2001, 2004; Işık & Tekeli 2001; Yılmaz & Karacık 2001; Yılmaz *et al.* 2001; Işık *et al.* 2003, 2004; Erkül 2004; Erkül *et al.* 2005a, b, 2006, 2013a, b, 2017; Ring & Collins 2005; Altunkaynak 2006; Thomson & Ring 2006; Ersoy & Helvacı 2007; Ersoy *et al.* 2008, 2010, 2011, 2012b, 2014a, b, 2017; Akay 2009; Agostoni *et al.* 2010; Altunkaynak *et al.* 2010, 2012; Dilek & Altunkaynak 2007, 2010; Hasözbek *et al.* 2010, 2011, 2012; Çoban *et al.* 2012; Catlos *et al.* 2012; Karaoğlu & Helvacı 2012a, b, 2014; Aldanmaz *et al.* 2015; Aysal 2015; Yücel-Öztürk 2016; Ünal & Altunkaynak 2018 and references therein).

34

The activity is expressed in two episodes: **(1)** The first magmatic phase is represented by Oligocene-Early Miocene intermediate to felsic high-K calc-alkaline granitic magmatism and associated calc-alkaline to alkaline volcanics (andesitic to rhyolitic lavas, domes, and pyroclastics). Kozak, Evciler, Ezine, Koyunoba, Alaçamdağ and Eğrigöz granitic-granodioritic plutons were emplaced at shallow levels (approximately 4 km below surface). NE–SW- and N–S-trending oblique faults formed pathways for magma and associated fluids to rise and reach the surface. The chemistry of rocks are consistent with mantle-derived magmas contaminated by abundant crustal components, similar to that of arc-derived associations. Subduction-related geochemical signatures are attributed to inheritance of a lithospheric mantle source enriched by subduction metasomatic processes during northward subduction of the Neotethyan oceanic lithosphere. Recent models argue for collision-driven slab breakoff for origin of this phase magmatism. **(2)** The second magmatic phase is represented by sporadically developed alkaline basalts (e.g., Kula basalts), which were emplaced from latest Miocene-Pliocene to recent time (Richardson-Bunbury 1996; Alıcı *et al.* 2002; Tokçaer *et al.* 2005; Bayhan *et al.* 2006; Holness and Richardson-Bunbury 2006; Westaway *et al.* 2006; Smith *et al.* 2008; Grützner *et al.* 2013; Heineke *et al.* 2016).

Shallow-seated granitic plutons have important role in the tectono-magmatic evolution of the region and in serving as source for heat and hydrothermal fluids that is cited as origin of porphyry and epithermal ore formation. This is why, several geochemical and geochronological studies were carried out about the granitoids and associated volcanic rocks. The plutons are mostly emplaced into the low-grade metamorphic rocks of the Menderes Massif and late Cretaceous ophiolites and mélanges of the İzmir-Ankara-Erzincan suture. Many of these plutons are interpreted as syn-extensional granitoids that intrude the footwall of the low-angle Simav detachment. The age data from these plutons can be summarized as: **(i)** Koyunoba granitoid: 23.2±0.1 to 20.4±0.1 Ma (Ring & Collins 2005; Hasözbek *et al.* 2010; Altunkaynak *et al.* 2012; Catlos *et al.* 2012; Çoban *et al.* 2012); **(ii)** Eğrigöz granitoid:

20.7±0.6 to 18.77±0.19 Ma (Bingöl *et al.* 1982; Erkül 2010; Hasözbek *et al.* 2010; Altunkaynak *et al.* 2012; Catlos *et al.* 2012); **(iii)** Alaçamdağ granitoid: 23.0±1.8 to - 19.5±0.1 Ma (Bingöl *et al.* 1982; Erkül 2010; Hasözbek *et al.* 2010; Altunkaynak *et al.* 2012; Catlos *et al.* 2012); and **(iv)** surrounding volcanic associations: 19.82±0.07 to 18.04±0.02 Ma (Çoban *et al.* 2012; Semiz *et al.* 2015).

The Sındırgı district is located within the Miocene Bigadiç borate basin (Figure 1.15); various characteristics of the basin have been studied several authors (Gündoğdu *et al.* 1989, 1996; Helvacı 1995; Erkül *et al.* 2005a, b, 2006; Gemici *et al.* 2008; Ersoy *et al.* 2011; Koç-Taşgın *et al.* 2018; Koç-Tasgın & Deniz-Akarca 2018). The basin lies within the NE-SW-trending İzmir-Balıkesir transfer zone. It is composed of borate-bearing deposits deposited in playas and perennial interconnected saline lakes and contains the largest borate deposits in western Turkey and in the world. Basin fill is represented by two distinct volcano-sedimentary associations above a so-called basement (Erkül *et al.* 2005a): **(1)** early Miocene andesitic intrusions, lavas, pyroclastic rocks and associated volcanogenic sedimentary rocks (Kocaiskan volcanites) and **(2)** overlying, with a basin-wide angular unconformity, early Miocene Bigadiç volcano-sedimentary. The basement is composed of low-grade muscovite-chlorite-quartz schists of the Menderes Massif, Upper Cretaceous-Palaeocene Bornova Flysch, composed of Mesozoic limestone olistoliths, ultramafic and chert blocks within aa flysch-type matrix, and Eocene sediments with nummulitic limestone and mudstone-sandstone intercalations. Bigadiç volcano-sedimentary sequences composed of several subunits; these are: **(i)** dacitic and rhyolitic intrusions, massive and autobrecciated lava flows, and pyroclastic deposits of the Sındırgı volcanites; **(ii)** NE-SW-trending olivine basalt dykes (and associated lavas) of the Gölcük basalt that intrudes the volcanic breccia of the Kocaiskan volcanites and the lacustrine sediments; **(iii)** NE-SW-trending (N40°E) andesitic-trachy-andesitic dykes and associated lava flows of the Kayırlar volcanites; **(iv)** NE-SW-trending andesite and basaltic andesite intrusions into the Bornova Flysch Zone and associated lava flows intercalated with autobreccia and pyroclastic rocks (Şahinkaya volcanites) and **(v)** lacustrine rocks

(lower limestone unit, lower tuff unit, lower borate unit, upper tuff unit and upper borate unit). The detailed stratigraphy of the Bigadiç borate basin and radiometric dates will be given in Chapter 2.

The most peculiar structures of the basin are represented by NE–SW-trending oblique-slip and strike-slip faults. These structures mostly form the boundary between Bornova Flysch Zone rocks and lower Miocene basin-fill sediments. The Damage zone around the faults may reach up to 100 m. The general orientation of the faults and olivine basalt, andesitic-trachy and andesitic dykes appear to be parallel and suggest a genetic link. They are interpreted as active structures during basin formation, sedimentation and volcanism. The NE–SW-trending faults and accompanying zone of weaknesses therefore have localized emplacement of volcanics.

Computed results from fault-slip data on normal faults are consistent with N–S extension while those from the NE–SW- and NW–SE-trending oblique faults suggest approximately NW–SE compression and NE–SW extension. The data is interpreted suggest that the oblique- and strike-slip faults may have developed during a NW–SE compression that might have accompanied a transpressional event. The Bigadiç borate basin evolved in to distinct stages: an early Miocene transpressional event and a younger transtensional event, separated by angular unconformity between the Kocaiskan volcanites and the Bigadiç volcano-sedimentary succession (Erkül *et al.* 2015).

1.6. Mineral Deposits of Western Turkey

Cited at the collision zone between two Laurasian continental masses to the north and Gondwana continents to the south, geology of Turkey records evidence for opening and closure of several oceanic basins throughout its geological history. Broadly Paleozoic-Early Mesozoic Paleotethys and Mesozoic-Early Tertiary Neotethys oceans formed, and then progressively closed when continent-continent collision occurred during late Paleozoic-Early Mesozoic and late Cretaceous-late Oligocene time interval, respectively. That is why Turkey have world class records of a typical super

continent cycle of rifting, opening of oceans, convergence by active subduction, continent-continent collision and closure of oceans. In this regard, Turkey has always been formed suitable sites for the formation of different types of ore mineralization in different tectonic settings. At present, Anatolia is located within the ongoing convergence zone of Arabian, African and Eurasian plates in the Eastern Mediterranean. The Anatolian plate moves westward with respect to Eurasia and Arabia along the North Anatolian and East Anatolian faults. Western Turkey has been experiencing post-orogenic extensional tectonics since, at least, latest Oligocene. Turkey therefore forms a part of one of the largest ore-producing belts, the Tethyan orogenic belt, that extends from Pacific Ocean (Indonesia) in the east, through Himalayas, Zagros, Anatolia, Balkans, to Alps in the west. That is why Turkey contains a wide spectrum of several ore deposits formed in different tectonic settings (see Pirajno *et al.* 2019, a recent book entitled 'Mineral Resources of Turkey', for more information).

The Western Turkey (especially Biga Peninsula) forms one of the richest locations and contains rich porphyry- and epithermal-type economic mineralizations. The country is cited as an emerging copper-gold province and is characterized by numerous economically important epithermal Au-Ag $\pm$ Hg-Sb and Pb-Zn-Cu-(Ag) deposits and prospects spatially associated with submarine to subaerial (late Cretaceous?) Eocene to Miocene calc-alkaline post- collisional magmatism (Figure 1.22; Table 1.7). Both low sulfidation (LS) (quartz $\pm$ calcite $\pm$ adularia $\pm$ illite) and high sulfidation (HS) (quartz + alunite $\pm$ pyrophyllite $\pm$ dickite $\pm$ kaolinite) types are common (cf. Yiğit 2009, 2012; Oyman 2019). In general, HS deposits from in association with porphyry-type deposits. The basic characteristics of epithermal deposits in the region are given in Table 1.7 and more detailed information is available in the literature. The readers are referred to recent publications (cf. Yiğit 2009, 2012; Oyman 2019) and many other references cited in them.
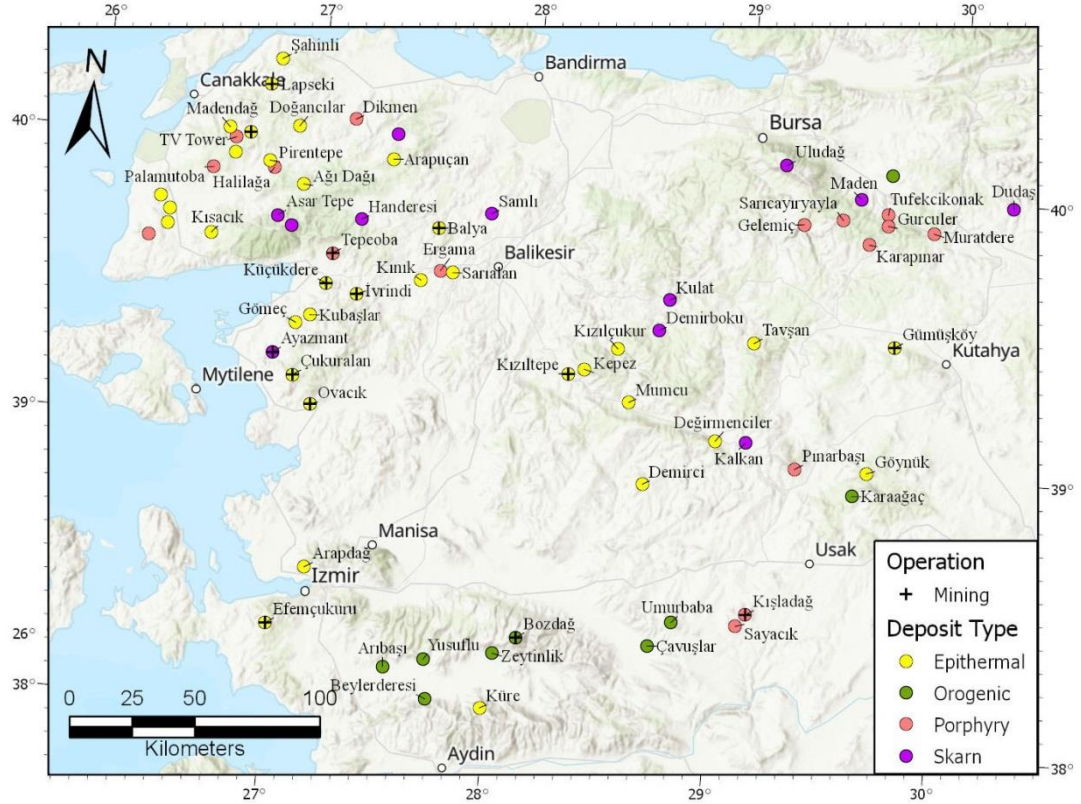
Figure 1.22. Distribution of mineral deposits, types and their operational status in Western Turkey.

1.7. Previous Studies

Ch. J. Hâlefi (1966) studied Hisarköy and Hisaralan hot springs in Bigadiç and Sındırgı districts (SE of Balıkesir). He mapped faults and shear zones, as well as the quartz veins in the region. NW-SE and ENE−WSW trending faults and their intersection/interaction are considered to localize carbonate precipitation in travertines. The hot springs use NE-SW- trending faults as pathways to rise to the surface. The rose diagram of open (tensional) shows that fractures trend in NE -SW (045°N) and NW-SW (312°N) directions. Two NW-SE- trending (150°N/60°-80°) major fault zones are mapped. The fault zone(s) is characterized by quartz veins and extensive silicification. Limonitization is common along fractures. The author was able to define 206 hot springs and associated travertine deposits are mapped.

The fossil openings used as pathways for geothermal waters outflow occur in two distinct directions: NE-SW (044°N) and NW-SE (314°N); so they are very similar to that of open fractures. The temperature of hot springs range between 48°C and 98°C (average is 82.2°C). Alteration is common around hot springs and along faults that control their formation. The author has concluded that the hot springs form along NW-SE trending two major faults.

Vedat Oygür (1997) has studied an Au-Hg epithermal mineralization in Mumcuköy (Sındırgı) area. Mineralization occurs along a fault that forms the boundary between metamorphic and Miocene andesitic volcanic rocks. HS Epithermal deposit is represented by hydrothermal quartz vein rich in Au (3.8 gr/t) and Ag (270 gr/t) within the schists. Argillic alteration (kaolinite, montmorillonite and cristobalite), intense silicification, brecciation, and opalisation are common in the prospect area. Breccia is composed of angular volcanic rock fragments embedded within black silica or limonite matrix where black silica and quartz veinlets are common. Intense jasperoidization is also common. White opaline coatings long fissure surfaces in tuffs is observed. Pyrite is widespread, drusy quartz is characteristic. Intense kaolinization, limonization and pyritization along faults/fractures and leaching in the host rock are cited as common processes. Mineralization occurs within mercury-bearing opalite zone in the metamorphic rocks and is represented by cinnabar associated with arsenopyrite, electrum (?) and rare gold particles. Derecikören granite is interpreted as buried porphyry stock that releases the hydrothermal fluids and provides heat to drive the epithermal system. Skarn deposits of base metals and porphyry of pyrite, limonite and stockwork quartz veins are attributed to granitic intrusion. Author has provided geochemical analyses from, and proposed a genetic model for the formation, the mineralization.

Table 1.7. *Characteristics of epithermal deposits in western Turkey. Compiled from Çolakoğlu (2000), Yılmaz (2003), Tezer (2006), Aydın (2007), Yiğit (2009, 2012), Oygür & Erler (2000), Yılmaz et al. (2010), Ece et al. (2013), Ünal-İmer et al. (2013), Smith et al. (2014), Kumral et al. (2016), Özen & Arık (2016), Oyman et al. (2019).*

Deposit Name	Commodity	Deposit Type	Principal Host Rocks	Age of Host Rocks	Ore Body and Structure
Ergama, Balıkesir	Au-Ag-Cu	IS & HS	Volcanic Rocks	Late Oligocene-Miocene	Sheeted or stockwork type veinlets
Küçükdere, Balıkesir	Au-Ag	LS	Andesite Porphyry	Miocene	Banded-quartz-carbonate veins; NE-SW-trending veins
Balya, Balıkesir	Pb-Zn-Cu-(Au-Ag)	Skarn/CR/ Epithermal	Dacite, andesite Limestone Conglomerate, sandstone and shale	Late Oligocene Permian Triassic	Veins, replacement, disseminations
Kızıltepe, Balıkesir	Au-Ag	LS	Acidic volcanics and ocerlying dacitic volcanoclastic sequence	Early Miocene	NW-SW- to NNW-SSE-trending vein swarms, few WNW-ENE-trendingveins, stockworks
Küçükdere, Balıkesir	Au-Ag-(Hg-As-Sb, Pb-Zn-Cu)	HS	Andesite	Miocene	NW-SE-trending two main veins, tension fractures, vein breccia; minor ~E-W- trending veins; NW-SE-trending and discting WNW-ESE-trending normal faults
Kubaşlar, Balıkesir	Au	LS	Metasedimentary rocks of Kınık Formation near the contact with the Kozak Pluton	Early Triassic	WNW-ESE-trending multi-stage vein breccia
Gömeç, Balıkesir	Au-Ag	LS	Andesite porphyry and overlying andesitic-dacitic volcanoclastics	Late Oligocene-Early Miocene	Veins, quartz breccia bodies, silicifiedfaults; E-W trending faults
Karadere, Balıkesir	Au-Ag	LS	Andesitic domes and overlying agglomerate-volcanic breccia	Late Oligocene-Early Miocene	NE-SW-trending veins; NE-SW-trending low angle normal fault
Ovacık, İzmir	Au-Ag	LS	Andesite porphyry, late stage dolerite dikes	Early Miocene	Banded-quartz veins, breccia; E-W-trending M vein and NW-SE-trending S vein
Efemçukuru, İzmir	Au	LS	Flysch, hoenfels Rhyolite intrusions premineralization	Late Cretaceous-Paleogene Neogene	Veins, stockworks, breccia; NW-SE-trending faults and veins
İnkaya, Kütahya	Cu-Pb-Zn-(Ag)	HS	Mica-quartz schists of the Menderes Massif	Paleozoic?	E-W-trending veins; NW-SE-trending fault
Karakoca, Kütahya	Pb-Zn-(Cu-Ag)	IS	Koyunoba platon	Early Miocene	NW-SE-trending intra-plutonic veins, breccias and stockwork; E-W-trending faults are intersected the N-S-trending faults
Su Döşeği, Kütahya	Pb-Zn-(Cu-Ag)	HS	Eğrigöz pluton	Early Miocene	NW-SE-trending intra-plutonic veins, breccias and stockwork
Yukarı Ortaburun (Katrandağ), Kütahya	Pb-Ag-(Au)	Epithermal	Dolomitic limestone along the contact with Eğrigöz pluton	Late Paleozoic-Early Triassic; mineralization is Early Miocene	Veins; silicified dolomitic limestone, N-S- and NE-SW-trending faults
Mumcu, Kütahya	Au-Ag-Hg	HS	Andesitic volcanic rocks Schists	Miocene Paleozoic?	Silicified, brecciated and opal bearing zones; N-S transfer faults
Değirmenciler, Kütahya	Sb	HS	Limestone lenses of mwtamorphic rocks	Paleozoic?	Vein, hydrothermal breccia
Körkuyu, Kütahya	Sb-Hg-(As-Au)	HS	Serpentinites of the melange Recrystallized limestones	Late Cretaceous Late Triassic-Late Cretaceous	Thrust of melange and related hydrothermally silicified zone; NNW-SSE-trending active fault zones

Table 1.7. *Continued.*

Deposit Name	Commodity	Deposit Type	Principal Host Rocks	Age of Host Rocks	Ore Body and Structure
Arapçukuru, Kütahya	FeS₂	HS	Gneisses Porphyry dike	Paleozoic? Miocene?	Massive pyrite lenses; N70°W-trending
Kestanelik and Şahinli, Çanakkale	Au-Ag	Epithermal	Andesitic volcanic rocks Schists	Eocene? Paleozoic	NE-SW- and E-W-trending veins with some N-S-trends
Ağdağı, Çanakkale	Au-Ag	HS	Felsic to intermediate volcanic rocks	Oligocene	Disseminations, breccias, NE-SW-trending mineralized and altered zone
Kirazlı, Çanakkale	Au-Ag	HS	Andesitic and dacitic lavas and pyroclastics	Oligocene	Stockworks, breccia, disseminated and replacement; NNE-SSW-trending mineralized zone, sub-horizontal ore zones
Kısacık, Çanakkale	Au-Ag	LS	Dacitic-rhyodacitic and andesitic volcanic rocks	Middle-Late Miocene	Multi-phase hydrothermal breccias; NE-SW-trending veins and stockworks; NE-SW-trending mineralized and altered zone
Arapuçan, Çanakkale	Pb-Zn-Cu(Au-Ag)	LS	Metasandstone and metadiabase Nearby dacitic rocks Granitic intrusions	Triassic Oligocene Miocene	5 major veins; E-W and NE-SW-trending veins
Madendağ, Çanakkale	Au-Ag	LS	Andesite and dacites Schists	Middle Eocene Paleozoic	E-W to WNW-ESE veins, breccia and stockworks; mainly NW-trending veins, NE-trending mineralized fissures and fractures
Koru and Tesbihdere, Çanakkale	Pb-Zn-(Au-Ag)	IS	Andesite lava and pyroclastics, rhyolitic lava-domes and tuffs	Eocene-Late Oligocene	Veins, stockworks, breccias, disseminated ore, NW-SE-trending falt and vein system
TV Tower, Çanakkale	Au-Ag-Cu	HS	Lapilli-bearing tuff sequence: lithic lapilli tuffs and epiclastic rocks, andesitic breccias and welded lithic lapilli tuff, fluvial-lacustrine sequence	Eocene-Oligocene	ESE-WNW veins, stockworks, breccia pipes; N-S- and NNE-SSW-trending near vertical brittle faults and their intersection with ESE-WNW-striking faults
Kartaldağ, Çanakkale	Au-Ag	HS	Dacite porphyry	Middle Eocene	Breccias, veinlets or as disseminations, NNE-SSW-striking normal faults
Pirentepe, Çanakkale	Au	HS	Dacitic to basaltic andesitic lavas and tuffaceous sediments, andesitic porphyry	Late Oligocene	Massive, brecciated NE-SW fractures, E-W controlling faults
Kuşçayırı, Çanakkale	Au-Cu-(Ag)	HS	Lava flows domes, andesitic to dacitic volcanoclastics and quartz feldspar dacitic porphyry	Middle Eocene	E-W-trending structures

42

Oygür & Erler (2000) documented summary information about the previously studied mineralizations occurring along the WNW-ESE-trending dextral Simav Fault (SF). They are vein-type base metal deposits, massive pyrite lenses, epithermal precious metal, mercury (Hg) and antimony (Sb) deposits, porphyry Cu-Mo deposits and hydrothermal kaolinite alunite deposits. Epithermal deposits are listed as Hg-Au Mumcu, Değirmenciler Sb, Şaphane alunite, Körkuyu Sb-Hg deposits. İnkaya Cu-Pb-Zn, Arapçukuru pyrite-copper and Pınarbaşı porphyry Cu-Mo deposits form examples for mesothermal mineralization in the region (Figure 1.24). Detail information about the Mumcular Hg-Au deposit is already given in the preceding paragraph (see Vedat Oygür 1997). The authors relate all these occurrences to magmatism in the region and deformation along the SF.

Vein-type İnkaya Pb-Zn-Cu mineralization forms along NW-SE-trending fault sub-parallel to the Simav Fault. The ore-bearing quartz vein occurs within schists and is composed of galena, chalcopyrite, sphalerite and pyrite. The vein is characterized by relatively high Ag content. The alteration in the host rocks is extensive as expressed by chlorite, illite, smectite and kaolinite. The presence of mafic dykes in the vicinity of the mineralization is used to suggest that there is a genetic and spatial link between mafic magmatism and mineralization. The metal-rich hydrothermal fluids are released from cooling magma, rise upwards and precipitate within a NW-SE-trending fault. During the final stage of the graben formation, epithermal mineralization has developed at suitable sites in associated with intense silicification and brecciation along the controlling N−S transfer fault(s). This has resulted in the formation of characteristic epithermal textures overprinting mesothermal base-metal (veins) mineralization.

Değirmenciler Sb deposit occurs as replacing limestone lenses and bands within the biotite gneisses or as open-space filling of stibnite-quartz veins. A strongly silicified and carbonatized dacitic porphyry dyke lies in the close vicinity of the mineralization. Limestones close to faults are replaced by jasper as aggregate of microgranular quartz and/or chalcedony. Advanced argillic alteration halo around the ore body is composed

of montmorillonite, smectite, dickite, opal, quartz and cristobalite. Stibnite-quartz veins contain pyrite and graphite with minor galena, chalcopyrite, molybdenite, bismuth, gold and silver. This mineral assemblage is used to suggest that they either have magmatic origin or partly form through leaching of, and chemical reactions with, the reactive host rock.
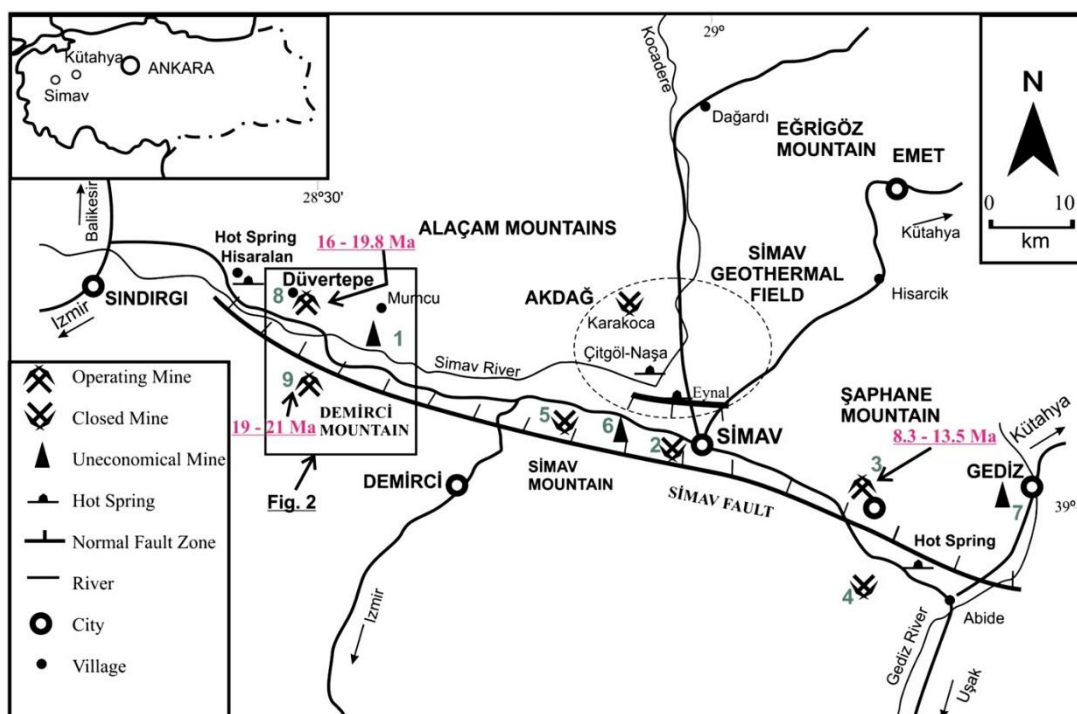
Figure 1.23. Index map showing locations of epithermal deposits along the Simav Fault (from Ece *et al.* 2013). 1- Mumcu Au-Hg, 2- Değirmenciler Sb, 3- Şaphane alunite-kaolinite, 4- Korkuyu Sb-Hg, 5- İnkaya Cu-Pb-Zn, 6- Arpaçukuru FeS2, 8- Pınarbaşı Cu–Mo, 8- Düvertepe kaolinite-alunite and 9- Arpatarla-Sapcı kaolinite–alunite. Dates on the map are Ar–Ar model age from alunite samples.

Şaphane alunite deposit forms within tuffs in relation to N−S and E−W trending faults. Extensive silicification is expressed, with increasing depth, by silica-alunite-kaolinite, kaolinite and alunite zones. A vuggy silica cap lies at the top of the alteration zone. Along faults cutting across the alteration halo, limonite and hydrothermal breccia is common; breccia is characterized by silica matrix and contains pyrite and chalcopyrite in places. The network of quartz veinlets is common. Some fractures re filled by opal with colloform texture where cryptocrystalline rutile and magnetite are reported. The

44

deposit is interpreted to form by replacement of volcanics through alteration by acidic sulphate-rich magmatic hydrothermal fluids from Cu-Mo porphyry.

Körkuyu Sb-Hg mineralization occurs with ophiolitic mélange that is characterized by large limestone blocks. Along faults/fractures, ophiolitic rocks are carbonatized and silicified to listwanites whereas marbles are partially replaced by jasperoides. The high molybdenum content of hydrothermal breccias suggests that listwanite forming silica-carbonate alteration forms in association with magmatic hydrothermal fluids released from a quartz-diorite porphyry. The alteration develops in zones that are composed, away from listwanites, of talc, carbonates (ankerite, siderite and dolomite) and silica. Fugacite is common in carbonate-rich zone. Mineralization occurs within the silica zone where quartz veins display comb and banded textures; these textures and opal occurrences are interpreted to suggest an epithermal system. The hydrothermal breccia is interpreted as sinter deposits of an epithermal system.

Arpaçukuru pyrite-copper mineralization develops along a N70°W-trending and NE-dipping fault that forms the boundary between gneisses and porphyry dike with disseminated pyrites. It is covered by a limonitic Fe-blanket and forms E−W-trending lens-shaped massive pyrite body. It is composed, with increasing depth, of arsenopyrite zone, galena-chalcopyrite-rich magnetic band, massive pyrite zone dissected by fractures filled with magnetite-chalcopyrite- sphalerite and magnetic zone cut by a network of barite veinlets that contains chalcopyrite and galena. The pyrite lines are cut by a N−S-trending fault, along epithermal quartz veins develop; veins are composed of amethyst and fine-crystalline quartz that shows banded and comb textures. The zoned structure of the ore body and its folding suggest that ore-bearing fluids have flowed into a basin, which is located in close vicinity of intrusion(s), to form a massive sulfide (pyrite) deposit.

Following brief description of known mineral deposits in the region, the authors have reached a number of conclusions; these include:

(1) Many vein-type base metal deposits and massive pyrite lenses, epithermal precious- metal, mercury and antimony mineralizations, porphyry-type Cu-Mo mineralization and hydrothermal replacement-type kaolinite and alunite deposits occur along the Simav Graben

(2) These mineral deposits have formed in association with two distinct tectono-magmatic phases during compressional paleo- and extensional neo-tectonic regimes.

(3) The plutonic rocks represent two distinct magmatic phases: calc-alkaline post-collisional granitoids representing the interaction of the crust and mantle sources and rift-related alkaline mafic dykes that probably has a mantle origin.

(4) The Pınarbaşı Cu-Mo mineralization has developed in the higher levels of a shallow- seated granitic (porphyry) intrusion during its final stages of emplacement under the compressional tectonic regime. Lack of contact metamorphism suggests that the intrusions were relatively dry and cooler. Porphyry dikes are responsible for the formation of massive pyrite lenses with base metals near the pluton in Pınarbaşı and probably Arpaçukuru deposits. This granitoid pluton (named the İnkaya pluton) that produced porphyry mineralization is also interpreted as the heat source that activates hydrothermal fluid cells for other mineralizations along the Simav Graben. The absence of fluorite suggests that there is no genetic link between mineralization and alkaline magmatism in the region.

(5) The anomaly of high molybdenum content in albite-, chlorite-, muscovite-, sericite- and quartz-muscovite schists are very important and is not compatible with a possible acidic magma source. The Mo anomaly is therefore explained by leaching of, and chemical reactions with, the reactive host rock where hydrothermal fluids rising from the granitoid(s) leached the host rocks along their pathways, thus get rich in precious metals.

(6) Following porphyry mineralization, possibly away from the İnkaya pluton, mesothermal vein-type Cu-Pb-Zn mineralization occurred in genetic and spatial relation to mafic dykes within so-called Karakoca pluton. The vein-type base metal mineralizations were deposited within NW-SE-trending tensional cracks that formed in association with WNW-ESE-trending dextral Simav Fault (SF) during the compressive regime. These veins have closely relationships with, both in time and space, late stage mafic dykes of granitoid intrusions.

(7) The native sulphur ore deposits within the tuffs form along a NW-SE-trending fault that is nearly parallel to the Simav Fault and is presumably associated with a porphyry system.

(8) The epithermal Hg-Au mineralization in Mumcu occurs along the N−S-trending transfer fault. They possibly represent mineralization during latest stage(s) of graben evolution and probably represent the highest levels of a buried porphyry system. Similarly, N−S faults were used as pathways for hydrothermal fluid flow and circulation, and precipitation in vein-type epithermal quartz-base metal mineralizations of İnkaya and Arapçukuru prospects. Travertine deposition, brecciation, silicification, open-space filling, comb, crustiform and colloform textures, and crustification are common epithermal features in these areas. The typical low- temperature comb texture and fine-crystalline amethyst suggest mineralization in meso- to epi-thermal environments.

(9) Değirmenciler Sb mineralization has presumably formed during epithermal stage in the outer zones of a magmatic-hydrothermal system rich in base metals and precious metals. The mineralization is related with a (sub-)volcanic activity in association with calc-alkaline granitic magmatism during closure of the Neotethyan Ocean.

(10) Also, during this period, mercury and antimony mineralizations developed within vugs and quartz veins that display comb, crustiform and banded textures of fine-

crystalline quartz and also opaline coatings. The mineralizing quartz veins occur within the Körkuyu listwanites.

(11) The Mumcu and Körkuyu deposits are interpreted as distal epithermal mineralizations of a porphyry system and occurred near the plaeosurface.

(12) The porphyry dykes intruding the carbonate lenses within metamorphics formed replacement-type antimony mineralization away from the Değirmenciler pluton.

(13) Replacement-type Şaphane alunite deposits represent epithermal mineralization at the palaeosurface in the uppermost levels of a porphyry system.

(14) Epithermal mineralizations are associated with the porphyry dykes in the late stage of the granitoids.

(15) The present-day sinter precipitation at Ilıcalar (Gediz) and numerous hot-springs give rise to intense active geothermal activity along the Simav Graben are the recent equivalents of this epithermal activity.

Kerim Şener *et al.* **(2006)** studied low-sulfidation style epithermal gold deposits in Sındırgı (Balıkesir) district. They occur in veins, vein breccias and stockworks. The veins form series of ridges in the region. The host rocks are dacitic volcanics and overlying dacitic volcanoclastic sequence of the so-called Sındırgı volcanic complex. The LS epithermal deposits are characterized by well-developed argillic alteration; alunite, kaolinite and silicification are common alteration products that contain gold in small amounts (up to 0.14 ppm). Lithologically-controlled mineralized and silicified zones are also reported. Veins are characterized by colloform-crustiform banding and lattice-and-moss textures. The textures and trace-element chemistry are used to suggest that erosion of veins have reached to chalcedonic super zone. There are four Au-Ag deposits, namely Kızıltepe, Kepez, Karakavak and Kızılçukur, that occurs in a broadly NE-SW-trending corridor. The Kızıltepe LS epithermal deposit is described as ca. 19.5-km-long NW-SE- and NNW-SSE-trending sub- parallel non-bifurcating LS veins and related stockworks hosted in dacitic lavas and pyroclastics.

Banu and Arzu veins dip 75-80° SW and 70-85°NE, respectively. Kepez prospect is represented by 2.5-km-long N-trending and bifurcating LS veins. One of the veins occurs along the contact between dacitic and ophiolitic rocks. The gold-bearing veins dominantly trend in NW-SE and WNW-ESE direction and are interpreted to mimic the Simav Fault. The N-trending veins are attributed to near vertical transfer faults formed in association with latest Miocene extension. Early Miocene is, based on stratigraphy of the host rhyodacitic-dacitic ignimbrites (ca. 20 Ma), suggested as the lower limit of mineralization. The veins are interpreted as conjugate R-shears that results in formation of NNW-SSE- and NW-SE-trending veins in a dextral strike-slip fault system. Because these LS deposits occur in close proximity to the Simav Fault (SF) (like Hg-Au and Sb occurrences and alunite- kaolinite deposits in the region), authors suggest that the Simav Fault (SF) plays an important role in the development of mineralization and alteration. They also propose that further detailed study is needed in order to better understanding of fault kinematics along the SF and its role in the metallogeny of the region.

Aygün & Çolakoğu (2008) studied the effect of grain size on the analysis value of stream sediments in the Kızıltepe LS gold mineralization. Twenty-eight (28) samples are systematically taken and four size fractions are extracted for further investigation. The samples were sieved to classify three fractions as >2 mm, 2 mm-500 micrometers, 500-177 micrometers and <177 micrometers. The fourth fraction is prepared by the Bathe technique. Average gold values (n= 28) for each size fraction are 2.7 ppb ± 3.33, 3.7 ppb ± 8.05, 14.6 ppb ± 20.28, and 5 ppb ± 11.11 (the Bathe technique), respectively. The results show that: **(i)** highest average gold content (ranging between 0.7 pp and 86.9 ppb; average 14.6 ppb ± 20.28) is obtained from under 80-mesh sub-177 micrometer fraction size but if there is enough fine-grained particle, the grain size should be sieved below 100 mesh (149 microns) or 200 mesh (74 microns); **(ii)** gold values increases with decreasing particle size so that there is a reverse relationship between the gold values and the grain size; and **(iii)** Bathe technique gives the second best result in terms of gold content. The authors therefore concluded that smaller the

particle means higher the gold values and this is attributed to degree of liberation. This conclusion is cited to be consistent with the general characteristic of epithermal gold mineralization. The other important conclusion of this work is that the Bathe technique is also an appropriate methodology for sampling the stream sediments as shown by the fact that the second highest the gold content comes from the samples taken by the Bate method. It has also been shown that, in exploration of epithermal deposits hosted in volcanic rocks, the particle size of stream sediments should be below 177 microns.

Kerim Şener *et al.* (2009) documented brief information about two low-sulfidation epithermal deposits in the Sındırgı district: Kızıltepe and Tavşan deposits. The former is low-sulfidation Au-Ag deposit and comprises several subvertical to steeply-dipping NE-SW-trending en échelon quartz veins hosted within Miocene dacitic-rhyodacitic ignimbrites. The latter is a low-sulfidation Au-Ag-Sb deposit that develops along a thrust fault between upper Cretaceous ophiolites in the upper plate and Jurassic limestones in the lower plate. Jasperoide horizon hosts the mineralization. NW-SE-trending steeply-dipping (normal?) fault cuts the jasperoide horizon and controls the distribution of high-grade Au and Sb occurrences. The NW-SE-trending faults are interpreted to play a significant role in Au-Ag-(Sb) mineralization in both deposits. Authors have also highlighted the role of stratigraphy and position of hosting rock units in controlling location and style of mineralization.

Hüseyin Yılmaz *et al.* (2013) pointed out that Kızıltepe forms an example of quartz-adularia low-sulfidation epithermal gold-silver deposited in volcanic rocks in Sındırgı (Balıkesir) district. There are also other prospects in the near east of the Kızıltepe deposits and they include Kepez, Kavaklıduz, and Karaduz prospects. The Kızıltepe LS deposit is characterized by **(i)** quartz-adularia veins with typical LS-related vein textures, like colloform, crustiform, cockade and carbonate replacement textures as quartz pseudomorphs after bladed calcite; **(ii)** vein breccia with quartz matrix and **(iii)** massive chalcedony. Gangue minerals are fine- to coarse-grained quartz, adularia, chalcedony and calcite, while disseminated pyrite and Fe-oxide with electrum, acanthite, Au-rich acanthite, and Ag-Hg-Au-Tl-Te-Pb compounds in trace amounts

50

from the main ore minerals. Illite/smectite, dickite and nacrite forms the common alteration minerals whereas precious metal minerals are acanthite, Au-rich acanthite, and Ag-Hg-Au-Tl-Pb series; pyrite is the most common opaque mineral. Authors have established a hydrothermal temporal sequence and suggested that mineralization has evolved in three main phases: **(i)** phase I, coarse-crystalline quartz, illite and pyrite with minor precious metals; **(ii)** phase II, economically the most important major Au-Ag forming phase and is composed of medium- crystalline quartz that shows characteristic LS textures of crustiform banding, carbonate replacement, and hydrothermal breccia; and **(iii)** phase III, fine- crystalline chalcedonic quartz with characteristic colloform/crustiform banding. The authors have studied the fluid inclusions to describe the nature and genesis of main mineralizing phase II: the mineralization is produced from relatively low salinity (0.5-4.8 wt% NaCl equiv.) predominantly vapour- to liquid-rich hydrothermal fluids at homogenization temperatures (Th) of 157°C to 330 (clustering between 190°C and 300 °C) and ice-melting temperatures (Tm) of -0.2 to -2.9 °C. The deposition is attributed to boiling of a volatile-rich fluid with subsequent dilution and drop in salinity due to the loss of volatiles. They have dated two samples from lower and upper units: groundmass separates from these rocks have yielded 40Ar/39Ar plateau ages of 18.96±0.11 Ma and & 19.82±0.14 Ma, and isochron ages of 19.05±0.11 Ma and 20.91±0.21 Ma, respectively. Similarly, adularia from the quartz veins have yielded 40Ar/39Ar plateau age of 18.27±0.11 Ma and isochron age of 18.50±0.05 Ma; accordingly, age of mineralization is assigned at 18.3±0.2 Ma.

Ömer İ. Ece *et al.* (2013) studied Düvertepe high sulfidation epithermal kaolininite and alunite deposits located on the western end of the Simav Graben; it is one of the largest known fossil hydrothermal kaolinite deposits in Turkey. Kaolinite and alunite reserves are hosted within the Miocene rhyolites-rhyodacites and tuffs. It is attributed to active faults that forms in association with ongoing N–S extensional tectonics. Thus, upward fan-shaped deposits of silicification and enhanced kaolinization commonly occur along fault zones. Silica sinters are present above the kaolin deposits

and mark outflow of geothermal waters above fracture systems that forms pathways for hydrothermal fluids to rise the surface. There two distinct occurrences described: **(i)** Şapçı-Arpatarla kaolinite- alunite- quartz deposits in the south of the Simav Graben; the has been active since early Miocene. They form in the western hanging-wall of a NW-SE trending fault zone situated about 2 km south of Şapçı. **(ii)** Düvertepe-Moren kaolinite (mostly halloysite) deposits in the north of the Simav Graben; they form along two small fault zones. The system results in halloysite-alunite-opal-CT-quartz mineralization. Authors have performed oxygen and sulfur isotope studies of alunite; K-Ar and 40Ar/39Ar ages are also obtained from alunite. The isotope values indicates that hydrothermal alteration occurred in the range of 38° to 129 °C. Both K-Ar and Ar-Ar ages are concordant and suggest that hydrothermal alteration in the south and north of the graben has occurred during early Miocene; 20.1-20.6 Ma and 17.3-19.2 Ma, respectively. The main conclusion of this paper is that steam-heated hydrothermal fluids are sourced from the early Miocene rhyolitic magma and caused formation of Düvertepe kaolinite-alunite deposits thorough metasomatism.

As seen from these studies, there is not much done about the structural control of low-sulfidation epithermal Au-Ag mineralization in the Sındırgı district. This thesis therefore aims to contribute to the better understanding of controlling structures of the epithermal vein- type mineralization in Kızıltepe LS epithermal mineralization and to propose a model that may explain the localization of ore formation in this particular area.

CHAPTER 2

SINDIRGI PROSPECT

The Kızıltepe low-sulfidation Au-Ag deposit occurs within the early Miocene Bigadiç borate basin that develops over the rocks of the İzmir-Ankara suture zone (Figures 1.15, 1.16 and 2.1). The basin is part of a volcanic large volcanic field, named as Bigadiç-Sındırgı volcanic field (Figure 1.16; cf. Dilek & Altunkaynak 2009). The stratigraphy, tectono- magmatic evolution and structures of the Bigadiç borate basin were studied by Fuat Erkül in the frame of his PhD research (Erkül 2004); he published a number of papers as well (Erkül *et al.* 2005a, b, 2006). There are many other publications about the basin (Helvacı & Alaca 1991; Helvacı 1995, 2015; Helvacı & Alanso 2000; Erkül 2004; Yücel-Öztürk *et al.* 2004; Ersoy *et al.* 2011; Koç-Taşgın & Diniz-Akarca 2018; Koç-Taşgın *et al.* 2018) but Erkül's work is the most comprehensive and therefore following information will be a brief summary of his work (Erkül 2004).

2.1. Rock Units: Bigadiç Borate Basin

The Bigadiç borate basin develops over the Bornova Flysch Zone (the basement rocks), a kind of sedimentary mélange, made up of variably-sized blocks of Mesozoic limestone, spilites, cherts and serpentinised peridotites that occur within a chaotically deformed and intensely sheared matrix of turbidites and micritic limestone lenses. The age of flysch zone, based on the age of youngest limestone block and unconformably overlying oldest unit, is assigned as late Maastrichtian-Palaeocene. The Lower-Middle Eocene Başlamış Formation unconformably overlies the various lithologies of the Bornova Flysch Zone. It commences with basal conglomerates made up of rounded ultramafic clasts, continues upward into finer clastic sediments, and then to shallow-marine nummulitic reefal limestones with sandstone- mudstone-marl intercalations. Oligocene clastics unconformably overlie the Başlamış Formation. These lithologies are interpreted to form the basement to the Bigadiç borate basin and overlain

unconformably by the oldest/lowest lithologic association of the basin fill, volcanogenic sediments of the Kocaiskan volcanics (Figure 2.2).
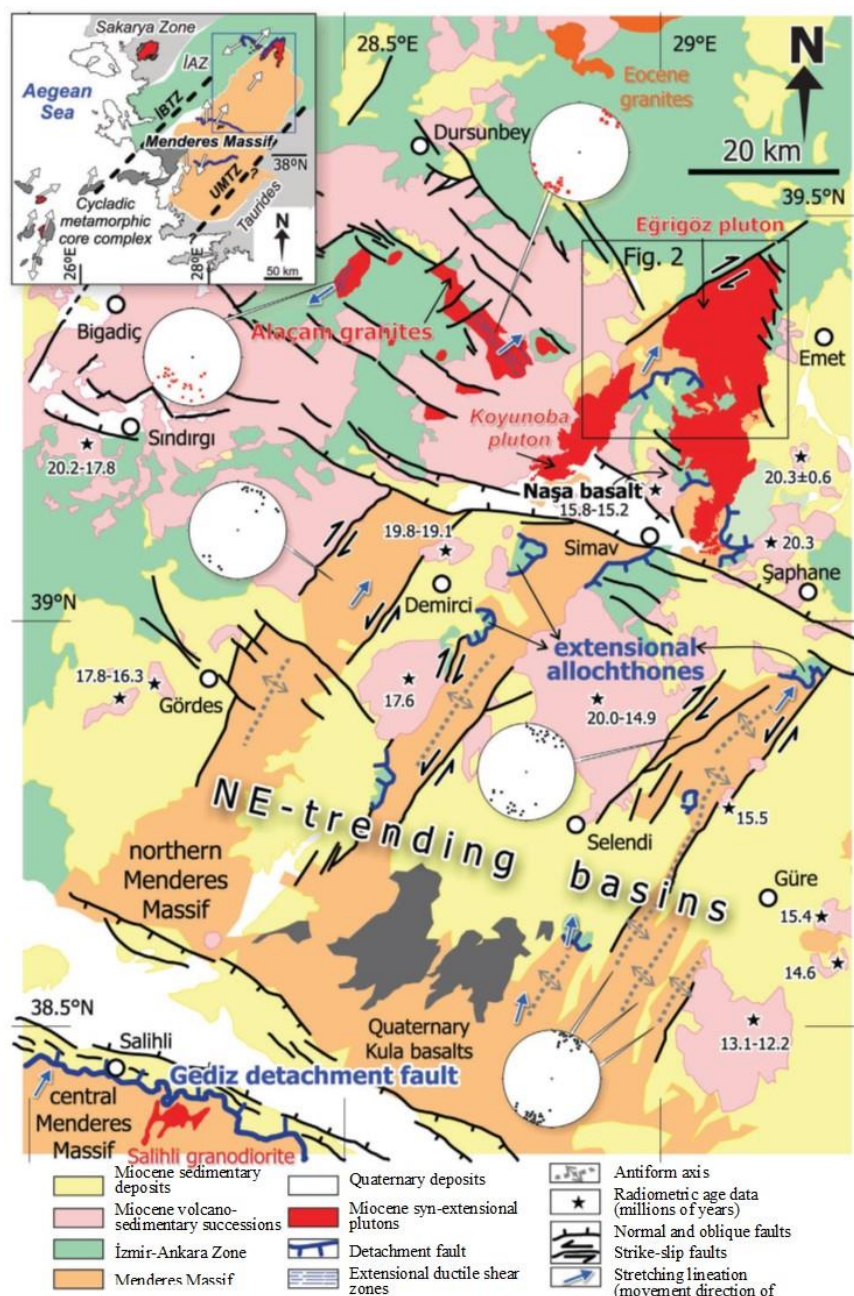
Figure 2.1. Geological map of western Turkey, showing its major rock units and structural elements. The inset map is the simplified tectonic map of the Aegean region and shows major tectonic units of western Turkey. Lower hemisphere equal-area stereographic projections of lineation patterns measured from footwall rocks of the Menderes Massif (black circle) and mylonitic rocks in the syn-extensional plutons (red square). IBTZ: İzmir-Balıkesir transfer zone. UMTZ- Uşak-Muğla transfer zone (from Erkül *et al.* 2017).

Figure 2.2. Generalized stratigraphic columnar section of the Bigadiç borate basin (from Erkül 2004; Erkül *et al.* 2005a).

The basin-fill overlies unconformably the basement and is represented by a succession of lacustrine and fluvial sediments with evaporates; the sedimentation was accompanied by extensive and intense volcanism that produced lava flows and

pyroclastic rocks. Numerous volcanic centers and many dome-like intrusions and dykes trend in NE-SW direction. The volcanism was episodic and has occurred in two distinct stages; the products of two phases are separated by a basin-wide unconformity. The second phase was accompanied with sedimentation.

The first phase is represented by andesitic intrusions and lavas, together with andesitic pyroclastic rocks, andesitic autobreccias and intercalated volcano-sedimentary (intercalation of volcanic breccia-conglomerate-sandstone) deposits; this succession is named as Kocaiskan volcanics and interpreted to be produced by stratovolcanoes during early Miocene. The products of the second phase comments with a basal conglomerate and are composed of basaltic to andesitic volcanics and intercalated calcareous and clayey sediments; this sequence is termed the Bigadiç volcano-sedimentary succession and is considered as syn-depositional volcanics formed synchronously with the filling of the basin. The felsic components are dacitic to rhyolitic lavas, ignimbrites and associated sediments - Sındırgı volcanics. During this time, olivine basalt (Gölcük basalt) and trachyandesites (Kayırlar volcanics) were emplaced along NE-SW-trending faults to form similarly trending dykes, domes and lava flows (Gölcük basalt). The peperitic textures within calcerous sediments form the best evidence for syn-depositional volcanic activity. The associated volcano-sediments comprise two distinct tuff horizons (lower and upper tuff units) and intervening two borate horizons (lower and upper borate units rich in borate minerals - colemanite and ulexite - within clay- dominated layers); there is a limestone horizon above the basal conglomerate. The volcano- sedimentary sequence consists mainly of lacustrine evaporitic sediments (claystone, siltstone, marl, and massive-laminated-locally silicified limestone) with acidic volcanoclastics, mainly volcanogenic sandstone. The final product of the volcanism is represented by basaltic andesitic intrusions and associated lava flows and autobreccias, the Şahinkaya volcanics (Figure 2.2).

The episodic first calc-alkaline, then coeval calc-alkaline to alkaline magmatism is interpreted to represent a transition from contractional to extensional regimes in

western Turkey. In this scenario, the early phase of calc-alkaline activity was coeval with possibly transpressional tectonic regime accompanying late orogenic N−S compression. The second phase of coeval calc-alkaline to alkaline is interpreted as the main bimodal magmatic phase and is attributed to post-orogenic extensional tectonics that commenced ca. 20−18 Ma. The Bigadiç borate basin was formed in a NE−SW-trending transtensional zone and was filled with volcanoclastics and accompanying borate-bearing lacustrine sediments. Many NE−SW- and NW-SE-trending strike-slip faults deformed and shaped the basin.

2.1.1. Kocaiskan Volcanics

Andesitic Kocaiskan volcanics forms the oldest rock association of the Bigadiç borate basin and are represented by a lava flows, pyroclastic rocks, associated volcanoclastic sediments and early- to late-stage intrusions (Figure 2.2). They unconformably overlie the basement rocks and are overlain unconformably by the Bigadiç volcano-sedimentary succession. These volcanics were extruded from two distinct volcanic centers and represent the earliest products of early Miocene magmatism in western Turkey. The unit is composed of a thick volcano-sedimentary sequence of lava flows, aurobreccias, pyroclastic rocks and interbedded conglomerate-sandstone layers. The early stage intrusions occur as andesitic domes or interconnected subvolcanic bodies that intrudes recrystallized limestones of the Bornova flysch. Late-stage intrusions are emplaced into, and form irregular bodies (domes) within, the volcano-sedimentary sequence. The unit is produced partly by effusive to explosive, possibly phreatomagmatic, volcanic activity; the products are pyroclastic flows, surge and fall (ash-and pumice-fall) deposits that are mostly composed of mainly subangular to rounded andesite lava and vesicular pumice clasts and some angular lithic fragments within ash matrix. Surge deposits are mostly composed of cross-bedded layers of andesitic lithic and vesicular pumice fragments. The volcanogenic succession is represented by clast-supported volcanogenic breccia, conglomerate (agglomerate) and sandstone; these lithologies show both lateral and vertical passages to one another. They show typical syn-sedimentary structures like normal- and reverse-grading, cross-

stratification, scour-and-fill features. The (lava) domes form spherical to ellipsoidal bodies that are aligned in ENE−WSE-direction (070°N). They form prominent topography and are represented by hilltops. Domes are mostly associated with massive and autobrecciated lava flows, pyroclastics, volcanogenic breccia and sandstone. Volcanic breccias are typically polymictic and composed of variably-sized (up to block size) angular to subrounded lava clasts. Pyroclastics are mostly ignimbrites and contain pumice and minor lithic clasts within an ash matrix. Lava flows shows flow bands and display pervasive sub-vertical cooling joints. Volcanogenic sandstones form distinct layers within the succession and mostly contain dolomitic lenses, clay beds and intercalated laminated limestones.

2.1.2. Bigadiç Volcano-sedimentary Sequence

The Kocaiskan volcanics are unconformably overlain, with a basin-wide angular unconformity, by a volcano-sedimentary succession of up to 700 m (Figure 2.1). It is represented by **(i)** a borate-bearing evaporitic lacustrine carbonates, clay-dominated sediments and intercalated volcanoclastic sediments (tuff units) and **(2)** volcanics - mainly felsic (dacitic and rhyolitic) intrusions and associated lava flows and, basalt and trachyandesite syn- depositional intrusions.

The volcanics comprises four units; these, from oldest to the youngest, are Sındırgı volcanics, Gölcük basalt, Kayırlar volcanics and Şahinkaya volcanics (Figure 2.1). Basic characteristics of these volcanics will be summarized in the following paragraphs.

Sındırgı volcanics comprises dacitic and rhyolitic intrusions in the form of domes and associated massive and autobrecciated lava flows, and pyroclastic deposits. The lavas and volcanoclastic sediments display both vertical and lateral passages from one another. These volcanics are represented by three distinct rock assemblages: **(1)** Rhyolitic domes, intruding the basement rocks and the Kocaiskan volcanics only, associated massive and autobrecciated lava flows with volcanoclastics. Dome rocks are porphyritic and composed of abundant biotite and plagioclase phenocrysts. Lava

flows are characterized by subvertical flow banding and, display very fine crystalline, vitric flow and devitrification (spherulites) textures. The volcanoclastics consists of tiny pumice and angular to rhyolite clasts set within an ash matrix. **(2)** Dacitic domes and associated massive-and-autobrecciated lava flows and abundant welded to non-welded ignimbrites form the second group of rocks. Domes and associated lava flows are commonly emplaced within NE-SW-trending zones. Porphyritic texture is characteristic and defined by plagioclase, sanidine, biotite, amphibole and quartz phenocrysts; enclaves of basement rocks are also common. Ignimbrites locally display columnar jointing and contain abundant flattened pumice clasts with few andesitic lava and metamorphic rock fragments. **(3)** Rhyolitic domes and dykes (associated with autobrecciated lava flows and pyroclastic rocks) intrude the products of the second dacitic phase and the Kocaiskan volcanics. Subvertical cooling joints are common in domes. Argillic alteration, silicification and iron staining form characteristic alteration products.

Gölcük basalt is represented by NE–SW-trending brownish olivine (phenocrysts) basalt dykes and vesicular lava flows. They intrude the Kocaiskan volcanics and wet lacustrine sediments where peperites and lava-sediment breccias are common. Amygdaloidal texture with secondary calcite, quart and zeolites is characteristic. Widespread quartz veins, recrystallized carbonates and iron-oxides form evidence for intense hydrothermal alteration in association with the basaltic intrusions.

Kayırlar volcanics occur as NE–SW-trending andesitic-trachyandesitic dykes and associated lava flows. The porphyritic texture is evident with plagioclase-hornblende-biotite (±pyroxene) or sanidine-plagioclase (±quartz) phenocrysts within a microcrystalline matrix. Mafic enclaves are also common. Mafic (olivine basalt) enclaves are common. Peperites and lava breccias are characteristic where they intrude the limestones. Subsidiary intrusions perpendicular to, and brecciated margins along, main dykes are observed. Associated lava flows display sub-horizontal cooling joints. Hydrothermal alteration and hydrobrecciation associated with intrusions are common in the close vicinities.

Şahinkaya volcanics occur as andesitic and basaltic andesitic brownish-grey circular domes, dykes and associated with lava flows, autobreccias and pyroclastics. They represent the youngest products of the volcanic activity and occur in a ca. N−S corridor. Subvertical cooling joints in domes are common. They are typically porphyritic with plagioclase, biotite and amphibole phenocrysts. Lava flows and intercalated autobreccias and tuffs occur around the domes. Autobreccias are composed of angular andesitic and basaltic andesitic lava fragments within lava matrix. Borate-rich sediments are divided into five units (Helvacı 1994) as lower limestone unit, lower tuff unit, lower borate unit, upper tuff unit, and upper borate unit (Figure 2.2).

The lens-shaped lower limestone (ca. 90-m thick) unit is composed of creamy-whitish dolomitic limestone and intercalated volcanogenic sandstone beds with quartz-plagioclase- biotite grains within a carbonate matrix. The unit gradually passes into the lower tuff unit (ca. 150-m thick). The unit is represented by volcanoclastic pile of massive-to-normally graded debris-flow deposits, pumice breccias, ash-fall tuffs and interbeds of lacustrine sediments; these lithologies show both intercalations and lateral passages to one another. Debris-flow deposits are composed of volcanic mineral grains (quartz, plagioclase, biotite and hornblende), pumice, lithic clasts, and limestone fragments. Pumice breccias occur as pyroclastic flows and, are composed of largely sub-rounded pumice clasts and minor dacitic lava fragments in an ash matrix. Ash-fall tuffs are massive, display characteristic conchoidal fractures, and contain tiny biotite grains. Zeolites are common within the lower tuff unit. Conformably above comes the lower borate unit (ca. 130-m thick). The non- to poorly stratified upper tuff unit (ca. 400-m thick) overlies conformably the lower tuff unit and, is composed of subrounded greenish fibrous pumice clasts and few angular lithic clasts within an ash matrix. Upper borate unit is ca. 110-m thick and represents the uppermost lithologic association in the borate-bearing evaporitic lacustrine sedimentary sequence in the Bigadiç borate basin. Both the lower and upper borate units share similar lithologic association and are composed of massive-laminated

limestone, marl, claystone and quartz-bearing volcanogenic sandstone intercalations. Silicified limestone with chert nodules occurs in the upper levels. The clay-dominated parts contain economical borate minerals; the thicknesses of the borate-bearing horizons are 65 m and 30 m, respectively. Syn-sedimentary structures, like slump folds, attest the tectonic activity during sedimentation.

Age of these intrusions associated volcanic rocks are reported as: **(i)** 20.2±0.5 Ma and 19.0±0.4 Ma biotite and hornblende K-Ar ages from rhyolites and dacites of the Sındırgı volcanites; **(ii)** 20.5±0.1 Ma and 19.7±0.4 Ma Ar-Ar groundmass ages from the olivine-basalt of the Gölcük basalt; **(iii)** 20.6±0.7 Ma biotite K-Ar age from the NE-SW-trending trachyandesite dyke of the Kayırlar volcanites; and **(iv)** 17.8±0.4 Ma biotite and hornblende K-Ar age from andesites of the Şahinkaya volcanites. The age data suggests that the age of the Bigadiç volcano-sedimentary succession is constrained between 20.6±0.7 and 17.8±0.4 Ma (Erkül *et al.* 2005a).

2.2. Host Rocks: Deposit Lithology

The Kızıltepe low-sulfidation Au-Ag deposit forms the southwestern most mineralization within the so-called NE-SW-Sındırgı gold corridor that terminates against the Simav Fault (Figures 2.4). The deposit is located about 8 km northeast of Sındırgı district, near villages of Yusufçam, Yolcupınar and Çötürtepe; Çaygören Dam lies to the south of the deposit (Figure 1.14). The deposit occurs within the Sındırgı volcanics (Erkül 2004; Erkül *et al.* 2005a, b, 2006); Şener *et al.* (2006) named the unit as Sındırgı volcanic complex. The rock units in the deposit are therefore represented by a thick sequence of dacitic and rhyodacitic-rhyolitic massive welded pyroclastics (crystalline and pumice ignimbrites) and stock-like felsic intrusives as domes and dykes (Figures 2.3 & 2.5). Pyroclastics are divided into two as dacitic ignimbrites (lower ignimbrites) and rhyodacitic-rhyolitic ignimbrites (upper ignimbrites); a rhyolitic welded tuff unit separates two horizons. The dacitic ignimbrites are more crystalline whereas the rhyodacitic-rhyolitic ones are rich in pumice clasts and form fiamme ignimbrites; between the two ignimbrite units, there

is a horizon composed of tuff ash layers (Figure 2.6). The stratigraphy of the Kızıltepe deposit will be summarized from personal observations, literature (Yılmaz *et al.* 2013) and the company reports (Erhan Akay 2007; Duncan Stevens 2012; Carman & Groves 2013; Larcombe *et al.* 2013; Blanks 2014). Most data have been generated through all the stages of exploration from green field to feasibility study and mine operation to understand the stratigraphy, mineralization and structural elements within the deposit area.
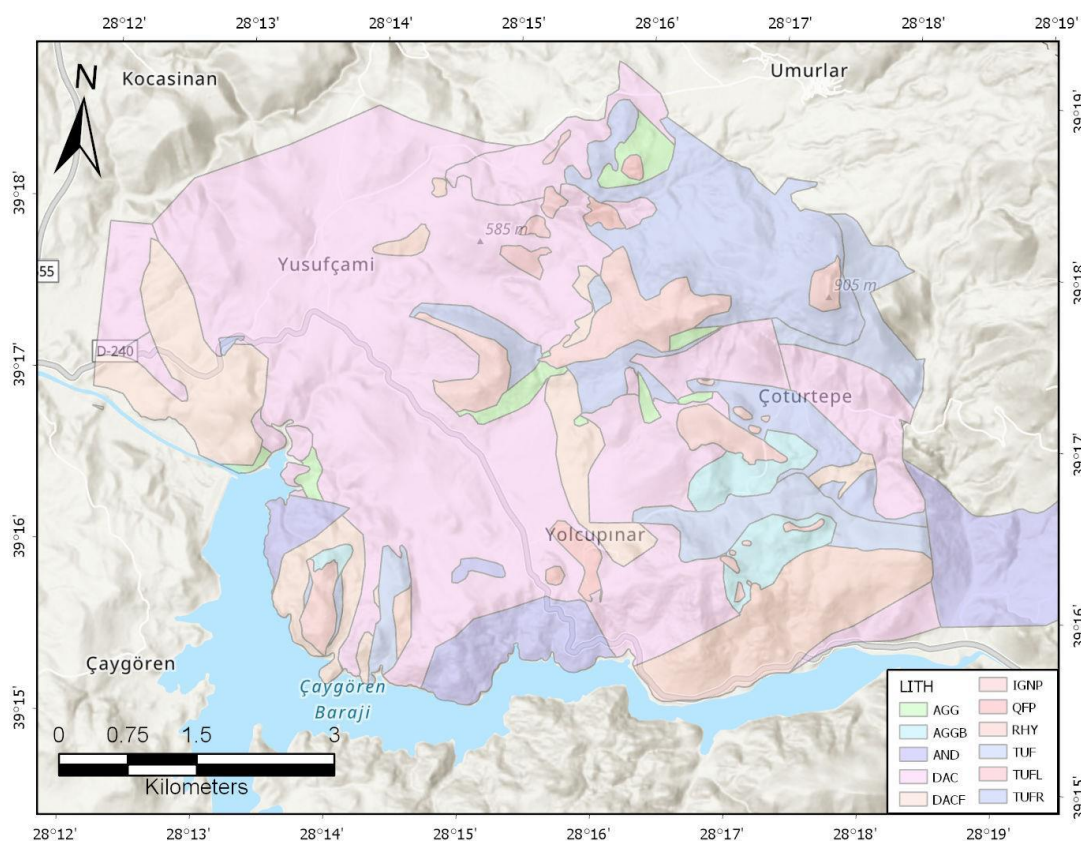
Figure 2.3. Geologic map of the Kızıltepe LS epithermal Au-Ag deposits and its surroundings, showing distribution of various rock units (redrawn from Carman & Groves 2013). AGG– dacitic volcanic agglomerate, autobreccia and coarse lapilli tuff; AGGB– polymictic bomb agglomerate with large dacite bombs; AND– massive andesite porphyry rich in feldspar phenocysts (no quartz) and well-bedded feldspar phyric andesitic tuff; DAC– medium to coarse crystalline quartz-feldspar dacitic ignimbrite; DACF– dacitic fiamme ignimbrite; IGNP– rhyolitic welded pumice ignimbrite; QFP– quartz-feldspar rhyolitic porphyry; RHY– fine-grained siliceous quartz rhyolite porphyry; TUF– rhyodacitic pinkish ash tuff; TUFL– medium- to very coarse-grained rhyodacitic lapilli tuff; TUFR– rhyodacitic white ash tuff (redrawn from Carman & Groves 2013).
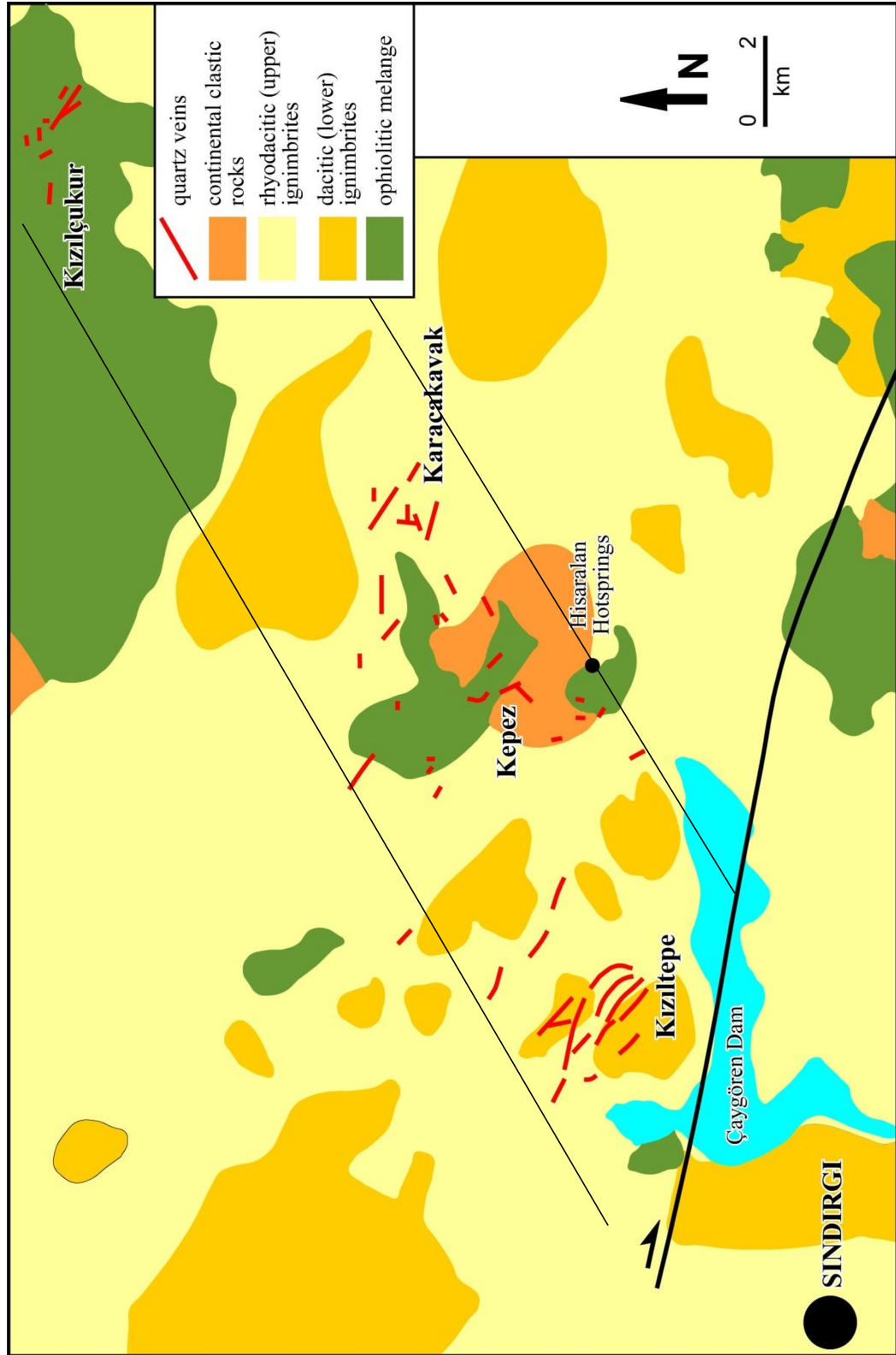
Figure 2.4. Geological map showing the Kızıltepe prospect in the south of the Sındırgı gold corridor (redrawn from Blanks 2014).

Legend:
- quartz veins
- continental clastic rocks
- rhyodacitic (upper) ignimbrites
- dacitic (lower) ignimbrites
- ophiolitic melange

Kızılçukur

Karaçakavak

Kepez

Hisaralan Hotsprings

Kızıltepe

Çaygören Dam

SINDIRGI

N

0 2 km
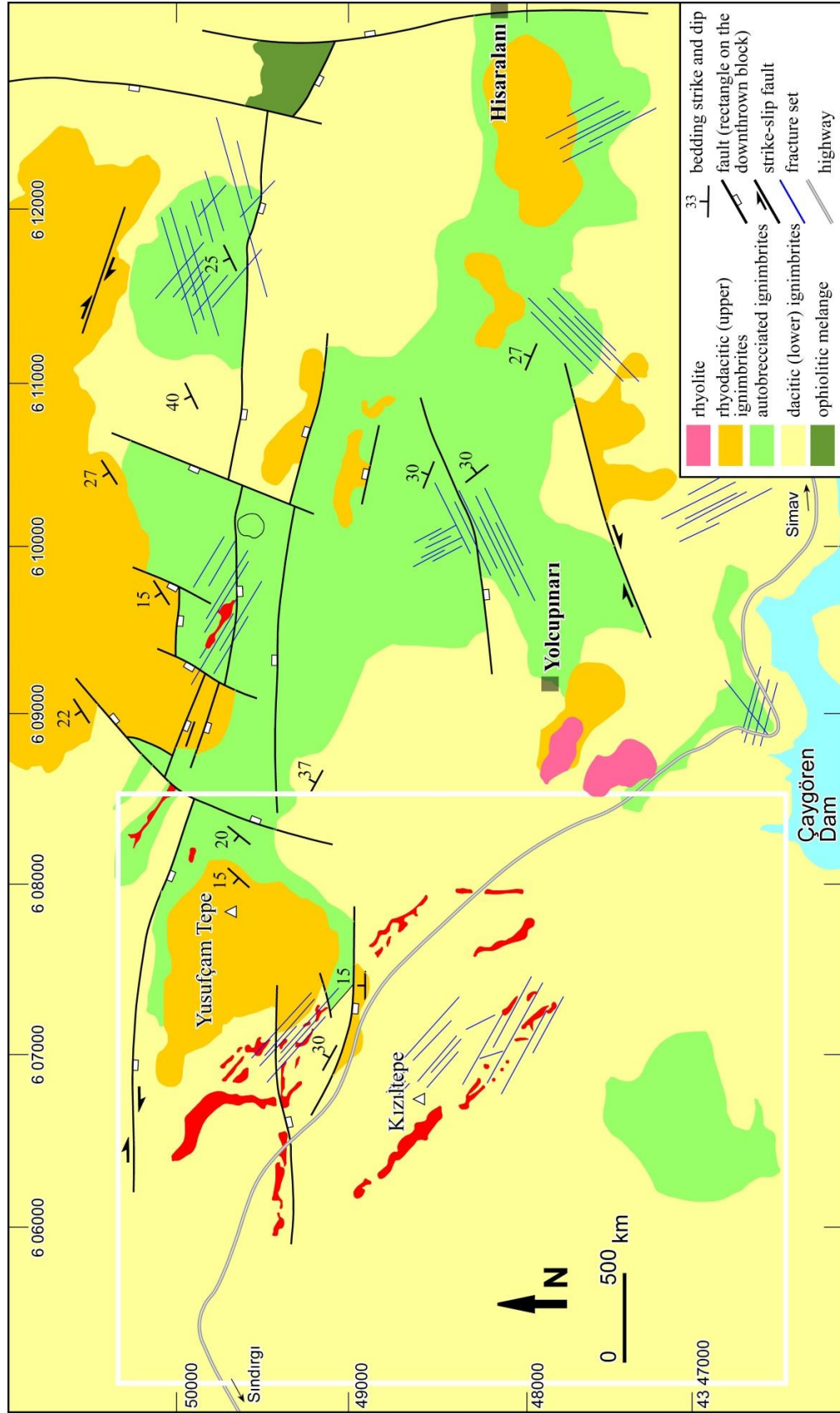
Figure 2.5. Geologic map of the Kızıltepe LS epithermal Au-Ag deposits and its surroundings, quartz veins in red (redrawn from Yılmaz *et al.* 2013).
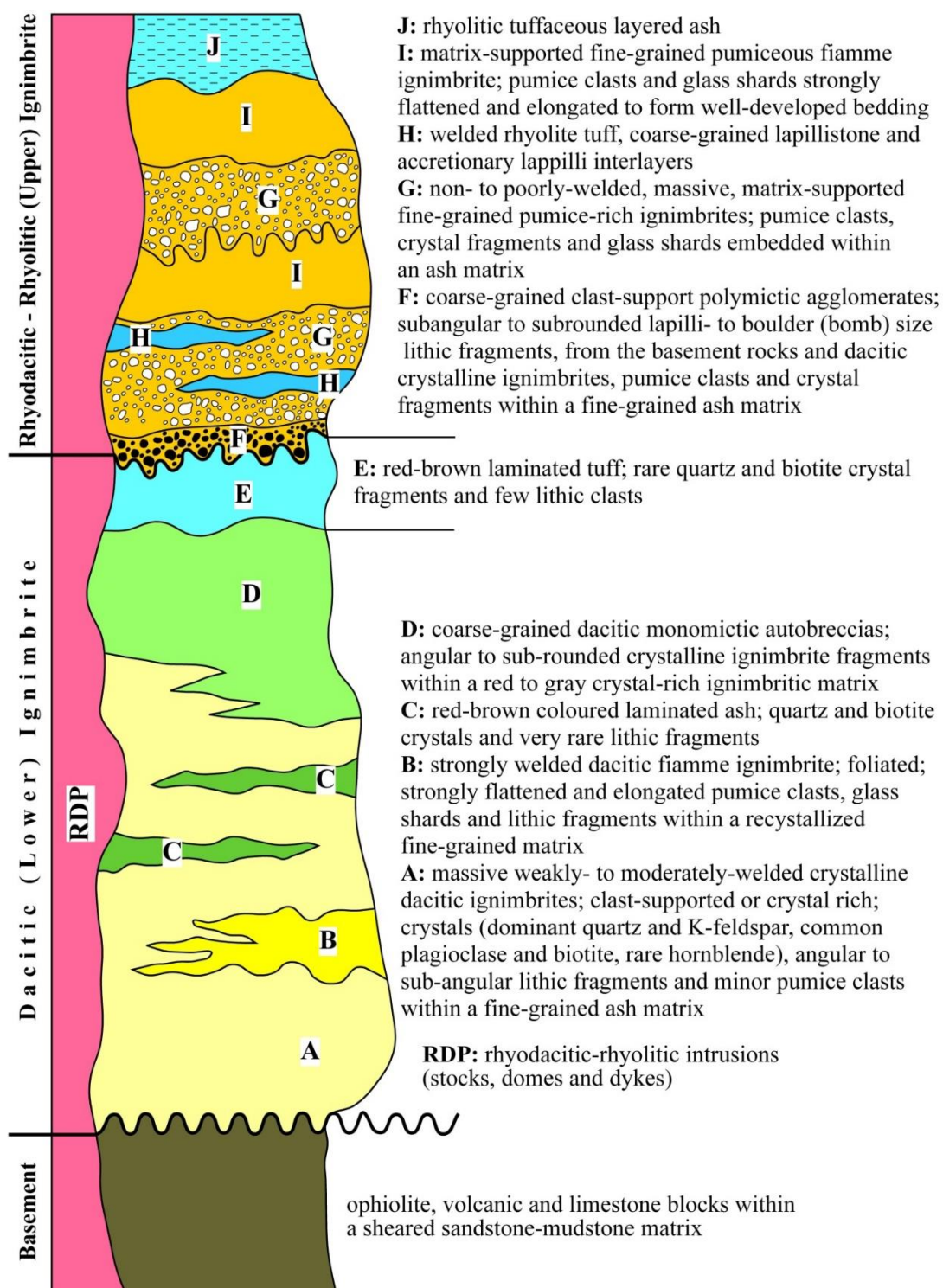
Figure 2.6. Stratigraphic column of the rock units in the Kızıltepe LS epithermal Au-Ag deposits and its surroundings (redrawn from Ekay 2007).

2.2.1. Dacitic Ignimbrites

Dacitic ignimbrites are represented by crystal-rich pyroclastic flow deposits and cover a large area in and around the Kızıltepe deposit (Figures 2.3 and 2.5). The lower parts of the unit are composed of mainly biotite-rich dacitic crystalline ignimbrites, they grade upward into fiamme ignimbrite; dacitic breccias/agglomerates and tuffs occur up in the succession. The unit is about 250–300-m thick. Common lithologies include quartz-feldspar crystalline ignimbrite, biotite crystalline ignimbrite, quartz-free crystalline ignimbrite, fiamme ignimbrite, and monomictic autobreccias (Figures 2.3 and 2.5)

The unit is characteristically reddish brown to grey in colour and forms mainly massive, locally thick-bedded, crystalline ignimbrites. The clast-supported/dominant (or crystal-rich) rock is typically composed of angular to sub-angular crystal and lithic fragments, with minor pumice clasts, within a fine-grained ash matrix. Matrix possess recrystalline textures in places. Quartz and K-feldspars forms the most dominant crystal phases; plagioclase and biotites are also common but hornblende is relatively rare. In places, where clast concentration is relatively low, the rock possesses a flow foliation; the wrapping of foliation around crystal fragments suggest flow mechanism and in places flow-direction can also be determined. The lower levels are mostly weakly to moderately welded. The degree of welding increases upward in the succession. Strongly welded levels occur in the middle parts of the succession. The fiamme texture is well developed and defined by strongly flattened and elongated pumice clasts, glass shards and lithic fragments within a recrystallized fine-grained matrix. The fiamme mostly occur as lozenge-shaped dark clasts and are aligned parallel to define a foliation (original bedding) in the rock. The recrystallization of the matrix may suggest that the fiamme formation is due to diagenetic compaction subsequent to the deposition.

> Fiamme, from the Italian word for flames (cf. Ross & Smith 1961), is a
> descriptive term that defines elongate lenses or domains of the same

mineralogy, texture and composition, and are separated by domains of different mineralogy, texture or composition. Fiamme are commonly found in welded ignimbrites, and aligned to define a pre-tectonic foliation (cf. Bull & McPhie 2007). Original definition of fiamme refers to 'strongly flattened pumice clasts', whereas broadened modern definition is any elongate, lenticular dark glassy juvenile clasts (pumice and bubble-wall shards, may sinter, anneal, or 'weld') that define a pre-tectonic foliation. Fiamme can be formed in a variety of ways, as welding in hot pyroclastic deposits, hot welding-compaction in pumice-rich pyroclastic fall deposits, diagenetic compaction - diagenetic alteration during compaction of non- welded, pumiceous, volcaniclastic facies and lavas (cf. Bull & McPhie 2007).

In addition to fiamme ignimbrites, the unit also contains a few-meters-thick laterally discontinues typically red-brown coloured laminated ash horizons (Figure 2.6). The crystal (mostly quartz and biotite) fragments are very rare, rock fragments are few.

The grain size increases upward in the succession, the crystalline ignimbrites grades both laterally and vertically into coarse-grained dacitic monomictic autobreccias (Figure 2.6). The poorly-sorted rock is composed of rock fragments that are derived from the underlying crystalline ignimbrites; the angular to sub-rounded clasts are set in a red to gray crystalline ignimbrite matrix. The clast size is variable and ranges in the order of a few centimeters; larger fragments up a meter-scale are rare. Where clast content is less, moderate to weak welding is expressed by flattened and elongate rock fragments within a crystal-rich ignimbritic matrix.

Dacitic ignimbrites form the most important lithological association in the Kızıltepe LS deposit because they host the mineralized veins.

2.2.2. Rhyodacitic-Rhyolitic Ignimbrites

These pyroclastic flow deposits are represented by mainly white-yellow coloured pumiceous ignimbrites that display a well-developed fiamme texture; they are

therefore termed as fiamme ignimbrites. The maximum observed thickness of the unit is ca. 200-m thick. The best exposures occur in the Yusufçamı Tepe. Common lithologies include polymictic boulder agglomerate, bomb agglomerate, non-welded pumice and fiamme ignimbrite, pinkish tuff, white to pinkish ash tuff and lapilli tuff (Figures 2.3 and 2.5).

The unit is represented by a fining-upward sequence of block- and ash-flows to massive non- welded pumiceous to fiamme ignimbrites, and finally to bedded tuffs. It commences with coarse-grained polymictic agglomerates above the underlying dacitic ignimbrites along an irregular surface. The clast-support rock is composed of lithic fragments, which are derived from the basement rocks and underlying dacitic crystalline ignimbrites, pumice clasts and crystal fragments set in a fine-grained ash matrix. The clasts are mostly subangular to subrounded; clast size is variable, but may reach up to lapilli- to boulder (bomb) size.

The coarse-grained basal unit grades gradually upward into fine-grained pumice-rich ignimbrites; the well-bedded lithology displays locally cross-bedding. The unit is matrix supported and, is composed of pumice clasts, crystal fragments and glass shards embedded within an ash matrix. The degree of welding and compaction vary vertically and laterally within the unit. The lower levels are commonly non- to poorly-welded and occur as massive pumiceous ignimbrites. Then, comes a well-welded horizon where the pumice clasts and glass shards are strongly flattened and elongated to form fiamme; the rock is a foliated fiamme ignimbrite and characterized by a foliation/bedding defined by the parallel alignment of fiamme. Above the fiamme ignimbrites comes a second level of non- to poorly-welded massive pumice-rich ignimbrite. These ignimbrite horizons with varying degrees of welding- compaction represents different pyroclastic flows during volcanic activity. Rhyodacitic ignimbrites consist of local occurrence of welded rhyolite tuff, coarse-grained lapillistone and accretionary lappilli interlayers. These interlayers are coarse-grained at the bottom and grades upward into finer levels. They have irregular erosive lower contacts and indicate different pyroclastic fall and flow phases. Local occurrence of

cross-bedding is also observed. Bedded welded rhyolitic tuffaceous layered ash horizon occur at the top of the sequence. At Yusufçam Tepe, tuffs appear to cover pumice ignimbrites and autobreccias of the underlying dacitic ignimbrite (Figure 2.6). Tuffs are composed of compacted and occur as typical consolidated volcanic ash and spherical and elliptical ejecta (volcanic crystal phenocrysts). Spherical and elliptical ejected volcanic crystal phenocrysts occur in some layers and suggest that the rock is lapilli. Ash horizon shows upward grading with larger fragments at the bottom.

2.2.3. Rhyodacitic-Rhyolitic Intrusives

Multiple massive felsic intrusions (stocks/domes) occur throughout the ignimbrite sequence and cut into the pyroclastic rocks. All are characterized by steeply dipping to subvertical flow foliation and are surrounded by associated autobreccias. They display typical porphyritic textures with euhedral to subhedral quartz, K-feldspar, biotite and amphibole phenocrysts within a siliceous (fine-grained crystalline quartz) to glassy matrix. They are named as quartz porphyry with sulfides, siliceous rhyolite porphyry (lake rhyolite intrusion), quartz rhyolite porphyry (Yolcupınar), quartz-feldspar porphyry (Belkoz; feldspar phenocryst within a fine- grained crystalline quartz and glassy matrix) and porphyry with mafic affinity (Figures 2.3 and 2.5). The siliceous rhyolite porphyry is fine-grained with quartz (possibly opaline) and glassy microcrystalline matrix; it displays characteristic devitrification with spherulites; pyrite traces are also reported. Some of the intrusions have chilled margins within and purple banded baked margin in the dacitic country rocks. Dacitic intrusion(s) are commonly fine-grained, porphyritic with large K-feldspar and quartz phenocrysts, and may have small black euhedral biotite or greenish black hornblende crystals.

2.3. Structural Geology of Kızıltepe District

Four major sets of faults are described in and around the Kızıltepe LS epithermal deposit. These include approximately WNW–ESE- (080–090°N), NE–SW-, NNE–SSE- and WSW–ENE-trending faults (Figures 2.3, 2.5, 2.7 and 2.8). The faults

are inferred from stratigraphic relationships, linear alteration zones or poorly preserved fault planes.

WNW–ESE-trending and south-dipping appear to be major structure dissecting the deposit area from west to east. The tips of the fault are marked by extensive and strong alteration, confirming that it was used as pathways for hot-warm hydrothermal fluids. Argillic alteration at the western tip, and propylitic alteration in the eastern tip are characteristic. Apart from this major structure, there are a number of smaller similarly-trending fault segments occur in its hanging wall (Figures 2.3, 2.5, 2.7 and 2.8). These fault segments are also marked by along-strike moderate to strong argillic alteration. Considering all fault segments, the total vertical displacement along these WNW–ESE-trending faults is reported as ca. 250 m. Slickenlines on small exposures of fault planes have rakes of ca. 20°W and suggest that the fault is a dextral fault with normal component (Akay 2007). Despite of Akay's contention, Carman& Groves (2013) suggest that the slickensides show generally vertical motion. This major structure is here named as Kızıltepe fault (Figures 2.7 and 2.8).

This fault appears to share similar trend with the Simav Fault and may be genetically related. Similar ca. E–W faults are mapped in the north (Bigadiç fault) and in the south (Gamze fault) (Figures 2.7 and 2.8).

The NE–SW-trending faults form the second prominent structures in the region. They form a number of parallel to sub-parallel fault segments and, cut and displace the major WNW-ESE- trending oblique-slip dextral fault (Figures 2.7 and 2.8). These structures are named as Sındırgı, Umurlar, Saylan, Kepez south, Hisaralanı and Hisaralanı west faults (Carman & Groves 2013).

There is a major NNW–SSE-trending, west-dipping fault cuts and displaces the major WNW–ESE-trending fault to the east of Çötürtepe; it is interpreted as the eastern boundary structure of the Kızıltepe deposit. No fault planes are observed but weak to argillic alteration is reported along the last two fault sets. Two segments of WSW–ENE-trending faults are also mapped to the south of the map area (Figures 2.7 and 2.8).
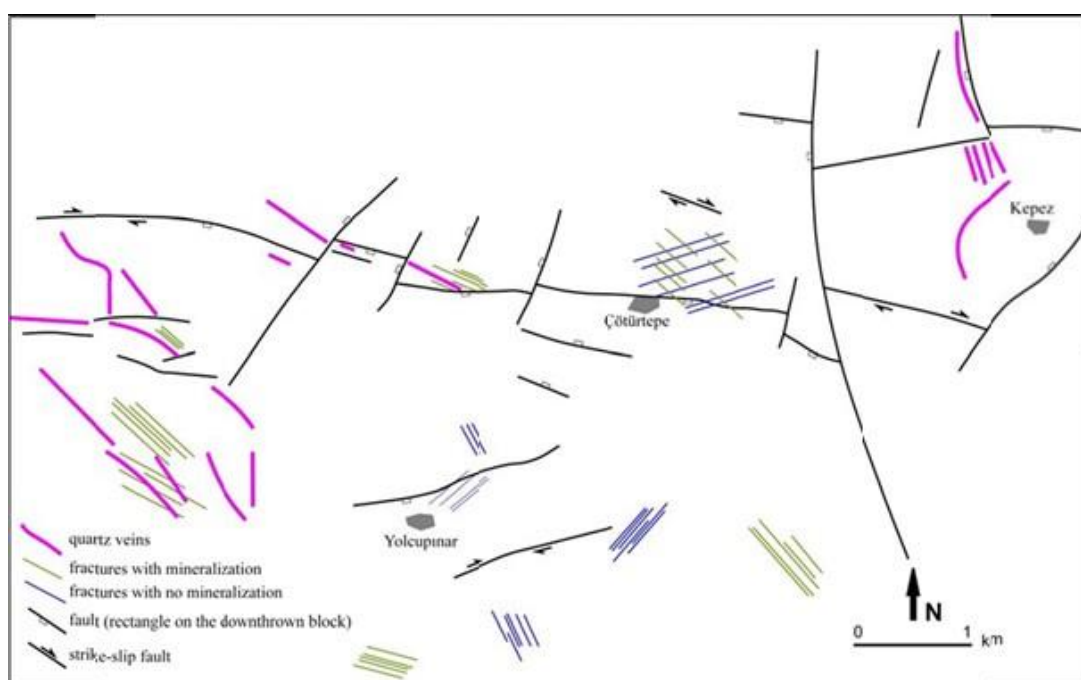
Figure 2.7. Fault map of the Kızıltepe LS epithermal Au-Ag deposits and its surroundings (redrawn from Akay 2007).
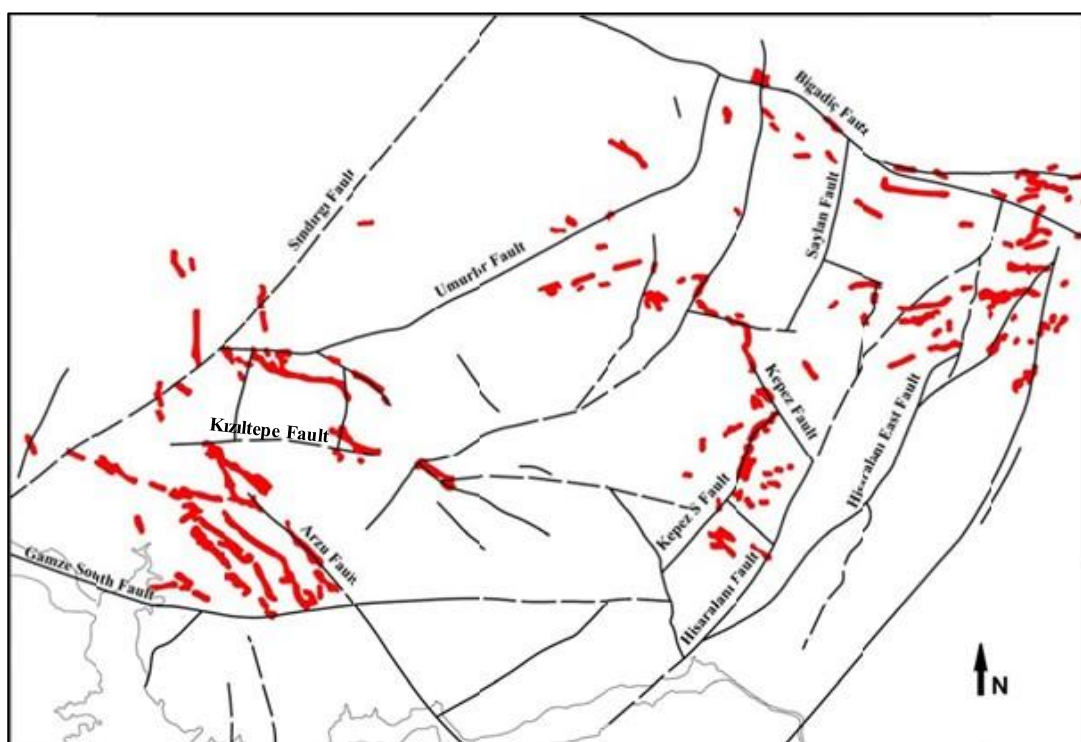
Figure 2.8. Fault map of the Kızıltepe LS epithermal Au-Ag deposits and its surroundings (redrawn from Carman & Groves 2013).

According to Akay (2007), all of these faults have considerable strike-slip motion with minor normal component whereas Carman & Groves (2013) suggest that slickensides show generally vertical motion. This is an important contrasting observation by two different schools and need to be clarified during this study.

Several NE–SW- and NW–SE-trending fracture sets are also mapped. Many of the fractures have no alteration and/or fillings but NW–SE structures occur as dilatational fractures and contain many quartz or calcite fillings. Gold-bearing quartz veins also trend in NW–SE direction (Figure 2.9).
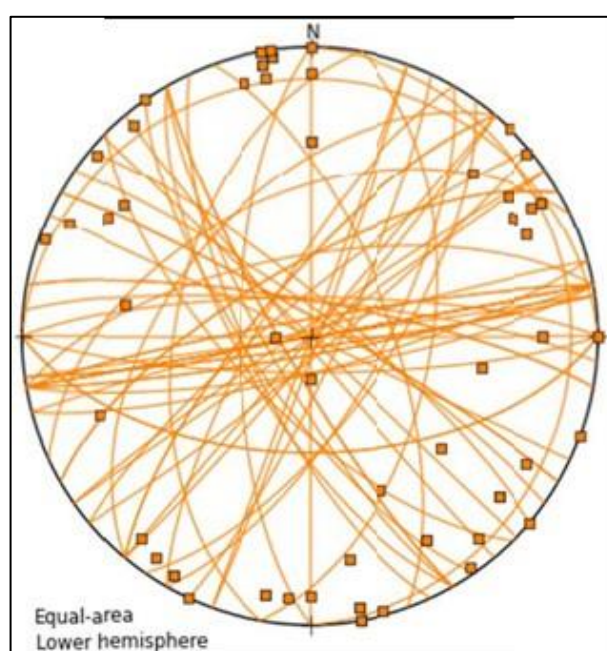
Figure 2.9. Faults and fractures from Kızıltepe deposit area plotted as great circles and poles to planes on an equal area stereonet. Three sets, ca. E–W-, NW–NE- and NE–SW-trending structures appear as dominant while N –S-trending structures are rare. are common across all three areas (from Carman & Groves 2013).

2.4. Epithermal Veins

Epithermal veins form the most spectacular structures of the Kızıltepe LS deposit; they are mainly hosted by dacitic crystalline (lower) ignimbrites. They occur in multiple orientations but NW–SE-trends form the most dominant orientation (Figure 2.10). They form steeply dipping to subvertical (80° to 90°) en échelon extensional

fracture arrays and host auriferous quartz-adularia veins and veinlets. Vein zones are marked by fractured hydrothermal breccia, smaller (<10 cm) quartz stock works and intense alteration halo. White-yellow rhyolite dykes paralleling the gold-bearing quartz-adularia veins are also common in similar density; the contact relationships illustrate that quartz-adularia veins are relatively younger than the dykes (Figure 2.10). Small arrays of NNE–SSW-trending open fractures with no fillings are oriented almost vertical to the dominant vein direction.
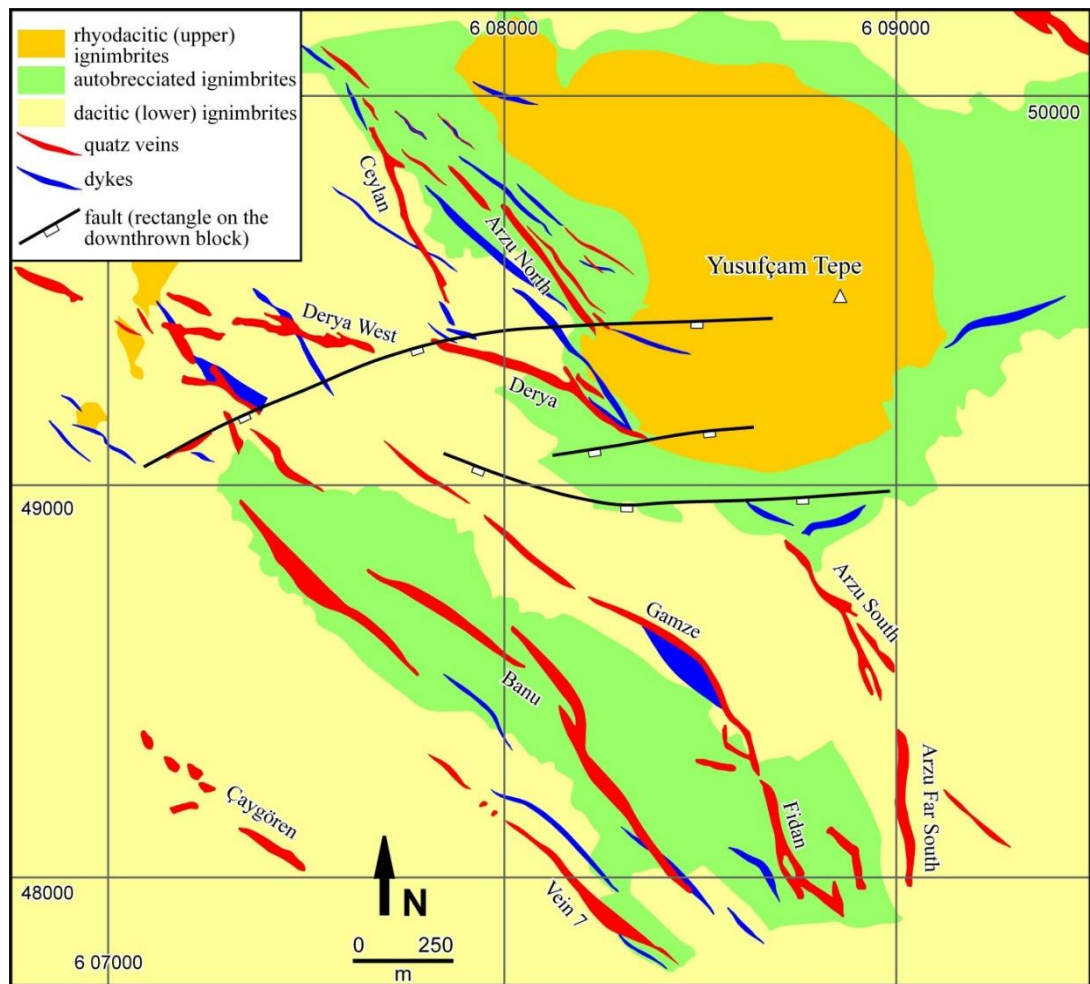
Figure 2.10. Geological map of the Kızıltepe prospect, showing locality and distribution of the Arzu North, Arzu South and Derya veins and rhyolite dykes (redrawn from Şener *et al.* 2006.)

The vein system is composed of several veins that show similar morphology and textural features; they are named after lady names Arzu, Banu, Ceylan, Derya, Derya West, Fidan, Gamze, etc... They form swarm of parallel to sub-parallel veins but stockworks are also common (Figure 2.10). Arzu vein has been divided into sectors as Arzu North, Arzu South and Arzu Far South. Among them, Arzu North and Arzu South veins are considered as the best target and the open- pit mine is now working along the Arzu South veins. Auriferous quartz-adularia veins display typical low-sulfidation textures, such as crustiform banded, colloform and cockade textures, bladed calcite and matrix- to clast-supported hydrothermal breccia; the highest gold grades are commonly associated with these textures.

The general orientation of the auriferous quartz-adularia veins and veinlets (Figures 2.11 and 2.12) also show a close-parallelism with the fractures and faults in the area; the good correlation suggests that the veins and fractures may genetically be related (Figure 2.13). There is however no correlation between the trends of major faults (WNW–ESE-trending Bigadiç and NE–SW-trending Sındırgı faults) and the vein-fracture population (Figure 2.14). This further suggests that the structural control on vein-forming processes and its possible relationship to these major structures need to be studied and explored. The present thesis therefore issues as well.

The width of veins is variable and ranges between 3 m and 6 m in average but may reach up to 14 m. They are quite persistent along strike up to ca. 1 km; they reach up to 2.5 km long. The vein margins appear sharp from a distance but when examined closely core and margins of the veins display transitional lateral boundaries where stockworks are common; then comes alteration halo around the veins.
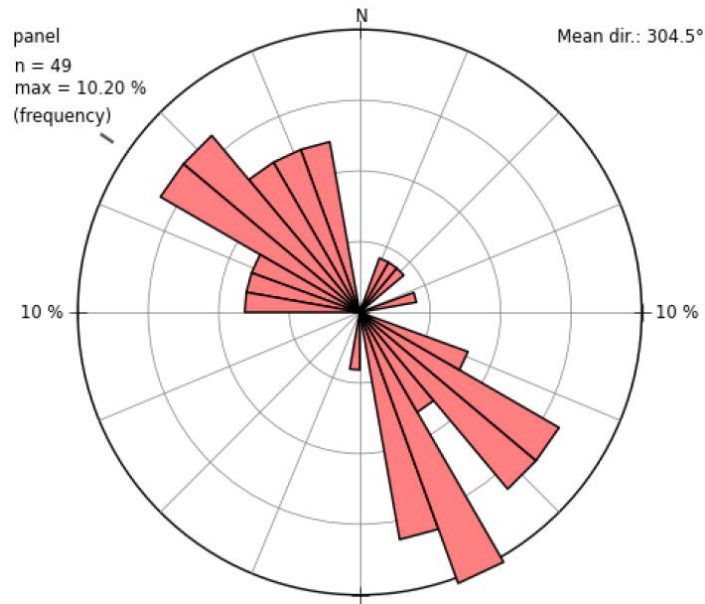
Figure 2.11. Rose diagram of epithermal veins in Kızıltepe LS Au-Ag deposit plotted with strike orientation. Average means are 135° and 304° (from Carman & Groves 2013).
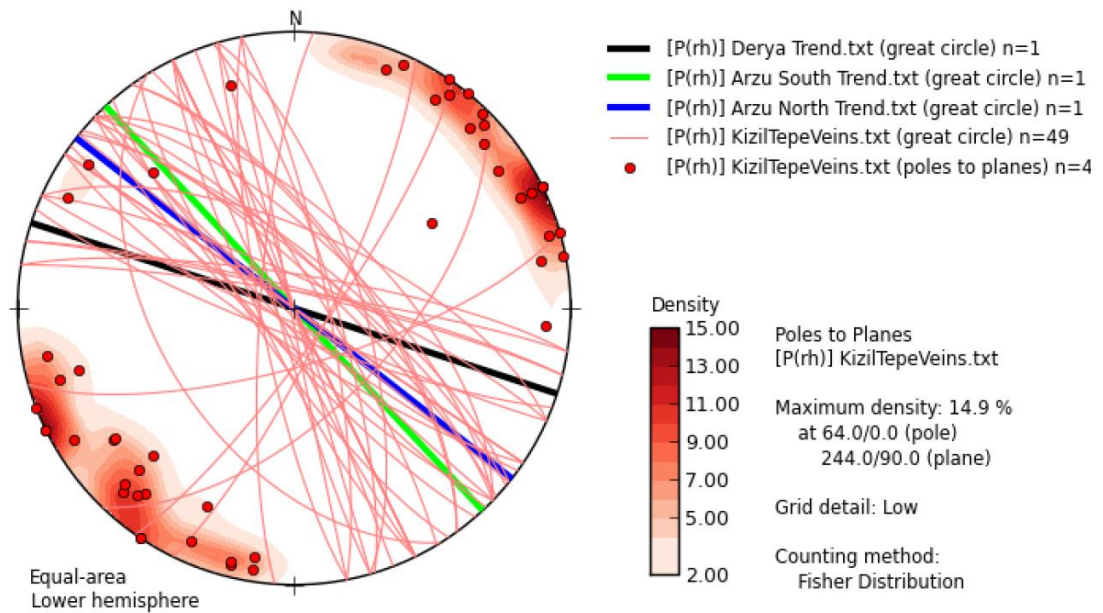
Figure 2.12. Stereonet of the epithermal veins in Kızıltepe LS Au-Ag deposit, plotted as poles to planes and great circles on an equal area (from Carman & Groves 2013). Note that the overall orientation of the veins shows a dominant NW–SE trend. Note also that the veins are subvertical structures dipping 80-90° to the NE or SW. The orientation of relatively small veins and veinlets show a close parallelism to the large-scale Derya, Arzu North and Arzu South veins.

75
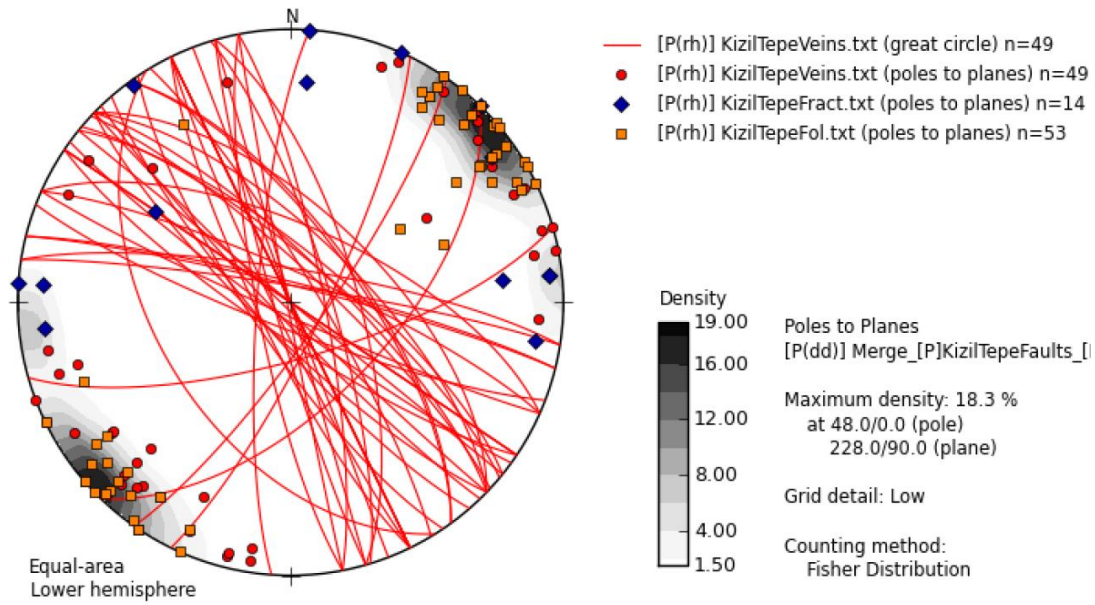
Figure 2.13. Stereonet of the epithermal veins, fractures and faults in Kızıltepe LS Au-Ag deposit, plotted as poles to planes and great circles on an equal area (from Carman & Groves 2013). Note good correlation among these structures.
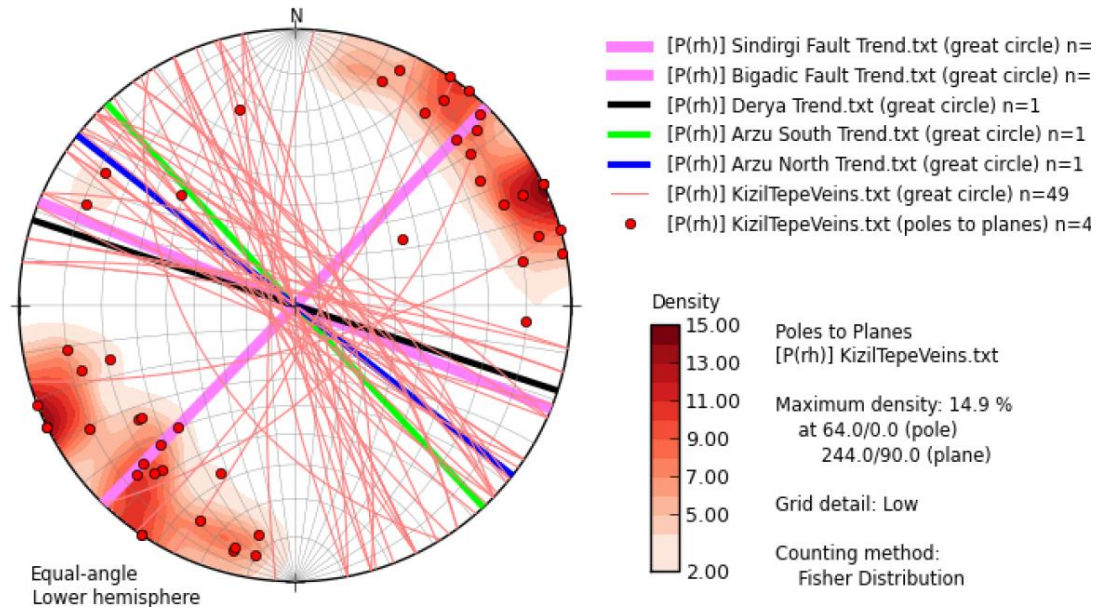
Figure 2.14. Stereonet of the epithermal veins, fractures and faults in Kızıltepe LS Au-Ag deposit, plotted as poles to planes and great circles on an equal area (from Carman & Groves 2013). The WNW–ESE-trending Bigadiç and NE–SW-trending Sındırgı faults are also included in the diagram. Note that there is no correlation between major and minor structures.

76

Veins are composed of quartz, adularite and chalcedony as gangue minerals; calcite is present, occurs as secondary mineral and forms either as distinct replacement bands or as fillings in vugs. Ore minerals occur as disseminations within veins and subordinate stockwork veinlets. They are mainly pyrite and Fe-oxides, and minor amounts of electrum, acanthite, Au rich acanthite, and Ag-Hg-Au-Tl-Te-Pb compounds (Yılmaz *et al.* 2013).

Almost all of the mineralized quartz-adularia veins display a zoned intense alteration halo, that is composed of typical low-sulfidation styles – silicification, argillic, and propylitic. Pervasive silicification is represented by coarse- and fine-grained quartz veins, veinlets and stockworks. Zoned argillic, sericitisation and propylitic alteration halo envelops the quartz- adularia veins. The mineral assemblages of the zoned halo, from the quartz vein outwards, contains quartz + adularia (minor) + illite, smectite with minor mixed-layer illite/smectite ± adularia, and cubic pyrite + chlorite + minor smectite (Yılmaz *et al.* 2013).

As is seen from the proceeding paragraphs in this section, the general orientation, mineralogy and composition of the veins are well studied but the kinematic analyses of the veins and their relation to major structures still waiting for clarification. The kinematic data obtained from the open pit mine along Arzu South vein will be presented in the following section.

CHAPTER 3

STRUCTURAL GEOLOGY OF THE KIZILTEPE
EPITHERMAL VEINS

The study area is located between 39°15' N – 39°20' N latitudes and 28°12' E – 28°19' E longitudes, 5 km northeast of Sındırgı town (Balıkesir); Çaygören Dam lies to the south and Yusufçamı village to the west (Figure 3.1).

The history of mining for gold goes back to 2000 years ago. Ancient mining galleries and trenches are still preserved. The first modern study was about the geology and hydrogeology of the region (Hafeli 1966). A mineral deposit specific study belongs to Oygür (1997); he described the epithermal mineralization at the near south of Mumcu village (Sındırgı) (see Section 1.7 for details).

Starting from 1990, Eurogold, Newmont, Tüprag and Kefi made regional exploration activities including BLEG (bulk leach extractable gold), 80 mesh stream sediment, systematic soil and rock chip sampling to locate and define epithermal mineralization within the prospective area. Ariana (Ariana Resources Plc) took over the license in 2005 and continue to exploration activities in order to evaluate an economic resource. Finally, the gold production has started in 2017 by Zenit Madencilik, joint venture company of Ariana and Proccea (Proccea Construction Co.).

This study area covers 45 km square in the so-called Kızıltepe region. This is the region where the most data have been generated through all the stages of exploration from green field to feasibility study and mine operation in order to understand the stratigraphy, mineralization and structural elements within the deposit area. The mine operation in the deposits still continues. This study aims to understand the control of structural elements within this well-defined epithermal mineralization.

Kızıltepe forms a typical example of a low-sulphidation epithermal Au-Ag deposit, characterized by numerous NW–SE- and NNW–SSE-trending subparallel auriferous quartz-adularia veins and associated stockworks, hosted by dacitic crystalline lower ignimbrite (Şener *et al.* 2006; Yılmaz *et al.* 2013). The vein system is composed of swarm of parallel to sub-parallel veins that are named as Arzu North, Arzu South, Arzu Far South, Banu, Ceylan, Derya, Derya West, Fidan, Gamze, etc... (Figure 3.1). Most study has been completed on the three epithermal veins namely Arzu, Banu and Derya. The poorly studied Ceylan and Fidan epithermal vein systems are not able to provide enough data for this study.
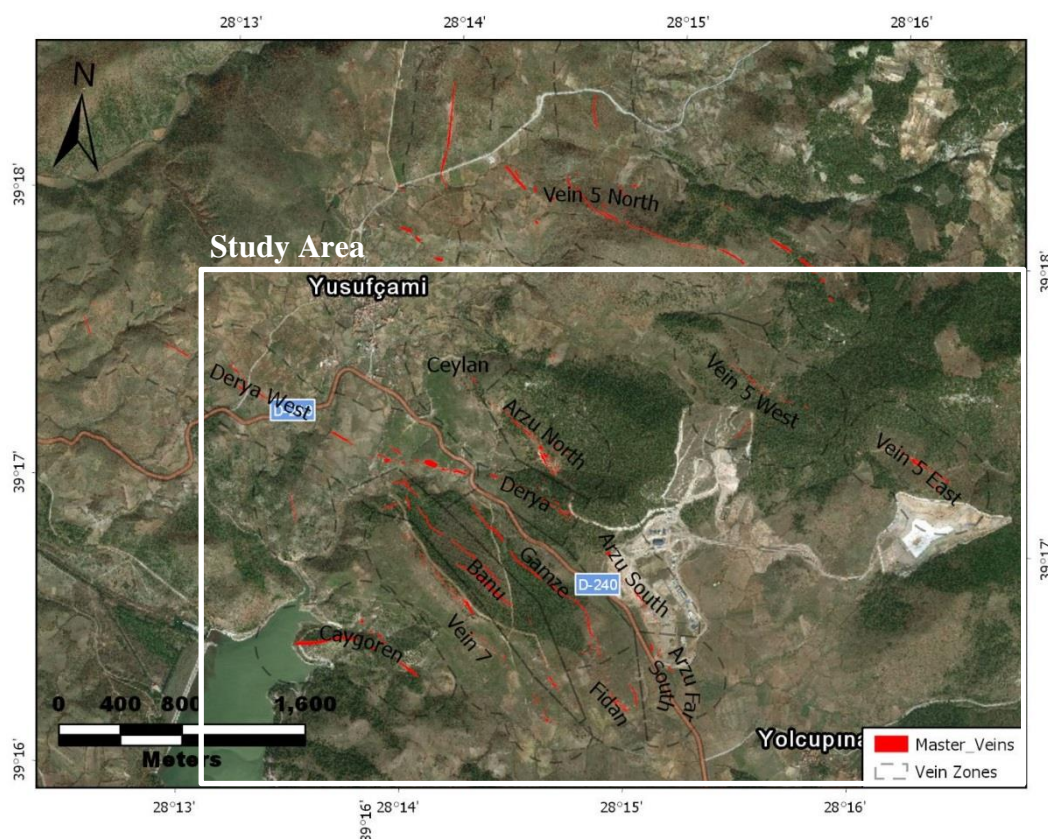
Figure 3.1. Google Earth image showing the distribution and naming of the Kızıltepe epithermal veins.

Structural control on the epithermal mineralization is the key information while exploring the sub- or none-cropping systems. All the Au-Ag-bearing quartz veins discovered till now are outcropping by the knowledge of surface geology (mostly lithological mapping) and geochemistry. During recent mining operation, the bench

80

faces provide best exposures to study vein orientation and in relation faults, which were not possible to identify prior to mining.

The study aims to define the major structural elements controlling the formation of the Kızıltepe low-sulfidation epithermal vein system. This why, the study area is kept limited with the location(s) where one can make observations about the controlling structural elements of gold mineralization. Arzu South open pit operation and its neighbouring region forms the best location where detail information about faults and their mutual relation to veins and structural elements are well studied. Within this defined region, three major sets of faults have been defined: **(1)** NW−SE-trending faults, they are observed as major syn-mineralizing structures, which have localized low-sulfidation epithermal quartz veining and, associated brecciation and stockworks; **(2)** N−S-trending faults and **(3)** E−W-trending faults that occurs as major boundary structures of the Kızıltepe LS epithermal deposit.

3.1. NW−SE-trending Faults

The NW−SE-trending faults occur as either bounding structures of, or at close vicinity of, similarly-trending auriferous quartz-adularia veins. Current mining operation is a great opportunity to survey and record the main fault in contact with Arzu South vein and associated breccias (Figure 3.2). Seven **(7)** measurements have been taken from the western bench wall at 310 m level. The steeply east-dipping fault plane is well preserved, polished and ornamented by slickenlines; striations, ridge-and-grooves and gutters suggest that it is an oblique-slip normal fault with minor dextral component. The corrugated geometry of the fault is well illustrated by along-strike variations where strike ranges between 311° N to 346° N, and dip is to the east with 75° to 90°. The rake angle of the slickenlines is variable from 65° to 80° from south, owing to the corrugated nature of the fault plane.

Another parallel fault plane is exposed (Figure 3.3), it shares very similar features with the other fault described in the preceding paragraph. Four **(4)** measurements confirm that it is a steeply (76°−84°) east-dipping corrugated fault plane. Well-preserved fault

plane displays slickenlines with rakes angles (65° to 73°) to the south, confirming its normal character with minor dextral component. The strike changes in short distances between 320°N to 335°N (Figure 3.3).

Similar structures also occur outside the Kızıltepe LS epithermal vein system area. Çaygören Dam is another location where NW–SE-trending fault(s) are observed, but this time without any mineralization. Çaygören Dam is located on one of the major E–W-trending fault, bounding the Kızıltepe en échelon vein system in the south. No mineralization localized along the E–W fault but there is evidence for along-strike alteration; it is interpreted as syn- to post-mineralizing structure. Two measurements from the southwest-dipping NW–SE fault suggests a dextral fault with normal component (Figure 3.4).

Figure 3.2. Field views from the Arzu South open pit 310 m level: Northwest–Southeast-trending pre- and/or syn-mineralizing normal fault with minor dextral component occurs at the contact of the main Arzu South low sulfidation Au-Ag quartz-adularia vein with field ID 317.
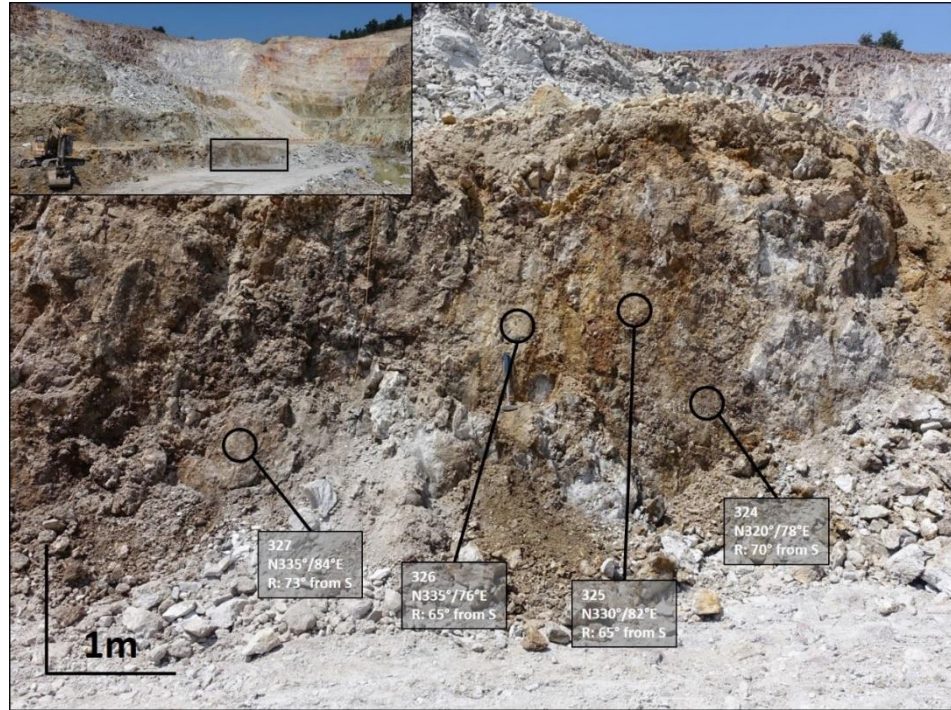
Figure 3.3. Field views from a NW−SE-trending pre- and/or syn-mineralizing normal fault with minor dextral component. It occurs at the contact of the main Arzu South low sulfidation Au-Ag quartz-adularia vein; field ID 324.
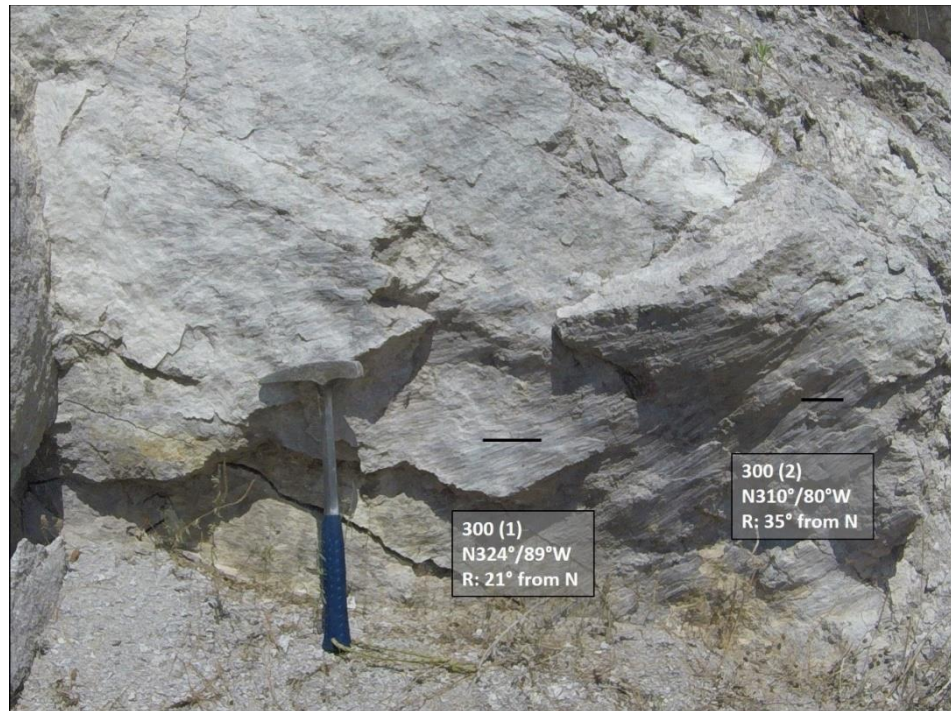
Figure 3.4. Field view from a NW−SE-trending fault to the north of Çaygören Dam; field ID 300. Two measurements are: 324°N/89°W, R= 21°N and 310°N/80°W, R= 35° N.

About 1.2 km west of above location, well-developed fault surface indicates the same NW–SE trend but with shallower dip angles of 35° to 44° to west. In this particular locality, the rake angles of 56° and 60° from north suggest a normal faulting with dextral component (Figure 3.5). However, along strike continuation of the same fault displays a west-dipping (55°) slickenside surface (320°–325°N) with almost horizontal slickenlines, suggesting a sinistral strike-slip motion (Figure 3.6). This fault forms the boundary the fiamme textured dacite and medium- to coarse-crystalline higher quartz (>5%) bearing dacite; it is here interpreted as a re-activated fault.

In another location at the Çaygören Dam site, a NW–SE-trending fault surface (344°N) dips steeply (75°). Rake angle of 55° from northwest suggests a normal movement with dextral component (Figure 3.7).

Figure 3.5. Field views from a NW–SE-trending normal fault with minor dextral component; north of Çaygören Dam with field ID 301. Two measurements are: 325°N/35°W, R= 60°N and 320°N/44°W, R= 56°N.
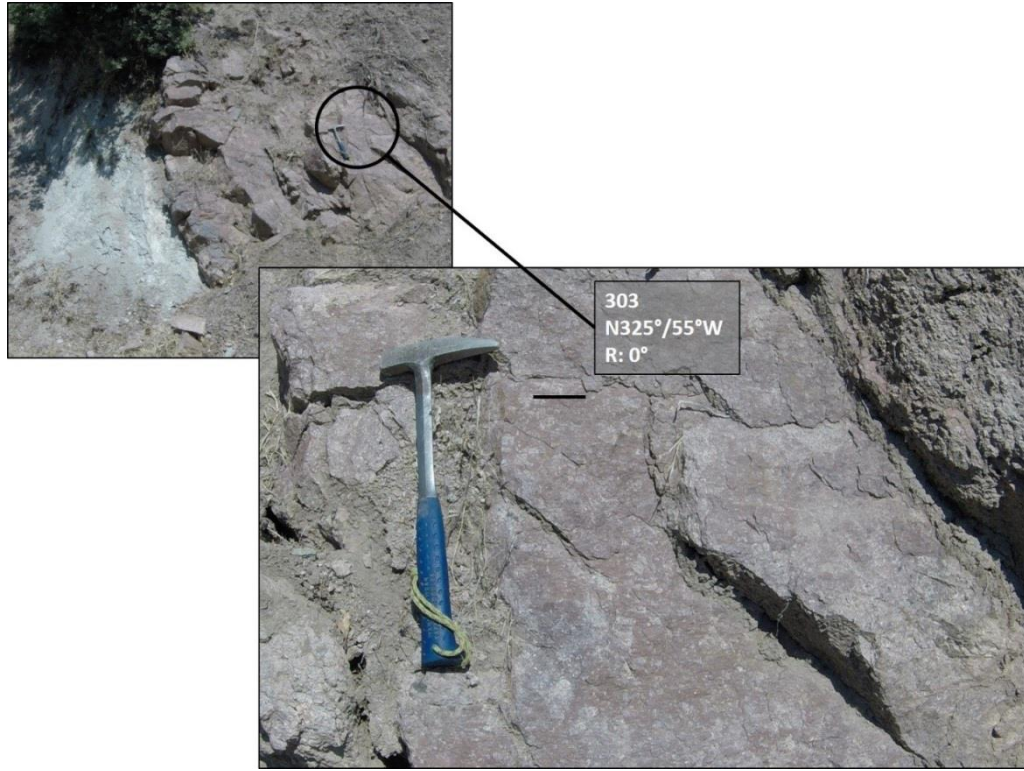
Figure 3.6. Field view from a NW–SE-trending sinistral fault; north of Çaygören Dam with field ID 303. 325°N/55°W, R= 00°.
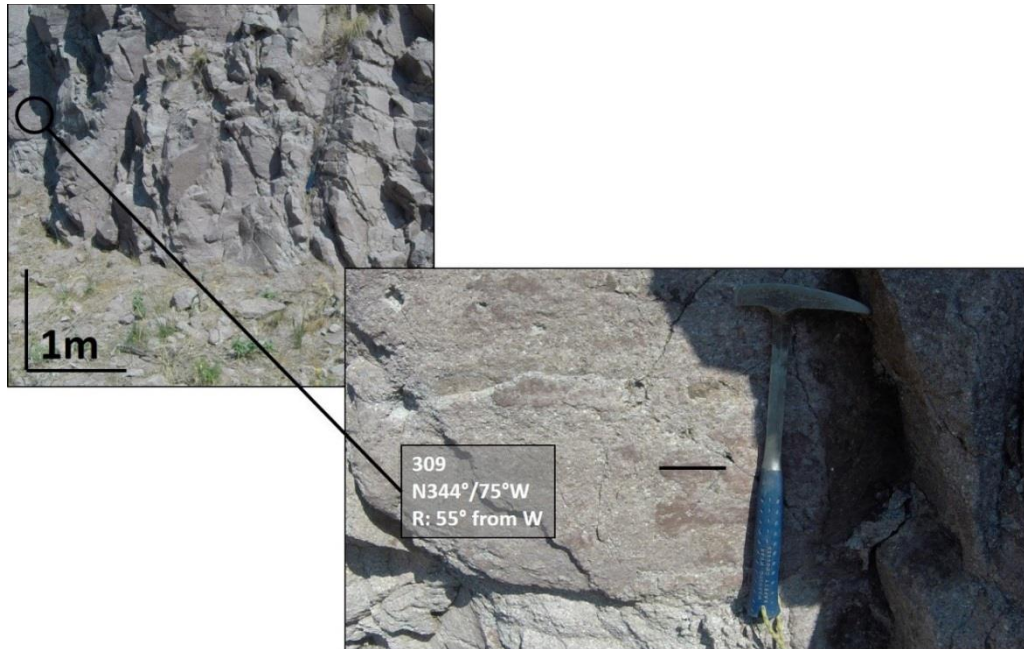
Figure 3.7. Field views from a NW–SE-trending normal fault with dextral component; north of Çaygören Dam with field ID 309. 344°N/75°W, R= 55°NW.

3.2. N−S-trending Faults

N–S-trending faults are not common in the study area and are just observed at two locations: **(i)** as an isolated fault at the north of Çaygören Dam site and **(ii)** about 1200 m east of Arzu South open pit. The fault surface of the former fault has an attitude of 192°N/70°E; the rake angle is 50° from south and indicates normal faulting with dextral component (Figure 3.8). The second fault plane strikes in N359°N and dips at 64° towards west; the rake angle is 60° from south and indicates normal faulting with sinistral component (Figure 3.9).

3.3. E–W-trending Faults

E–W-trending faults form the most conspicuous structures of the study area. They appear to occur as boundary structures of the Kızıltepe LS epithermal deposits from the north and south. They are therefore grouped in two as Domain A representing northern boundary faults while Domain B constitutes the southern boundary structures. These faults occur as corrugated structures and display dramatic along-strike variations. That is why the same structure may be observed as NE–SW and/or NW–SE fault planes in different locations along the general trend of the fault. Where exposed, the fault planes are well preserved, polished and ornamented by slickenlines; striations, ridge-and-grooves and gutters; shatter marks confirm the oblique-slip normal fault nature of the faults.

Figure 3.8. Field views from ca. N–S-trending normal fault with dextral component; north of Çaygören Dam with field ID 302; fault plane is 192°N/70°E, R= 50°S.

Figure 3.9. Field views from ca. N–S-trending normal fault with sinistral component; 1200 m east of Arzu South open pit with field ID 316; fault plane is 359°N/64°W, R= 60°S.

Group A: E−W-trending Northern Boundary Faults

Although the fault segments can be traced for several kilometres along strike, the well-preserved fault planes are rare. The well exposed slickensides occur in two distinct locations: about 1200 me east of Arzu South open pit and East of Çoturtepe village.

At east of Arzu South open pit on the road cut towards the tailing Dam, the corrugated fault plane is well exposed. The surface strikes in 284°N direction and dips by 56° to south; the rake angle is 70° from east and suggest a normal movement with sinistral component (Figure 3.10). This is an important observation because the same structure is mapped and interpreted as a dextral fault with rake angle of 20° from east (Akay 2007; Yılmaz *et al.* 2013). The repeating observations from the same structure in other localities form the robust evidence about the normal fault nature of this bounding structure; the tectonic significance of this observation will be elaborated in the Discussion Chapter.

East of Çoturtepe is also a very good location to observe and record structural data from a well-preserved fault plane that occurs along wide exposure. The slickensides, where preserved two sets of overprinting slickenlines. The fault plane strikes N265° and dips to the south by 45°. The dominant and younger slickenlines indicates a rake angle of 72° from east and suggest normal faulting with sinistral component (Figure 3.11).

Figure 3.10. Field views from ESE–ENE-trending south-dipping normal fault with minor sinistral component; 1200 m east of Arzu South open pit with field ID 314; fault plane is 284°N/56°S, R= 60°E. Note the pronounced corrugated geometry of the fault plane.

Figure 3.11. Field views from WSW–ENE-trending south-dipping normal fault with minor sinistral component; 300 m east of Çoturtepe village with field ID 294; fault plane is 265°N/45°S, R= 72°E. Note the pronounced corrugated geometry of the fault plane.

On the same outcrop, there are poorly preserved fault surfaces with slickenlines showing dextral normal faulting (Figure 3.11). The strike of the measured fault planes ranges between 245°N and 275°N whereas dip amounts are 60° to 90°; the rake angles are 49°–57°W and suggest normal faulting with dextral component.

As these slickenlines appear overprinted by the younger structures, this phase is attributed to an early motion along the same structures. Thus, the fault is interpreted as a reactivated structure with an early motion of normal faulting with dextral component and a late normal faulting with minor sinistral component.

Along the same fault in the east of Çoturtepe, the corrugated nature of the fault plane is very well illustrated by three parallel well-developed fault surfaces ornamented with slickenlines. The strike of relatively low- to moderately southeast-dipping (20° to 47°) fault planes varies from 205°N to 237°N (Figure 3.17). In this particular locality, the dip amount of the fault plane changes along dip direction and the fault displays small-scale flat-ramp geometry. Rake angles ranges between 55° and 60° from northeast, and suggest a normal movement with sinistral component.
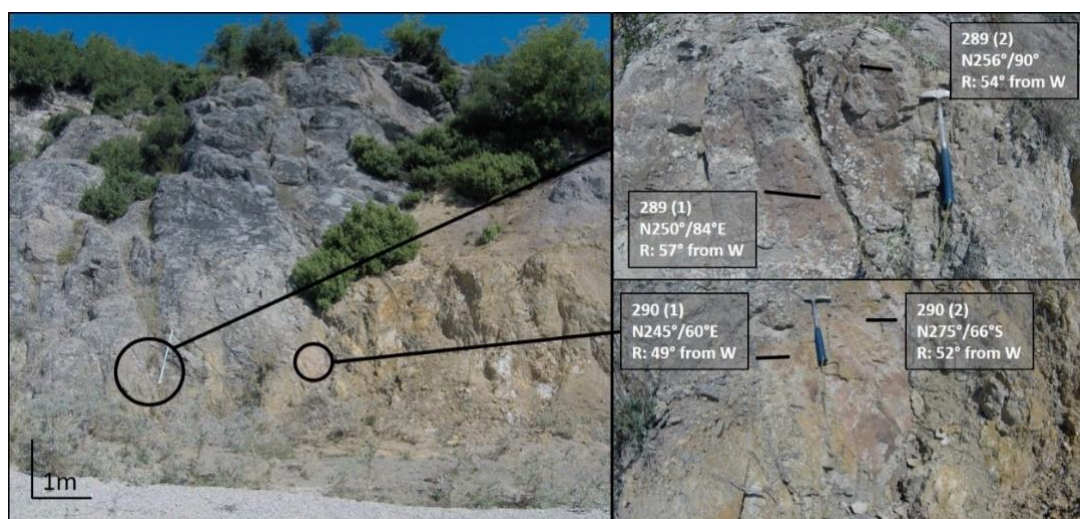
Figure 3.12. Field views from WSW–ENE-trending south-dipping normal fault planes with dextral component; 300 m east of Çoturtepe village with field ID 289-290; fault planes are: 250°N /84°S, R= 57°W; 256°N/90°, R= 54°W; 245°N/60°S, R= 49°W; 275°N/66°S, R= 52°W. Note the pronounced corrugated geometry of the fault plane.
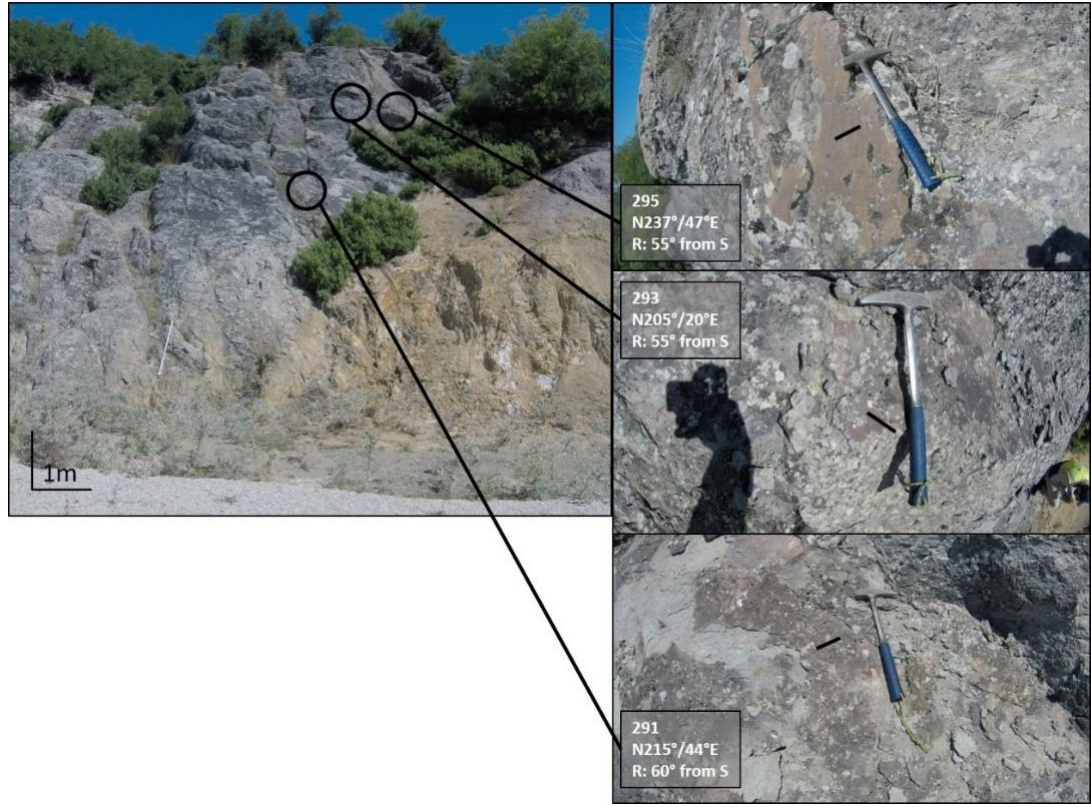
Figure 3.13. Field views from NE–SW-trending east-dipping corrugated normal fault planes, suggesting a normal fault with sinistral component; 300 m east of Çoturtepe village with field ID 291, 293 and 295; fault planes are: 237°N/47°SE, R= 55°NE; 205°N/20°SE, R= 55°NE; 215°N/44°SE, R= 60°NE. Note the pronounced corrugated geometry of the fault plane.

Similarly, a part of E–W-trending fault is well-exposed along the road cut formed during the road construction of the tailing Dam, located 1200 m east of Arzu South pit. Here, the fault strikes in NW–SE direction and dips westward by 60°; the rake angle is 75° from southeast and suggest a normal fault with sinistral component (Figure 3.14).

Figure 3.14. Field views from NW–SE-trending southwest-dipping normal fault with minor sinistral component; 1200 m east of Arzu South open pit with field ID 315; fault plane is 316°N/60°SW, R= 75°SE.

Group B: E–W-trending Southern Boundary Faults

Likewise, all the observation locations at the north of Çaygören Dam suggest normal and strike-slip movement with sinistral component (Figure 3.15, Figure *3.16* and Figure *3.17*). These structures are interpreted to form the southern boundary structure of the Kızıltepe LS epithermal deposit. They also show evidence for hydrothermal fluid flow and circulation as there is alteration developed along the trace of the fault. The strike direction of fault planes varies between 259°N and 276°N, whereas dip amounts are 50° to 74° to south. The fault plane shows two sets of slickenlines: an early strike-slip motion (Figure 3.15 and Figure 3.16) is overprinted by a later normal faulting with sinistral component (Figure 3.17).

Figure 3.15. Field views from ca. W–E-trending south-dipping strike-slip fault; north of Çaygören Dam with field ID 306; fault plane is 265°N/50°S, R= 00°.
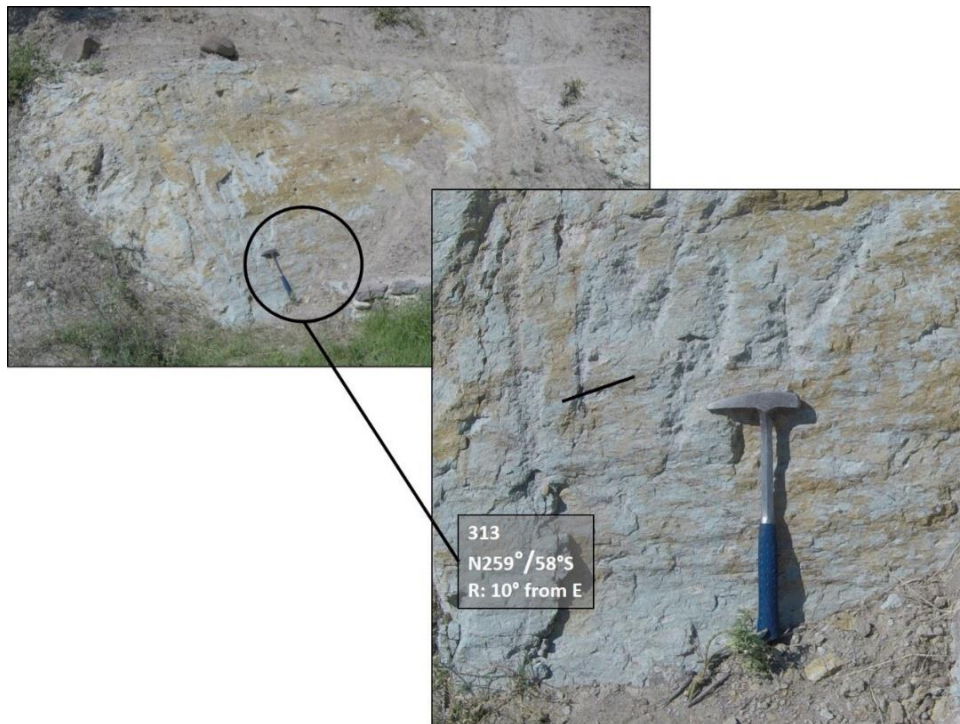
Figure 3.16. Field views from WSW–ENE-trending south-dipping syn-mineralizing dextral strike-slip fault; north of Çaygören Dam with field ID 306; fault plane is 259°N/58°S, R= 10°E.

Figure 3.17. Field views from ca. W–E-trending south-dipping syn-mineralizing normal fault with sinistral component; north of Çaygören Dam with field ID 305; fault plane is 276°N/74°S, R= 50°E.

3.4. NE–SW-trending Faults

Similar to northern boundary fault, the ca. E–W fault along the northern margin of Çaygören Dam also displays along-strike variations due to its corrugated geometry. A well-preserved fault plane in this particular locality trends in NE–SW direction (221°N) at the eastern end of the Çaygören Dam; the fault dips eastward by 40° (Figure 3.18); the rake angle is 00° and suggest a dextral motion. This geometry is attributed to the early dextral motion along the fault plane. The strike-slip motion is overprinted by a normal motion, where the fault strikes in 235°N and dips 74° to east; the rake angle is 85°N and suggests an almost pure normal motion (Figure 3.19). The eastern continuum of the same fault has an attitude of 060°N/65°S; the rake angle is 42°E and suggests normal faulting with sinistral component (Figure 3.20).

At the northern end of Çaygören Dam, a well-preserved fault plane is exposed along a 10-m wide outcrop. The measured fault planes have strikes ranging from 243°N to 248°N and dips from 51° to 60° towards SE. The slickenlines indicates two stages of movement: an early dextral motion and an overprinted normal faulting with sinistral motion (Figure 3.21).

It is therefore concluded that ca. E–W-trending and south-dipping northern and southern boundary faults of the Kızıltepe LS epithermal deposits are reactivated structures with and early phase of dextral motion and a lager stages of normal faulting

with sinistral component. The tectonic significance and role of these structures in vein forming and mineralizing events will be discussed in Discussion Chapter.

Figure 3.18. Field views from NE–SW-trending southeast-dipping syn-mineralizing dextral fault; north of Çaygören Dam with field ID 299; fault plane is 221°N/50°SE, R= 00°.

Figure 3.19. Field views from NE–SW-trending southeast-dipping almost pure normal fault; north of Çaygören Dam with field ID 307; fault plane is 235°N/74°SE, R= 85°N.

Figure 3.20. Field views from NE–SW-trending southeast-dipping syn-mineralizing normal fault with sinistral component; north of Çaygören Dam with field ID 308; fault plane is 060°N/42°SE, R= 42°E.
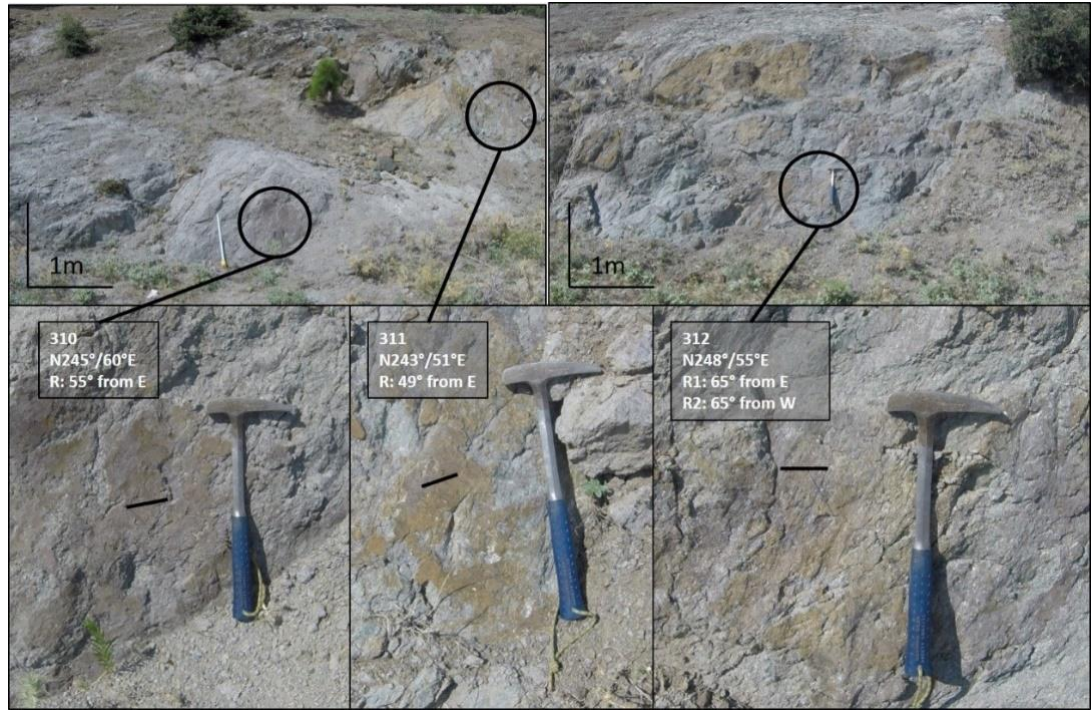
Figure 3.21. Field views from NE–SW-trending southeast-dipping syn-mineralizing normal fault with sinistral component; north of Çaygören Dam with field ID 310-312; fault planes are 245°N/60°SE, R_2= 55°NE; 243°N/51°SE, R_2= 49°NE; 248°N/65°SE, R_1= 65°SW and R_2= 65°NE. The fault planes on this outcrop suggest normal faulting with an early dextral and a later overprinting sinistral component.

3.5. Epithermal Veins

Kızıltepe LS epithermal deposit consists of several NNW–SSE- to WNW–ESE-trending subparallel epithermal auriferous quartz-adularia veins in association with its breccias and stockworks. Among these veins, Arzu South, Banu, Derya Main and Derya West are studied during this research (Figure 3.19 and 3.22).

Exploration and mining companies started to use unmanned aerial vehicles, more frequently known as drones, as a time and cost effective technique to obtain up to date high-resolution land images for target areas. In this study, a DJI Mavic Air Drone has been used to get the images of Arzu South open pit, Banu, Derya west and Derya main vein outcrops. The camera model was FC2103 with a resolution of 4056x3040 pixels.

The images have been processed by Pix4D which is photogrammetry software suite for georeferenced pictures. A total of 3,777 have been processed for all four selected vein systems (detailed reports in Appendix B).
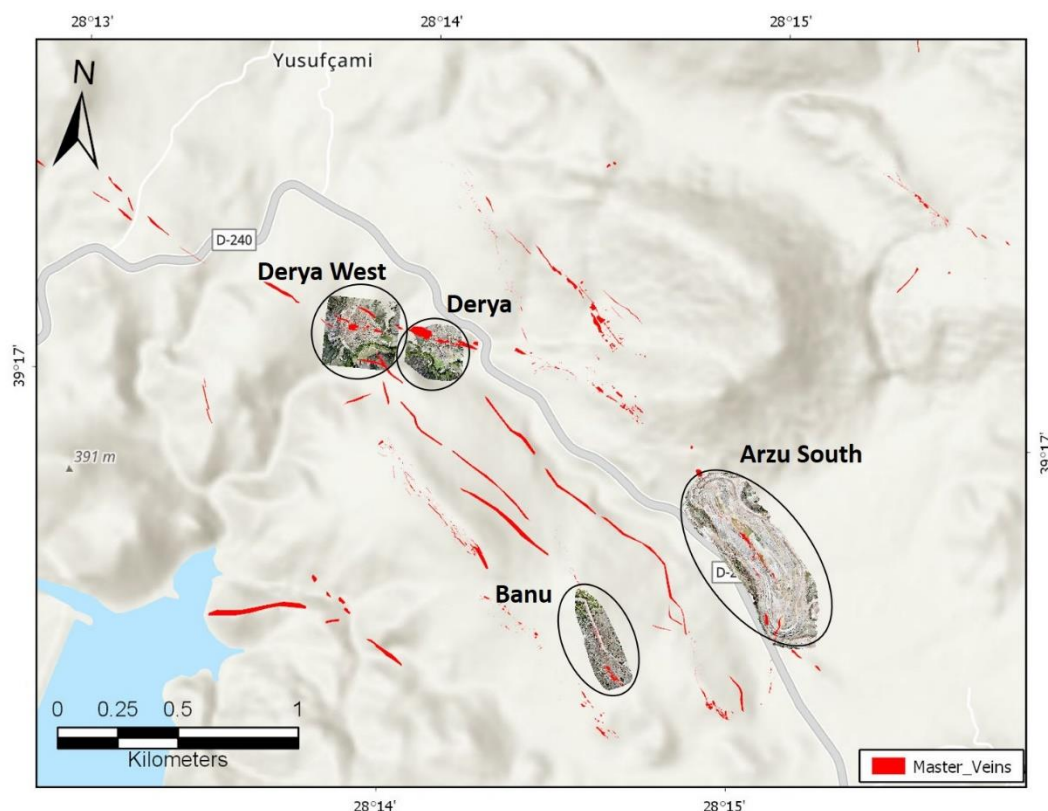
Figure 3.22. Location of the Arzu South, Derya, Derya West and Banu veins that have been selected for drone imagery in Kızıltepe district. Quartz vein outcrops shown in red.

2.5.1. Arzu South Vein

Arzu vein has a total 2,450 m length considering it continues under the pumice hill (rhyo-dacitic upper ignimbrites; Figure 2.10) where more exploration is required to define the gap between Arzu North and Arzu South sectors. Arzu South is the sector that has been defined as the highest tonnage and grade; therefore it is the first defined economic mineralization and mining has started in 2017.

Arzu South is a text book style low-sulfidation epithermal mineralization with the textures of chalcedony and crustiform banded Au-Ag vein. It is also common to observe lattice bladed texture as evidence of calcite replacement by quartz. The Au-

Ag distribution increases from surface to depth, thus supporting the idea of chalcedonic-lower temperature quartz at the near surface to occur at the top of the epithermal system.

The drill hole logging and open pit bench wall mapping exposes the primary mineralization caused alteration halo of disseminated sulfides, mostly pyrite, and clay minerals in the host rock of crystalline dacite. The contact of the vein in the footwall block in the west has higher sulfide mineral content, even massive pyrite zones occur at depth. Chalcedonic quartz turns into fine-grained milky quartz with ginguro spots and bands with the depth causing an increasing of Au and Ag grades. On the other hand, surface oxidation of the system, which is about 30 to 40 m from surface, changed the sulfide minerals into iron oxide minerals, mainly to hematite and goethite (Figure 3.23).
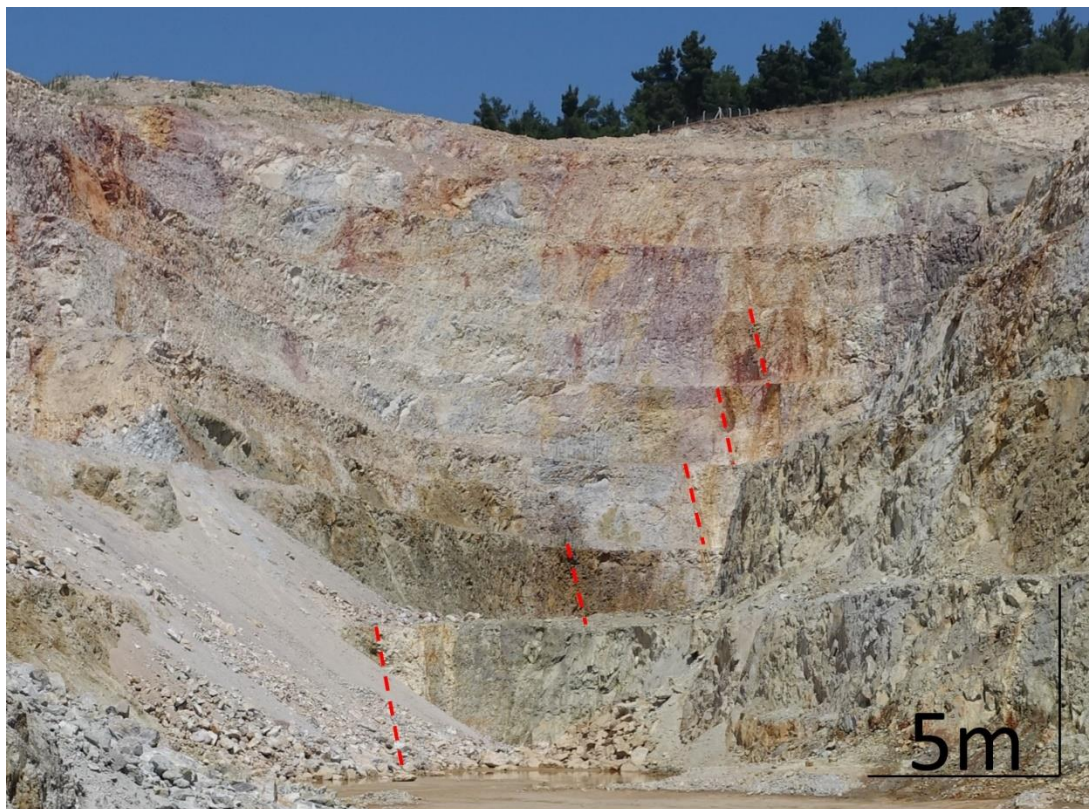
Figure 3.23. NW bench wall of the Arzu South open pit. Dip of the main mineralization and the contact of the footwall block is marked with red dashed line.

The steeply (78° to 81°) east dipping main Arzu South vein has a thickness of about 25 to 140 cm; there occurs a 15-m-wide mineralized zone associated with quartz breccias due to the reactivity of the vein-bounding fault after the precipitation of quartz and stockwork. A very interesting outcome of this study is to demonstrate that secondary veins both in the footwall and hanging wall of the Arzu South vein dips to the west where dip angles range between 58° and 85°. This is an important observation because the majority of the resource holes testing the target at a desired depth were drilled from east to west. These west-plunging holes have missed the subparallel west-dipping minor quartz veins with varying thickness of 1 to 23 cm. This further means underestimation of the resource during the feasibility study.
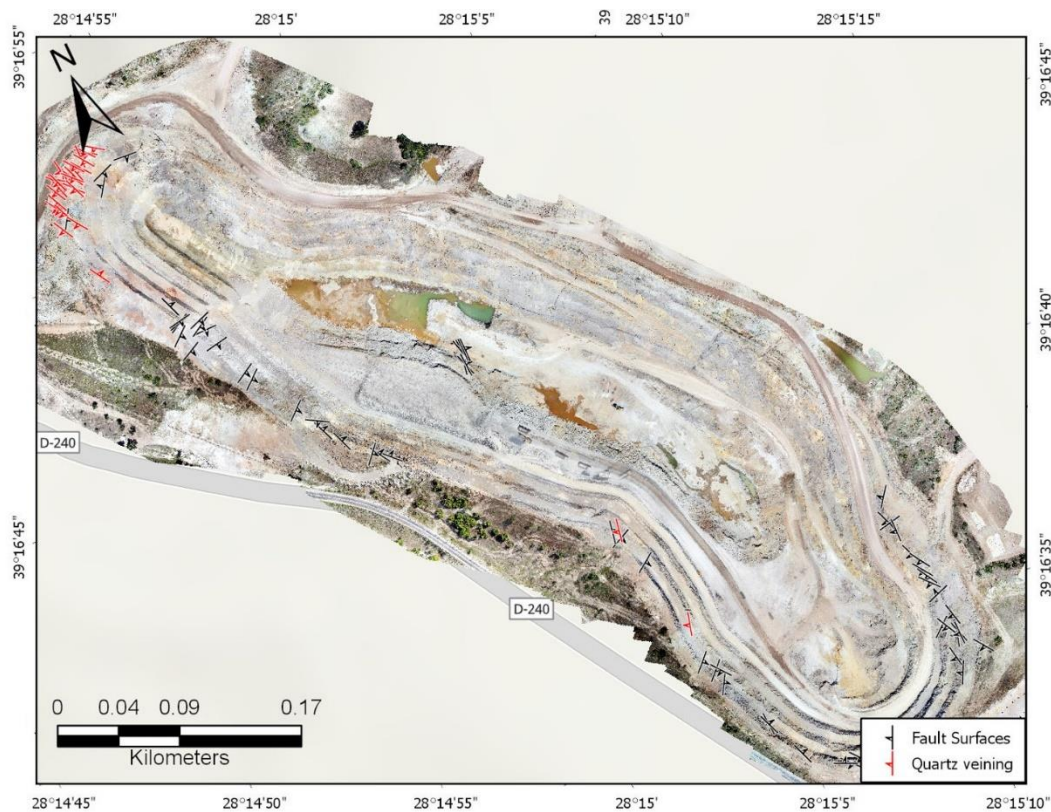
Figure 3.24. Drone imagery of the Arzu South open pit with the collected structural and quartz vein data.

Thousands of pictures have been collected and processed to obtain high resolution georeferenced images of the Arzu South open pit, Derya West vein, Derya Main vein

100

and Banu vein. A total of 2519 pictures have been collected and processed to obtain high resolution georeferenced image of Arzu South open pit (Figure 3.24).

2.5.2. Derya Vein

The clusters of epithermal veins along 1,600 m strike length at the west are grouped as Derya vein system. Even the gaps between these outcropping clusters haven't been tested until now, the elongation of them suggest its continuity. Derya is a roughly 280°N-trending steeply west dipping (80°–90°) vein with local 320°N intersecting veins. A total of 379 pictures have been collected and processed to obtain high resolution georeferenced image of Derya West vein, Derya Main vein (Figure 3.25).

Figure 3.25. Drone imagery of Derya West vein.

Massive chalcedony and glassy quartz are the dominant texture of this 2-m-wide vein system, suggesting quartz precipitation at very low temperatures, possibly at the top of the system. This further means trace level of Au and Ag grades in the vein.

101

However, micro-sulfide- bearing dark grey stringers at the middle of the outcrops increase the Au and Ag content (Figure 3.26).

A total of 180 pictures have been collected and processed to obtain high resolution georeferenced image of Derya Main vein (Figure 3.27).

Figure 3.26. Outcrop of the N320° striking vein at Derya West. Dark grey micro-sulfide bearing stringers have up to 4 ppm Au and 20 ppm Ag according to recent XRF survey.
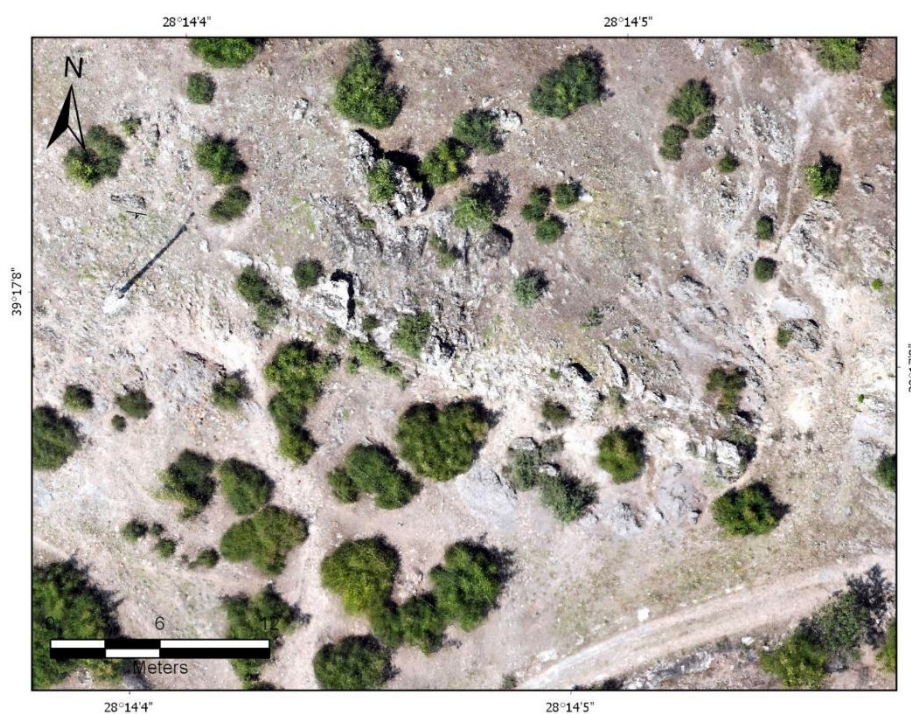
Figure 3.27. Drone imagery of Derya Main vein.

2.5.3. Banu Vein

The strike length of the Banu vein is about 900 m with a thickness of 1 to 6 m. General trend of the vein is 320°N, which is parallel to Arzu South vein; in fact it ranges between 313°N to 335°N. The steep vein dips to the west by 70° to 80° (Figure 3.28).

The outcrops of the Banu vein are characterized by banded chalcedony, open space and lattice bladed textures of quartz. Even though these quartz textures again suggest low temperature and shallow level of precipitation, geochemical analysis of surface rock/rock saw samples are modest compared to Derya.

Figure 3.28. Drone imagery of Banu vein.

The general orientation and the attitude of relatively smaller associated veins are studied in detail using these drone images. The veins are measured for further analysis (Table 3.1, Table 3.2, and Table 3.3). Attitude of the veins changes from one location to another due to undulating geometry of the veins. The stereoplot of the foliation data reflects two main orientations as ca. NW–SE and NNW–SSE, though the former orientation becomes dominant (Figure 3.29). The field observations confirm that the veins are generally parallel to the similarly trending normal faults. The computed

results of these veins (Figure 3.30) define a σ1 axis trending in 198°N direction with a steep plunge of 78°, whereas σ2 and σ3 axes are gently plunging at 03° and 11°, and trend in 303°N and 033°N, respectively. The results suggest an approximately NNE−SSW extension (Figure 3.30).

Table 3.1. *Dip direction and dip measurements at the north-western bench wall of the Arzu South open pit.*

Name	Easting	Northing	Elevation	Dip Direction	Dip
174	607673	4348911	381	W55	63
175	607672	4348905	383	W85	69
176	607669	4348905	382	W102	80
177	607667	4348900	385	W47	79
178	607664	4348898	384	W128	81
179	607662	4348891	383	W130	90
180	607660	4348888	385	W122	79
181	607661	4348886	385	W122	80
182	607663	4348883	386	W132	84
183	607658	4348872	387	W127	70
190	607701	4348915	359	W101	60
192	607695	4348914	359	W101	70
193	607694	4348915	359	W116	80
194	607694	4348915	359	E66	78
195	607691	4348910	361	W120	76
196	607687	4348906	361	W122	71
196A	607687	4348906	361	W118	75
196B	607687	4348906	361	E49	81
197	607683	4348909	360	W124	74
197A	607683	4348909	360	W117	82
198	607680	4348904	361	W134	74
199	607679	4348902	361	W122	78
199A	607679	4348902	361	W125	59
199B	607679	4348902	361	W111	85
200	607668	4348904	360	W116	70
200A	607668	4348904	360	W127	59
200B	607668	4348904	360	W113	60
200C	607668	4348904	360	W134	64
201	607677	4348895	362	W114	64
201A	607677	4348895	362	W133	71
202	607669	4348872	362	W121	69
203	607672	4348835	362	E34	80

Table 3.2. *Location, strike and dip measurements of Derya vein.*

Name	Easting	Northing	Elevation	Strike	Dip
265	606503	4349383	334	N280	82W
267	606161	4349421	333	N295	79W
268	606159	4349421	332	N314	88W
269	606146	4349425	328	N297	80W
270	606159	4349414	331	N328	80E

Table 3.3. *Location, strike and dip measurements of Banu vein.*

Name	Easting	Northing	Elevation	Strike	Dip
257	607263	4348271	396	N331	72W
258	607264	4348268	396	N335	80W
259	607289	4348213	389	N313	77W
260	607325	4348150	387	N316	72W
261	607334	4348115	388	N320	70W
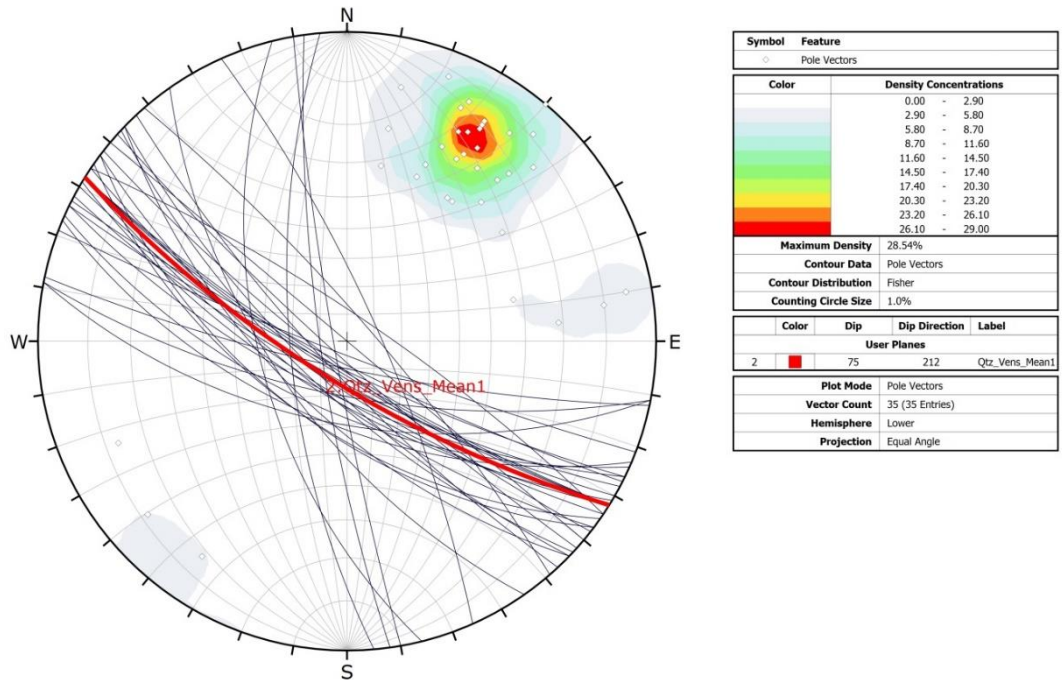
Figure 3.29. Contour graph of the *associated* poles to the vein planes, showing the best fit great circles. The diagram illustrates one dominant vein orientation in the Kızıltepe LS epithermal deposit. Mean attitude of the faults is 302°N, 75°NE.
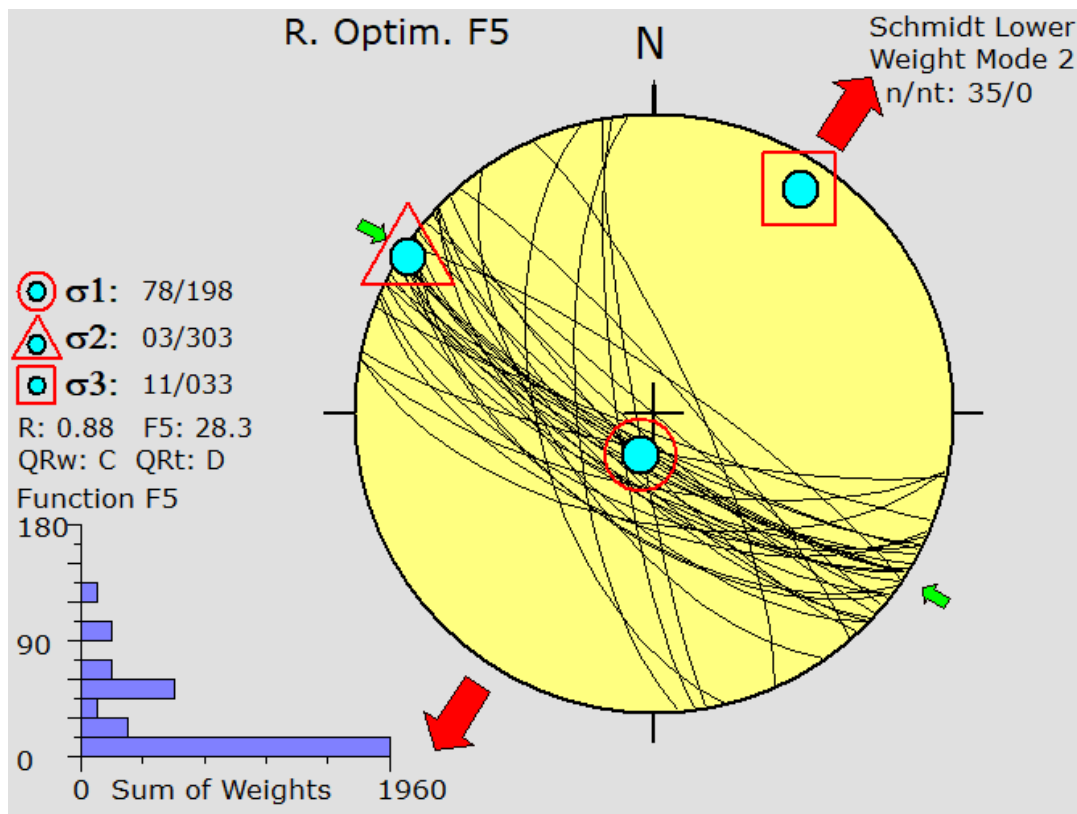
Figure 3.30. Schmidt lower hemisphere equal-area projections show stress inversion of vein data from the Kızıltepe LS epithermal deposit.

CHAPTER 4

DISCUSSION
PALEOSTRESS ANALYSIS AND INTERPRETATION

Attitude of fault planes are measured, where available the orientation of the slickenlines (rake) are noted and the relative sense of motion along the fault plane is interpreted. Collected structural data are filtered and paleostress analyses are carried out by using Win-Tensor and Dips software; the raw data is presented in Appendix A. The Win-Tensor is interactive software for determining tectonic stress from information in structural geology, neotectonic and seismotectonic investigations from geological fault-slip systems. Orientation of the three principal stress axes and the shape ratio of the stress ellipsoid of the reduced paleostress can be reconstructed.

The fault kinematic analysis using the data from striated slip surfaces are performed in order to determine the kinematic framework of faulting. The fault slip data are analyzed, using the stress inversion method of Angelier (1990), and computed using the Win-Tensor software. The inverse analysis of fault-slip data allows to determining stress orientation from measurements of fault slip data. All inversion results include the orientation (plunge and azimuth) of the maximum (σ_1), intermediate (σ_2), and minimum (σ_3) compressional principal stress axes as well as a 'stress ratio (φ)' [$\varphi = (\sigma_2 - \sigma_3) / (\sigma_1 - \sigma_3)$]', a linear quantity describing relative stress magnitudes.

I have studied the stress field orientations using the observed slip surfaces along the strike of the ca. E–W-trending northern boundary faults (Domain A) and the southern boundary faults (Domain B), and NW–SE-trending normal faults observed within the Arzu South vein pit (Figure 4.1). The results will be summarized below. The results are presented in lower-hemisphere stereoplots with a principal stress axes. It is important to emphasize that inversion techniques are applied to the fault sets with a limited number of data and their significance therefore needs to be used with care.
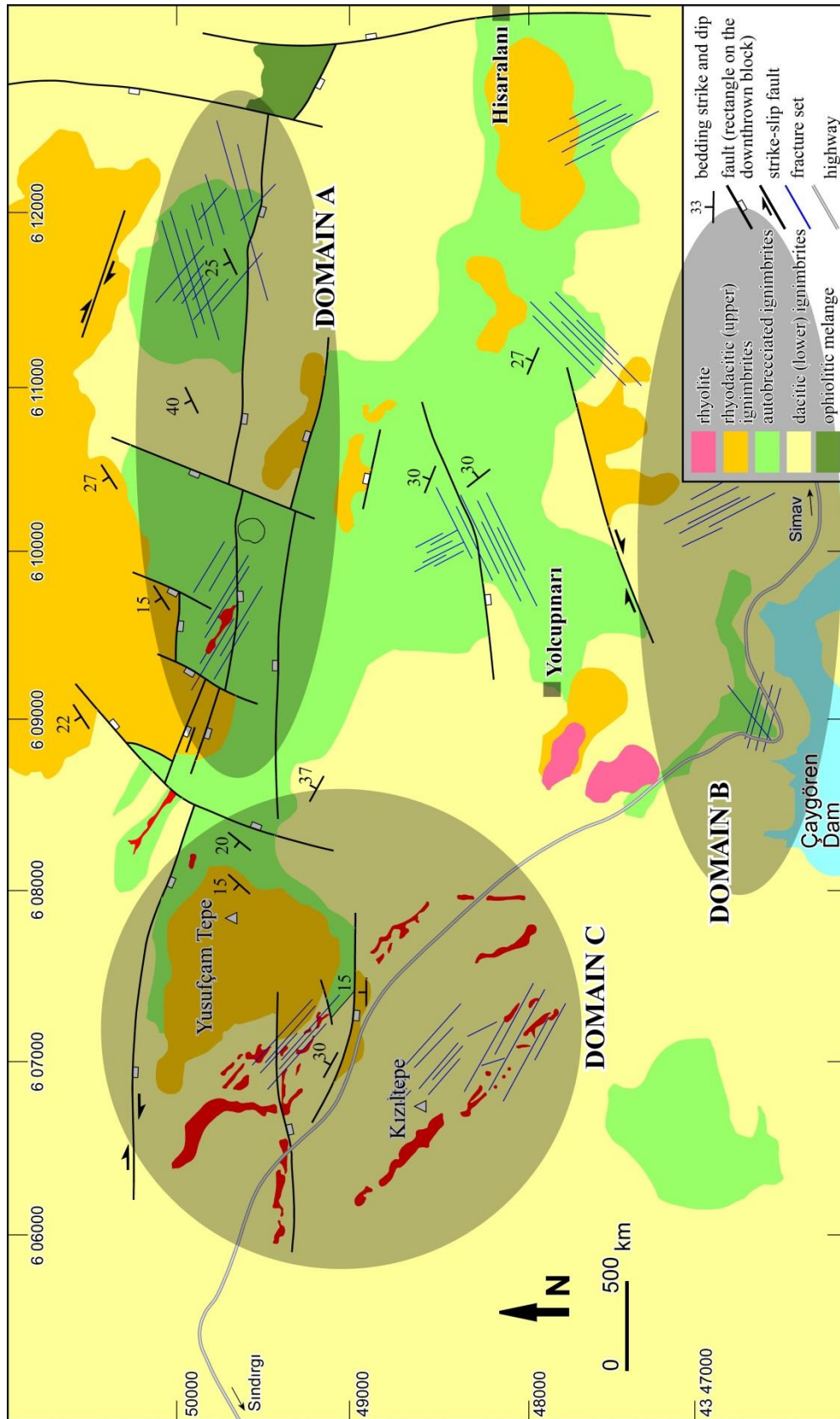
Figure 4.1. Geologic map of the Kızıltepe LS epithermal Au-Ag deposits and its surroundings (redrawn from Yılmaz *et al.* 2013). The location of three defined domains are also shown.

4.1. Domain A: Northern Boundary Faults

These faults display evidence for two sets of slip lines, indicating that they are reactivated structures. An early phase of dextral motion is overprinted by normal faulting with minor sinistral component. The stereoplot of the fault data reflects one main orientation; the mean attitude is 070°N, 61°S. (Figure 4.2). The computed results of the early dextral motion (Figure 4.3) define a $\sigma 1$ axis trending in 314°N direction with a moderate plunge of 43°, whereas $\sigma 2$ and $\sigma 3$ axes are relatively gently plunging at 36° and 26°, and trend in 160°N and 351°N, respectively (Figure 4.3). The results suggest an approximately NNE−SSW extension.

The fault-slip data from the younger normal motion with sinistral component are also analyzed. The calculated $\sigma 1$ trends in 307°N and plunges steeply at 85°, whereas $\sigma 2$ and $\sigma 3$ axes have average attitudes of 03°/085°N and 03°/175°N (Figure 4.4). These results are consistent with an approximately N−S extension.
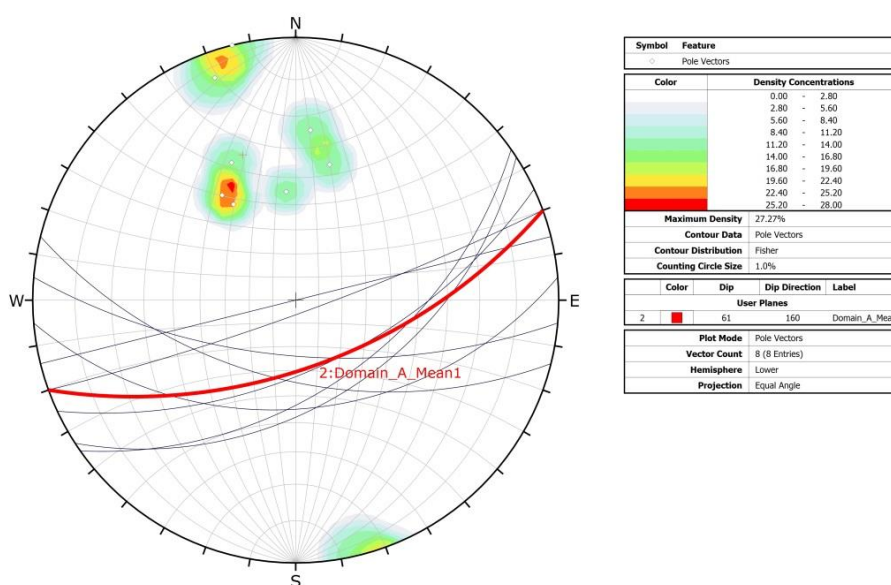
Figure 4.2. Stereonet and contour graph of the great circles and associated poles to the northern boundary fault planes, showing the best fit great circle. The diagram illustrates one dominant fault orientation; mean attitude of the faults is 070°N, 61°S.

4.2. Domain B: Southern Boundary Faults

These faults also display evidence for two sets of slip lines, indicating that they are reactivated structures. An early phase of dextral motion is overprinted by normal faulting with minor sinistral component. The stereoplot of the fault data reflects one main orientation; the mean attitude is 068°N, 55°S. (Figure 4.5); the strike direction is almost identical with those of the northern boundary faults. The computed results of the inverse analysis of fault-slip measurements define moderately plunging σ1 and σ2 axes (46° and 43°, respectively) and almost horizontal σ3 axes (04°); the trends are 036°N, 224°N and 130°N, respectively (Figure 4.6). The results are consistent with an approximately NW−SE extension.
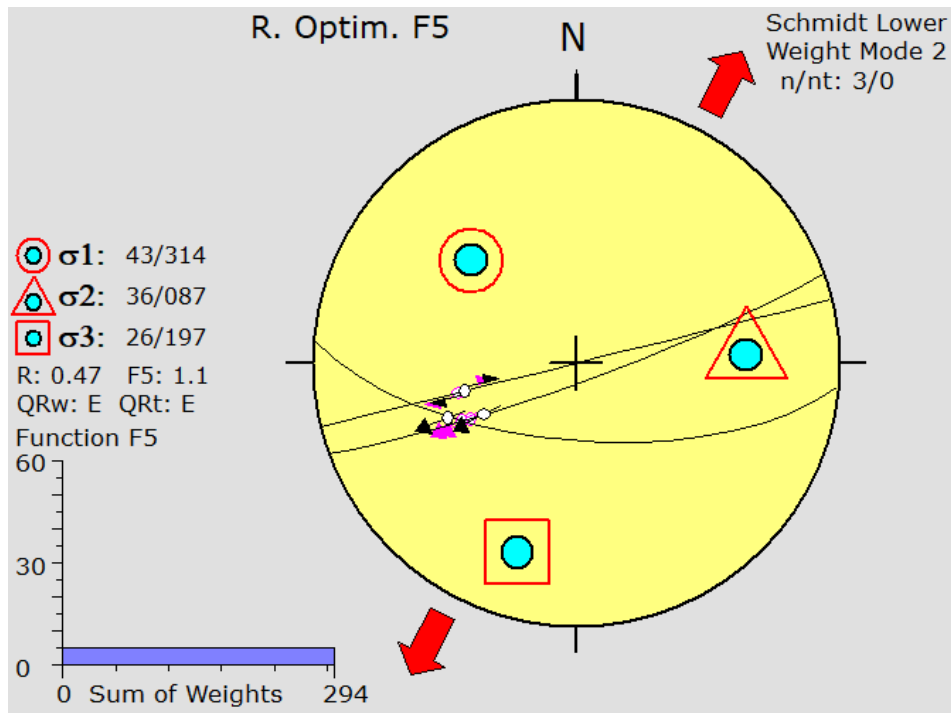
Figure 4.3. Schmidt lower hemisphere equal-area projections of the northern boundary fault planes to show stress inversion of the early dextral motion.

4.3. Domain C: Kızıltepe LS Epithermal Veins Site

This site represents the normal fault data collected from the Arzu South vein pit and other vein sites. The stereoplot of the fault data reflects two main orientations; the mean attitudes are 305°N, 57°NE and 317°N, 87°NE. (Figure 4.7); the strike direction is almost identical with those of the auriferous quartz-adularia veins. For this reason, these normal faults are interpreted as the active structures of gold mineralization. The N–S faults appear to be subordinate structures. Because the faults in the pit area are broadly divided into two directions as NW–SE and ca. N–S structures, the paleostress analyses are carried out accordingly (Figure 4.10).

The Domain C is important because it occurs within the common/overlapping area of both the northern and southern boundary faults. It is therefore important to see if there is a local stress anomaly and if it relates to the kinematics of the bounding faults.
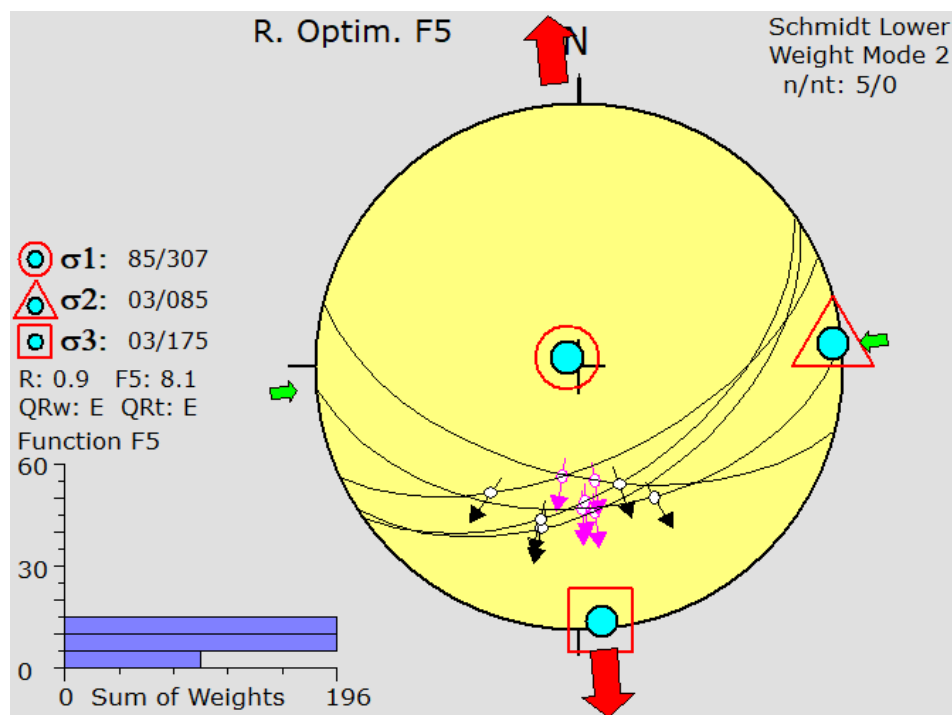
Figure 4.4. Schmidt lower hemisphere equal-area projections of the northern boundary fault planes to show stress inversion of the younger normal motion with sinistral component.
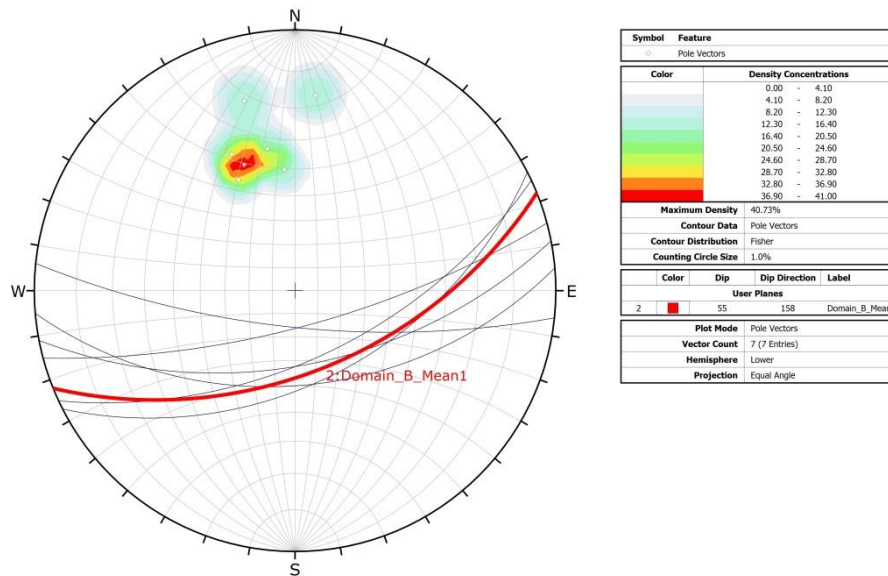
Figure 4.5. Stereonet and contour graph of the great circles and associated poles to the southern boundary fault planes, showing the best fit great circle. The diagram illustrates one dominant fault orientation; mean attitude of the faults is 068°N, 55°S.
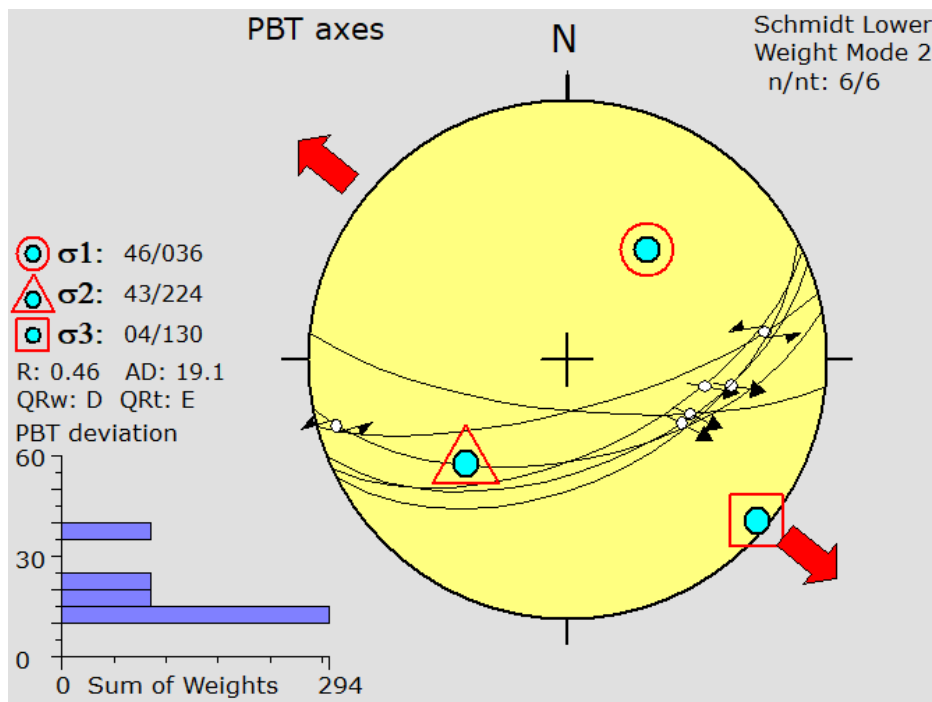
Figure 4.6. Schmidt lower hemisphere equal-area projections of the northern boundary fault planes to show stress inversion of the younger normal motion with sinistral component.

112
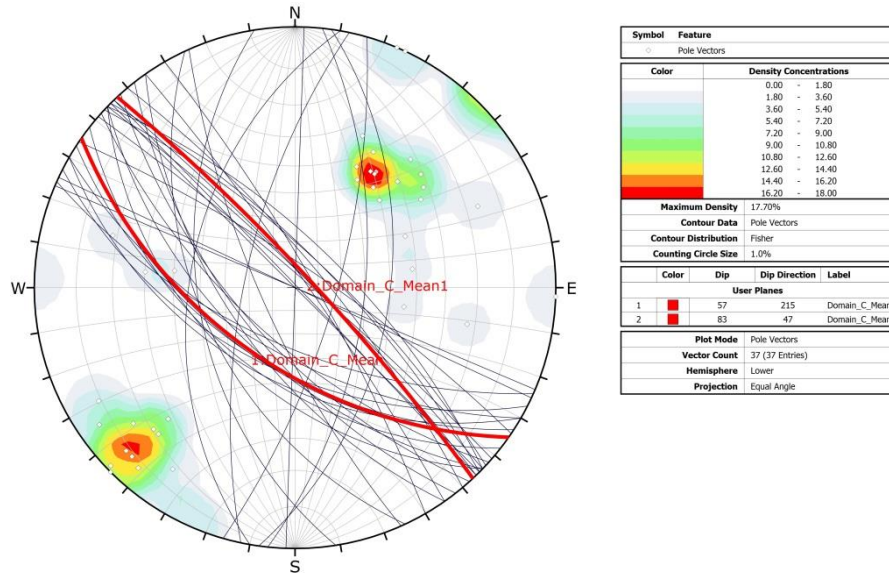
Figure 4.7. Stereonet and contour graph of the great circles and associated poles to the normal faults of the Arzu South vein pit showing the best fit great circle. The diagram illustrates two dominant fault orientations; mean attitudes are 305°N, 57°NE and 317°N, 87°NE.

The computed results of the inverse analysis of fault-slip measurements of the ca. N–S-trending faults indicates a gently plunging (14°) σ_1 that trends in 171°N direction. The calculated σ_3 is almost horizontal and has an average attitude of 05°/080°N. The and σ_2 axes plunges steeply at 75° in 329°N direction (Figure 4.8). These results are consistent with an approximately NNW–SSE compression and WSW–ENE extension.

Figure 4.8. Schmidt lower hemisphere equal-area projections to show stress inversion of fault-slip data from the ca. N–S-trending fault planes in the Arzu South vein pit.
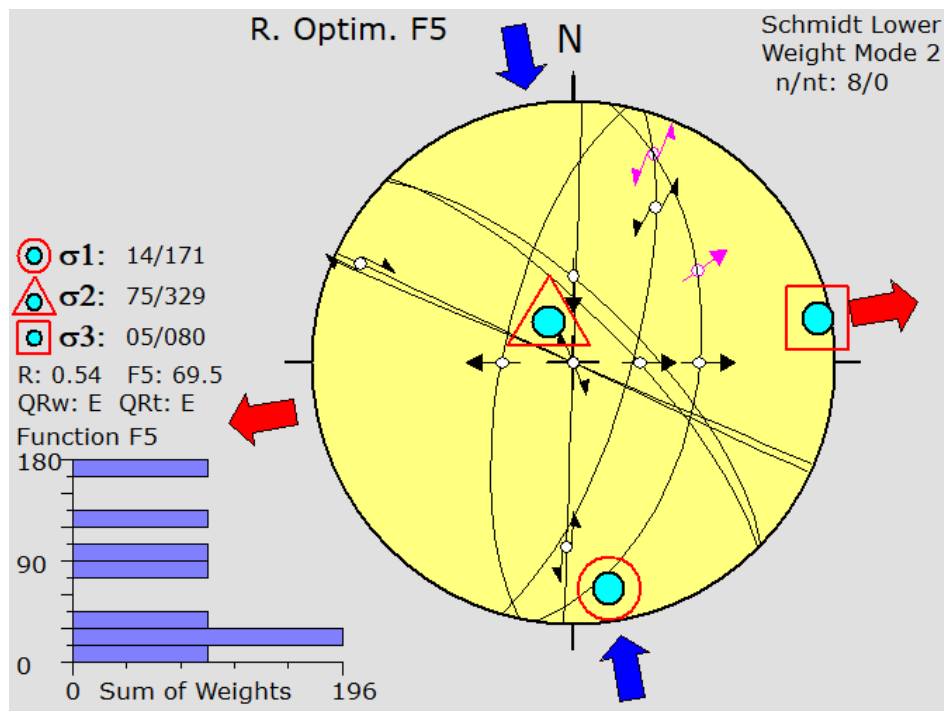
The computed results of the NW–SE normal faults in the Arzu South vein pit (Figure 4.9) define a σ1 axis trending in 071°N direction with a steep plunge of 65°, whereas σ2 and σ3 axes are relatively gently plunging at 14° and 20°, and trend in 308°N and 213°N, respectively (Figure 4.9). The results suggest an approximately NNE–SSW extension.

Similarly, the analysis of all measured faults in the pit area is also performed. The slip data define σ1, σ2 and σ3 axes with average attitudes of 71°/151°N, 19°/328°N and 01°/058°N (Figure 4.10). The calculated σ_1 is steeply plunging at 71°, whereas σ_3 axes is horizontal. The results suggest an approximately NE–SW extension.
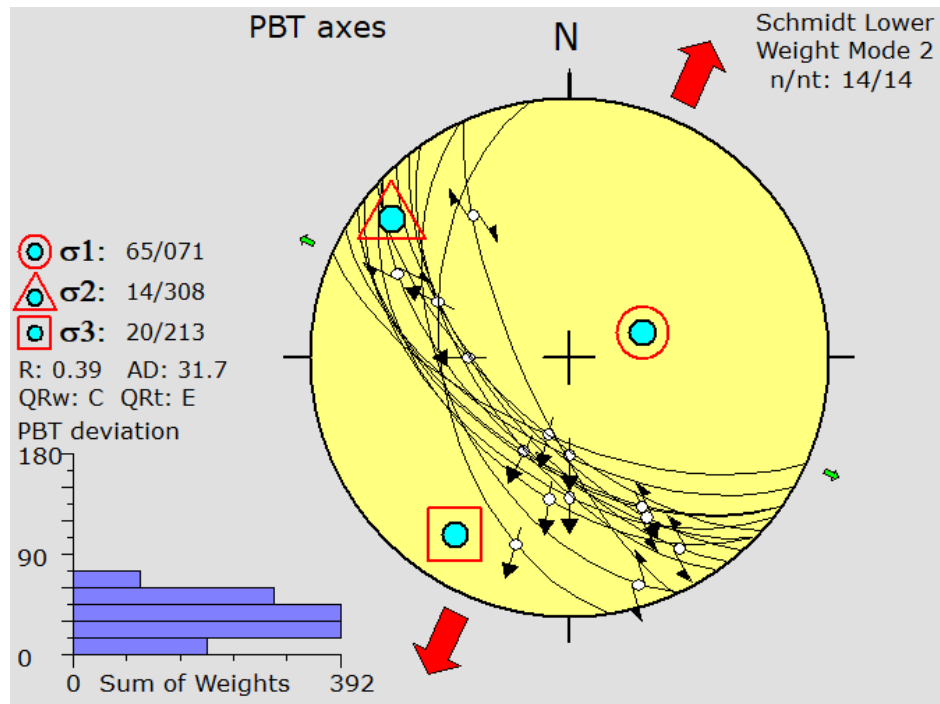
Figure 4.9. Schmidt lower hemisphere equal-area projections to show stress inversion of fault slip data from the ca. NW–SE-trending fault planes in the Arzu South vein pit.
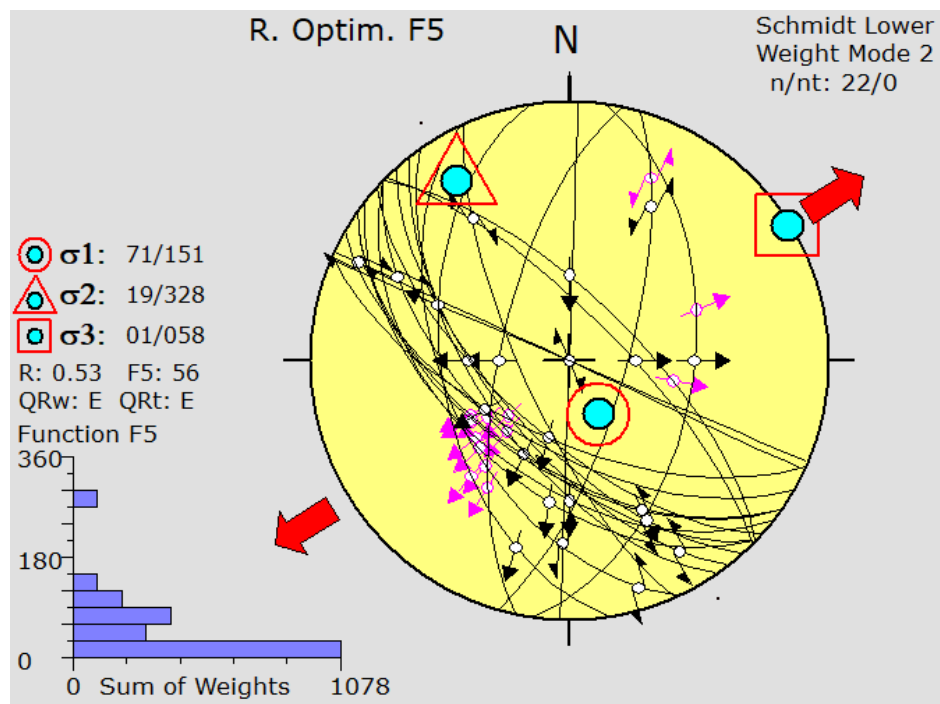
Figure 4.10. Schmidt lower hemisphere equal-area projections to show stress inversion of fault slip data from all fault planes in the Arzu South vein pit.

4.4. Geological Structures: Summary

The structural geology of the Kızıltepe low-sulfidation epithermal Au-Ag deposits is characterized by three distinct structures. Approximately E–W-trending and south dipping faults form the first group of structures. Observed fault planes are corrugated and the strike of the faults displays variations with pronounced undulations. Most planes are polished and contain parallel striations, ridge-and-groves and gutters that allow interpretation of the fault motion. These fault planes have two overprinting striations and the fault-slip data is consistent with two distinct stages of movement. The early motion is dextral with minor normal component. The faults are reactivated and moved as normal fault with sinistral component. They are interpreted as bounding structures of the Kızıltepe LS deposit. Similar faults are already described in the limited number of literature but no kinematic data is provided. There is only one single report of striations on one these faults (Akay 2007; Yılmaz *et al.* 2013); according to these authors the rake of striations is 20° from west and suggests a dextral motion with normal component. The dominant normal motion with relatively less sinistral component has therefore very important implications. The early motion dextral motion is consistent with ca. NNW–SSE extension while the later normal motion is consistent with approximately N–S and NW–SE extension.

The second group of structures are represented by NW–SE-trending auriferous quartz-adularia veins. They represent a swarm of several parallel veins, and associated with intense alteration and stockworks around their margins. The general orientation of these veins suggests a NE–SW-trending extension.

Third group is represented by NW–SE-trending normal faults, with subordinate N–S structures. Field observations confirm that these faults are parallel to the auriferous veins and occur along their margins. This relationship suggests that the faults and veins are genetically related and that the faults represent possible active structures of the mineralization. Inversion of the fault-slip data confirms NE–SW-trending extension during their formation.

116

4.5. A Working Model for Gold Mineralization

The stereoplot of the all fault data and the auriferous veins illustrates that mean orientations are: for bounding normal faults, 242°N, 56°SE; for vein-controlling normal faults, 303°N, 55°SW and 315°N, 81°NE; for auriferous veins, 302°N, 75°SW (Figure 4.11). The present geometry of the main bounding faults and, associated auriferous veins and normal faults indicates that these structures are almost orthogonal to each other. If these structures are genetically related, their relationship then can be explained by a typical relay ramp model, owing to the normal faulting along the main bounding structures (Figure 4.13).
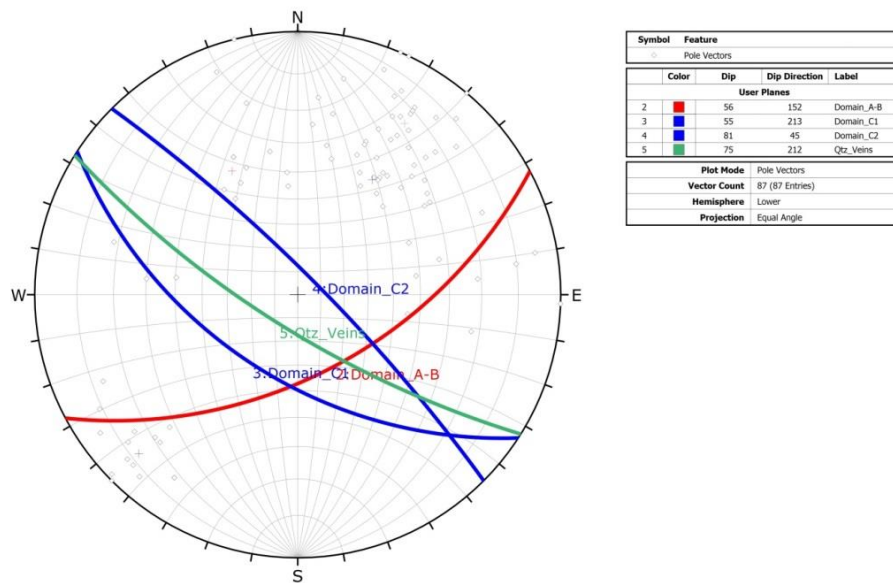
Figure 4.11. Stereonet and contour graph of the great circles of the best fit planes to the faults and veins in the study area.

The differential strain between overlapping normal fault zones in extensional terrains are accommodated by the relay ramps which may form in different scales. The development of the relay ramp start by the fault overlap and evolve to a fully breached fault. This is because of the strain accumulation in the fault overlap zone by the primarily bending of layers which followed by the formation of fractures and minor faults. Relay zones are (1) the lateral communication paths for fluid flow across

sealing faults, and (2) the conduits of vertical fluid flow which serve as the sites of ore deposits (Çiftçi & Bozkurt 2007; Fossen & Rotevant 2016).
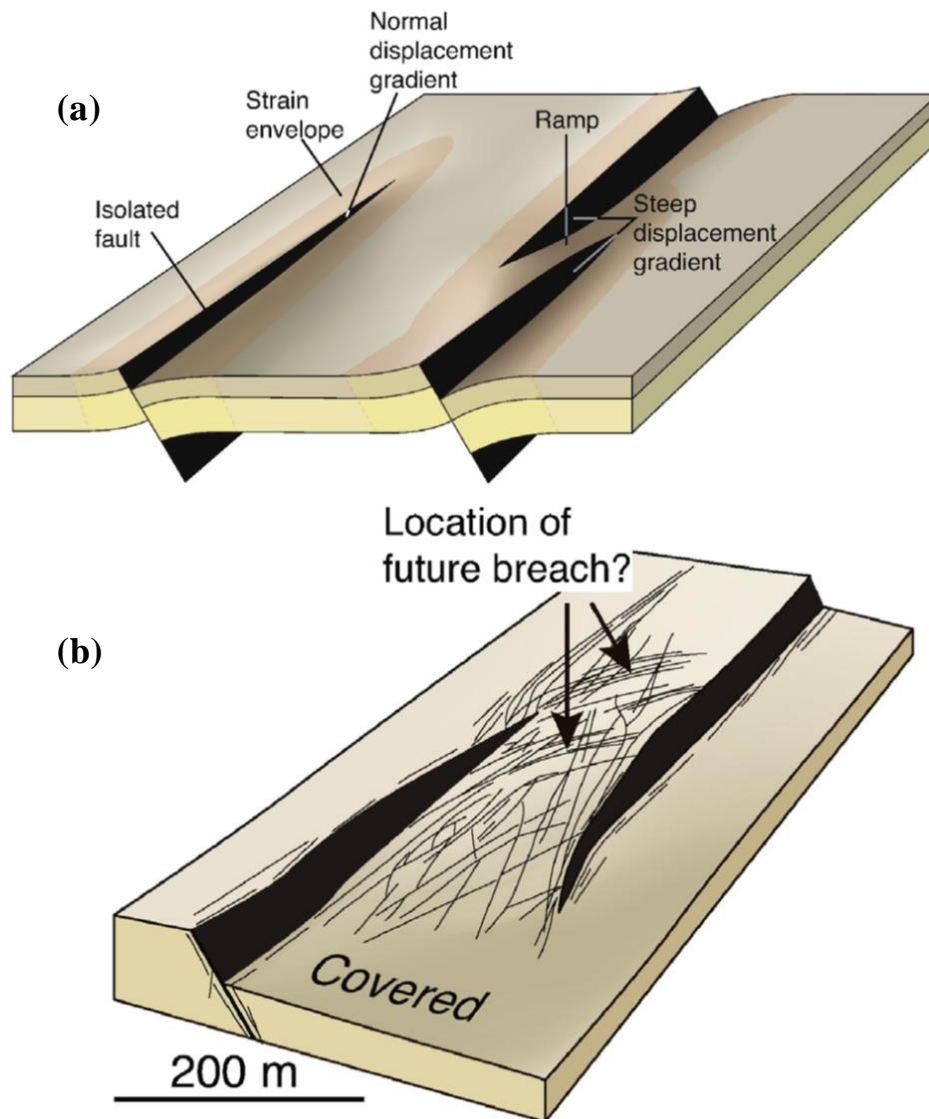
Figure 4.12: (a) A ramp connecting the hanging wall and footwall in a normal fault relay structure. In the left, an isolated fault is shown, and (b) An example of an unbreached ramp where the orientation and distribution of deformation bands in the ramp suggest that an upper-ramp breach was about to be established (from Fossen & Rotevant 2016).

In this model, the main bounding northern and southern faults reactivated isolated dextral structures that had little or no interaction between the segments. As the fault segments propagated towards each other, they began to interact and has resulted in the formation of a relay ramp, which connected to the footwall of one fault with the hanging-wall of the other. The relay ramp area acted as a transfer zone where displacement is transferred from one segment to the other. The deformation is localized in the ramp area and shows local extension almost orthogonal to the region direction. This localized deformation was accommodated by extensive fracturing and transverse faulting; this has resulted in the formation of an area where secondary fracture porosity and permeability has dramatically increased. The relay ramp area is finally broken and cut by breaching transverse faults and display increased structural complexity; increased deformation has result in the formation of numerous en echelon, overstepping normal faults formed in the region (Figure 4.14). This breached relay ramp became potential pathways for vertical migration of hydrothermal fluids from the active geothermal system. Thus, the region, relay ramp area became the location of fluid–rock interactive processes and formation of the Kızıltepe low-sulfidation epithermal gold mineralization of economic significance.
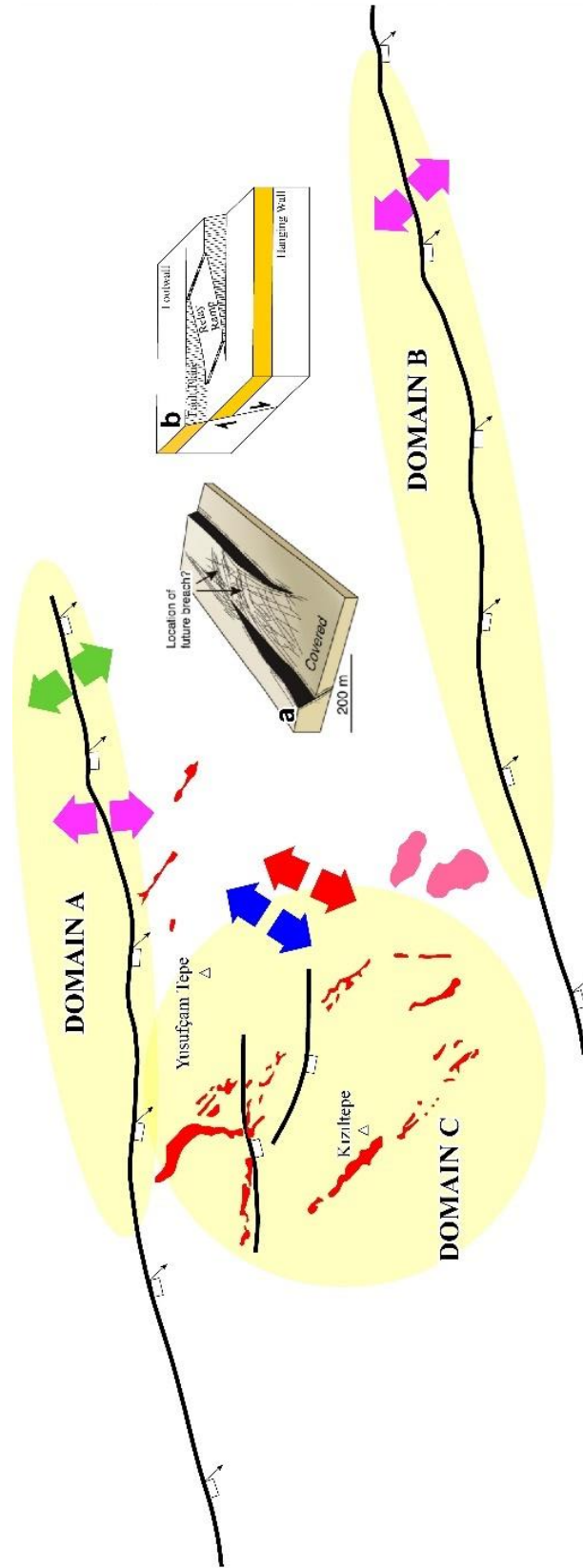
Figure 4.13. Relay ramp model for the structural setting of the Kızıltepe LS epithermal gold deposits. (a) model of a relay ramp illustrating intensive fracturing and faulting in the ramp area (from Fossen and Rotevatan 2017); (b) a block diagram illustrating a breached relay ramp (redrawn from Peacock & Sanderson 1994). The pink arrows indicated extension direction from inversion of fault-slip data; green arrows show inferred extension direction from inversion of auriferous veins and blue arrows, extension direction of vein-bounding normal faults.

In conclusion, it is suggested that the Kızıltepe gold deposits forms a typical example of a relay-ramp related low-sulfidation epithermal gold deposits in extensional terranes. This model needs further testing and necessitate collection more and detail structural data in and around the Kızıltepe deposits.
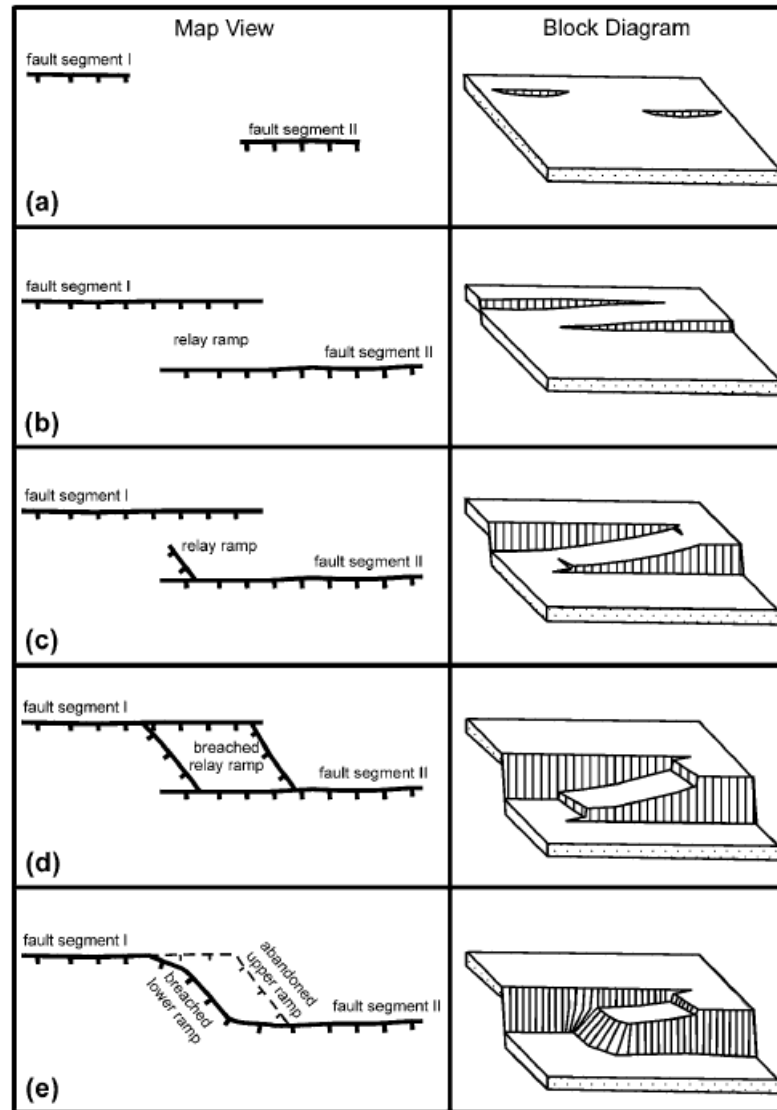
Figure 4.14. Schematic diagram showing evolutionary stages of a relay ramp (from Çiftçi and Bozkurt 2007). Tick marks on the map view depict the down-thrown block of normal faults. **(a)** Stage I: the faults do not interact. **(b)** Stage II: the faults have started to interact and a relay ramp has developed to transfer the displacement among the segments. **(c)** Stage III: accumulated strain in the relay ramp has resulted in initiation of fracturing. **(d)** Stage IV: the relay ramp is broken by a breaching fault to form a single fault zone with strike irregularity. **(e)** Upper bench is abandoned and two segments joined through breaching of lower ramp that form an along-strike bend on the course of the main fault.

REFERENCES

Akay, E. 2007. Geology of Kızıltepe Prospects and Surroundıngs (Sındırgı-Balıkesir). Galata Madencilik.

Akay, E. 2009. Geology and petrology of the Simav Magmatic Complex (NW Anatolia) and its comparison with the OligoMiocene granitoids in NW Anatolia: implications on Tertiary tectonic evolution of the region. Int Geol Rev, 98, 1655-1675.

Aldanmaz, E., Pickard, M., Meisel, T., Altunkaynak, Ş., Sayıt, K., Şen, P., Hanan, B.B., Furman, T., 2015. Source components and magmatic processes in the genesis of Miocene to quaternary lavas in western Turkey: constraints from HSE distribution and Hf-PbOs isotopes. Contrib. Mineral. Petrol. 170:23–42. doi:10.1007/s00410- 015-1176-x

Altunkaynak, Ş., Sunal, G., Aldanmaz, E., Genç, C. Ş., Dilek, Y., Furnes, H., . . . Yıldız, M. 2012. Eocene Granitic Magmatism in NW Anatolia (Turkey) revisited: New implications from comparative zircon SHRIMP U–Pb and 40Ar–39Ar geochemistry on magma genesis and emplacement. Lithos, 155, 289-309. doi:10.1016/j.lithos.2012.09.008

Asti, R., Malusà, M. G., Faccenna, C. 2018. Supradetachment basin evolution unravelled by detrital apatite fission track analysis: The Gediz Graben (Menderes Massif, Western Turkey). Basin Research, 30(3), 502–521. https://doi.org/10.1111/bre.12262

Asti, R., Faccenna, C., Rossetti, F., Malusà, M. G., Gliozzi, E., Faranda, C., Lirer, F., Cosentino, D. 2019. The Gediz Supradetachment System (SW Turkey): Magmatism, Tectonics, and Sedimentation During Crustal Extension. Tectonics, 38(4), 1414-1440. doi:10.1029/2018TC005181

Atabek, G., Altunkaynak, S. 2012. Geology and Petrogenesis of Bigadic-Sindirgi Volcanites, Western Turkey. European Geosciences Union (EGU). Vienna.

Blanks, D. 2013. Mineralogical and fluid characteristics of low sulphidation epithermal mineralisation in Kiziltepe project area, Balikesir, Western Turkey. Unpublished internal independent report on behalf of Ariana Resources.

Bozkurt, E. 2001. Neotectonics of Turkey – a synthesis. Geodinamica Acta, 14:1-3, 3-30. doi:10.1080/09853111.2001.11432432

Bozkurt, E. 2006. Metamorphic terranes of the Aegean region. Geodinamica Acta, 19:5, 249-250. doi:10.1080/09853111.2006.9736302

Bozkurt, E., Mittwede, S. K. 2001. Introduction to the Geology of Turkey - A Synthesis. International Geology Review, 43:7, 578-594. doi:10.1080/00206810109465034

Bozkurt, E., Mittwede, S. K. 2005. Introduction: Evolution of continental extensional. Geodinamica Acta, 18:3-4, 153-165. doi:10.3166/ga.18.153-165

Bozkurt, E., Park, R. G. 1994. Southern Menderes Massif: an incipient metamorphic core complex in western Anatolia, Turkey. Journal of the Geological Society, London, 151, 213-216.

Bozkurt, E., Rojay, B. 2005. Episodic, two-stage Neogene extension and short-term intervening compression in Western Turkey: field evidence from the Kiraz Basin and Bozdağ Horst. Geodinamica Acta, 18:3-4, 299-316. doi:10.3166/ga.18.299-316

Bozkurt, E., Satır, M., Buğdaycıoğlu, Ç. 2011. Surprisingly young Rb/Sr ages from the Simav extensional detachment fault zone, northern Menderes Massif, Turkey. Journal of Geodynamics, 52, 406-431.

Buchanan, L. J. 1981. Precious metal deposits associated with volcanic environments in the southwest. (W. R. Dickinson, W. D. Payne, Dü) Relation of tectonics to ore deposits in the South Cordillera. Ariz Geol Soc Digest, 14, s. 237-262.

Carman, C., Groves, I. 2013. Geology of the Red Rabbit Gold Project Sındırgı District, Balıkesir, Turkey. Balıkesir: Unpublished internal independent report on behalf of Ariana Resources.

Catlos, E. J., Baker, C., Sorensen, S. S., Hançer, M. 2010. Geochemistry, geochronology, and cathodoluminescence imagery of the Salihli and Turgutlu granites (central Menderes Massif, western Turkey): Implications for Aegean tectonics. Tectonophysics, 110-130. doi:10.1016/j.tecto.2009.06.001

Catlos, E. J., Shin, T. A., Speciale, P., Speciale, P., Yıldız, G. O., Black, K. 2012. Linked magmatic events in central Turkey: geochemistry and geochronology of the Beypazari and Sivrihisar granitoids. EGU General Assembly 2012, held 22-27 April, 2012 in Vienna, Austria, (s. 2497).

Çemen, İ., Helvacı, C., Ersoy, E. Y. 2014. Cenozoic extensional tectonics in western and central Anatolia,. Tectonophysics, 635, 1-5.

Çiftçi, N. B., Bozkurt, E. 2007. Anomalous stress field and active breaching at relay ramps: a field example from Gediz Graben, SW Turkey. Geol. Mag. 144 (4), 687–699.

Çiftçi, N. B. 2013. In-situ stress field and mechanics of fault reactivation in the Gediz Graben, Western Turkey. Journal of Geodynamics, 65, 136-147.

Çiftçi, N. B., Bozkurt, E. 2008. Folding of the Gediz Graben fi ll, SW Turkey: extensional and/or contractional origin? Geodinamica Acta, 21, 145–167.

Çiftçi, N. B., Bozkurt, E. 2010. Structural evolution of the Gediz Graben, SW Turkey: temporal and spatial variation of the graben basin. Basin Research, 22, 846-873. doi:DOI: 10.1111/j.1365-2117.2009.00438.x

Çoban, H., Karacık, Z., Ece, Ö. I. 2012. Source contamination and tectonomagmatic signals of overlapping Early to Middle Miocene orogenic magmas associated with shallow continental subduction and asthenospheric mantle flows in Western Anatolia: A record from Simav (Kütahya) region. Lithos, 140-141, 119-141.

Cohen, H. A., Dart, C. J., Akyüz, H. S., Barka, A. A. 1995. Syn-rift sedimentation and structural development of the Gediz and Büyük Menderes grabens, western Turkey. Journal of the Geological Society, London, 152, 629-638.

Coles, R. G. 2009. Geological mapping of exploration licenses for Ariana Resources plc and X-Ray diffraction analysis of clay samples to assess causes of alteration and relationship with hydrothermal activity. Sindirgi Gold Project, Western Turkey. Ariana Resources Plc and Cardiff University.

Cooke, D. R., Simmons, S. F. 2000. Characteristics and genesis of epithermal gold deposits. Reviews in Economic Geology, 13, 221-244.

Cooper, M. 2012. Kiziltepe IP Modelling. Core Geophysics.

Corbett, G. 2002. Epithermal Gold for Explorationist . AIG Journal – Applied geoscientific practice and research in Australia, 1-26.

Corbett, G. 2012. Structural Controls to, and Exploration for, Epithermal Au-Ag Deposits. Structural Geology and Resources (s. 43-47). Kalgoorlie WA: Australian Institute of Geoscientists.

Dilek, Y., Furnes, H., Shallo, M. 2007. Suprasubduction zone ophiolite formation along the periphery of Mesozoic Gondwana. Gondwana Research, 11(4), 453-475.

Ece, Ö. I., Ekinci, B., Schroeder, P. A., Crowe, D., Esenli, F. 2013. Origin of the Düvertepe kaolin–alunite deposits in Simav Graben, Turkey: Timing and styles of hydrothermal mineralization. 255, 57-78.

Emre, T. 1996. Geology and the Tectonics of the Gediz Graben. Turkish Journal of Earth Sciences, 5, 171-185.

Emre, T., Tavlan, M., Akkiraz, M., Işıntek, İ. 2011. Stratigraphy, sedimentology and palynology of the Neogene–Pleistocene(?) rocks around Akçaşehir-Tire-İzmir (Küçük Menderes Graben, Western Anatolia). Turkish Journal of Earth Sciences, 20, 27-56.

Erkül, F. 2010. Tectonic significance of synextensional ductile shear zones within the Early Miocene Alaçamdağ granites, northwestern Turkey. Geol Mag, 147(4), 611-637. doi:10.1017/S0016756809990719

Erkül, F., Helvacı, C., Sözbilir, H. 2005. Stratigraphy and Geochronology of the Early Miocene Volcanic Units in the Bigadiç Borate Basin, Western Turkey. Turkish Journal of Earth Sciences, 14, 227-253.

Erkül, F., Helvacı, C., Sözbilir, H. 2005. Evidence for two episodes of volcanism in the Bigadiç borate basin and tectonic implications for western Turkey. Geol. J., 40, 545–570

Erkül, F., Tatar-Erkül, S., Ersoy, Y., Uysal, İ., Klötzli, U. 2013. Petrology, mineral chemistry and Sr–Nd–Pb isotopic compositions of granitoids in the central Menderes metamorphic core complex: constraints on the evolution of Aegean lithosphere slab. Lithos, 180-181, 74-91. doi:10.1016/j.lithos.2013.07.022

Ersoy, E. Y., Akal, C., Genç, Ş. C., Candan, O., Palmer, M. R., Prelević, D., . . . Mertz-Krausd, R. 2017. U-Pb zircon geochronology of the Paleogene – Neogene volcanism in the NW Anatolia: Its implications for the Late Mesozoic-Cenozoic geodynamic evolution of the Aegean. Tectonophysics, 717, 284-301.

Ersoy, E. Y., Çemen, İ., Helvacı, C., Billor, Z. 2014. Tectono-stratigraphy of the Neogene basins inWestern Turkey: Implications for tectonic evolution of the Aegean Extended Region. Tectonophysics, 635, 33-58. doi:10.1016/j.tecto.2014.09.002

Ersoy, E. Y., Helvacı, C., Palmer, M. R. 2010b. Mantle source characteristics and melting models for the early-middle Miocene mafic volcanism in Western Anatolia: Implications for enrichment processes of mantle lithosphere and origin of K-rich volcanism in post-collisional settings. Journal of Volcanology and Geothermal Research, 198, 112-128.

Ersoy, E. Y., Helvacı, C., Palmer, M. R. 2011. Stratigraphic. structural and geochemical features of the NE-SW-trending Neogene volcano-sedimentary basins in western Anatolia: implications for association of supradetachment and transtensional strike-slip basin formation in extensional tectonic setting. Journal of Asian Earth Sciences, 41, 159-183.

Ersoy, E., Helvacı, C., Sözbilir, H. 2010a. Tectono-stratigraphic evolution of the NE–SW-trending superimposed Selendi basin: implications for late Cenozoic crustal extension in Western Anatolia, Turkey. Tectonophysics, 488, 210-232.

Evans, A. M. 1993. Ore geology and industrial minerals – An introduction. Oxford: Blackwell Scientific Publ.

Fossen, H., Rotevant, A. 2016. Fault linkage and relay structures in extensional settings—A review. Earth-Science Reviews, 154, 14-28.

Gemici, Ü., Tarcan, G. 2002. Hydrogeochemistry of the Simav geothermal field, western Anatolia, Turkey. Journal of Volcanology and Geothermal Research, 116, 215-233.

Glodny, J., Hetzel, R. 2007. Precise U-Pb ages of syn-extensional Miocene intrusions in the central Menderes Massif, western Turkey. Geological Magazine, 144, 235-246.

Göncüoglu, M. C. 2010. Introduction to the Geology of Turkey: Geodynamic Evolution of the Pre-Alpine. General Directorate of Mineral Research Exploration, Monography series 5, 1-66.

Hafeli, C. J. 1966. Hisaralan (Batı Anadolu) ılıcaları bölgesinde yapılan jeolojik ve hdrojeolojik etüdler. Maden Tetkik ve Arama Enstitüsü, 67, 110-118.

Hasözbek, A., Satir, M., Erdoğan, B., Akay, E., Siebel, W. 2011. Early Miocene post-collisional magmatism in NW Turkey: geochemical and geochronological constraints. International Geology Review, 53(9), 1098-1119. doi:10.1080/00206810903579302

Hedenquist, J. 1987). Mineralization associated with volcanic-related hydrothermal systems in the Circum Pacific basin. Circum-Pacific Energy and Mineral Ressources Conference.

Hedenquist, J. W., Arribas, A. 2017. Epithermal ore deposits: first-order features relevant to exploration and assessment. Mineral Resources to Discover - 14th SGA Biennial Meeting (s. 47-50). Quebec City.

Hedenquist, J. W., Lowenstern, J. B. 1994. The role of magmas in the formation of hydrothermal ore deposits. Nature, 370, 519-527.

Hedenquist, J. W., Arribas, A., Gonzalez-Urien, E. 2000. Exploration for epithermal gold deposits. Soc Econ Geol Rev, 13, 245-277.

Hedenquist, J. W., Izawa, E., Arribas, A., White, N. C. 1996. Epithermal gold deposits: styles, characteristics and exploration. Poster Soc Res Geol Sp Publ 1.

Henley, R. W., Ellis, A. J. 1983. Geothermal systems ancient and modern: a geochemical review. Earth Science Reviews, 19, 1-50. doi:10.1016/0012-8252(83)90075-2

Hinsbergen, D. J., Kaymakçı, N., W. S., Torsvik, T. H. 2010. Reconciling the geological history of western Turkey with plate circuits and mantle tomography. Earth and Planetary Science Letters, 297, 674-686.

Işık, V., Seyitoğlu, G., Çemen, İ., 2003. Ductile-brittle transition along the Alaşehir detachment fault and its structural relationship with the Simav detachment fault, Menderes Massif, western Turkey. Tectonophysics 374, 1–18.

Işık, V., Tekeli, O., Seyitoğlu, G., 2004. The 40Ar/39Ar age of extensional ductile deformation and granitoid intrusion in the northern Menderes core complex: implications for the initiation of extensional tectonics in western Turkey. Journal of Asian Earth Sciences 23, 555–566.

Karaoğlu, Ö. 2014. Tectonic controls on the Yamanlar volcano and Yuntdağı volcanic region, western Turkey: Implications for an incremental deformation. Journal of Volcanology and Geothermal Research, 274, 16-33.

Karaoğlu, Ö., Helvacı, C., Ersoy, E. 2010. Petrogenesis and 40Ar/39Ar geochronology of the volcanic rocks of the Uşak-Güre basin, western Türkiye. Lithos, 119, 193-210.

Kent, E., Boulton, S. J., Whittaker, A. C., Stewart, I. S., Alçiçek, M. C. 2017. Normal fault growth and linkage in the Gediz (Alaşehir) Graben, Western Turkey, revealed by transient river long-profiles and slope-break knickpoints. Earth Surface Processes and Landforms, 42(5), 836–852.

Kirkwood, C. 2012. Western Turkey exploration review, summer 2012: Analysis of rock chip and float sample assay data. Ariana Resources.

Küçükayman, A., Can, B., Çevikbaş, A., Ercan, T., Günay, E., Erkan, M., Ateş, M. 1984. The geology of Bİgadiç region: the petrology and genetic interpretations of the igneous rocks. Ankara: General Directorate of Mineral Research and Exploration.

Larcombe, G. 2012. Preliminary Report: Summer Work Placement. Unpublished internal report on behalf of Ariana Resources

Lindgren, W. 1922. A suggestion for the terminology of certain mineral deposits. Economic Geology, 17, 292-294.

Lindgren, W. 1933. Mineral Deposits (4th b.). New York: McGraw-Hill Book Co.

Moncada, D., Mutchler, S., Nieto, A., Reynolds, T. J., Rimstidt, J. D., Bodnar, R. J. 2012. Mineral textures and fluid inclusion petrography of the epithermal Ag–Au deposits at Guanajuato, Mexico: Application to exploration. Journal of Geochemical Exploration, 114, 20-35.

Morrison, H. F., Nichols, E. A., Torres-Verdin, C., Booker, J. R., Constable, S. C. 1990. Comparison of magnetotelluric inversion techniques on a mineral prospect in Nevada. SEG Annual Meeting. San Francisco, California.

Nilius, N.-P., Glotzbach, C., Wölfler, A., Hampel, A., Dunkl, I., Akal, C., Heineke, C., Hetzel, R. 2019. Exhumation history of the Aydın range and the role of the Büyük Menderes detachment system during bivergent extension of the central Menderes Massif, western Turkey. Geological Society of London, 176 (4), 704-726. doi:10.1144/jgs2018-162

Okay, A. I. 2008. Geology of Turkey: A Synopsis. Anschnitt, 19-42.

Öner, Z., Dilek, Y., Kadıoğlu, Y. K. 2010. Geology and geochemistry of the synextensional Salihli granitoid in the Menderes core complex, western Anatolia, Turkey. International Geology Review, 52, 373-408. doi:10.1080/00206810902815871

Öner-Baran, Z., Dilek, Y., Stockli, D. F. 2017. Diachronous uplift and cooling history of the Menderes core complex, western Anatolia (Turkey), based on new Zircon (U-Th)/He ages. Tectonophysics, 694. doi:10.1016/j.tecto.2016.12.005

Oygür, V. 1997. Anatomy of an epithermal mineralizaton: Mumcu (Balıkesir-Sındırgı), inner-western Anatolia. Turkey Mineral Research Exploration Bulletin, 119, 29-39.

Özen, Y., Arık, F. 2015. S, O and Pb isotopic evidence on the origin of the İnkaya (Simav-Kütahya) Cu–Pb–Zn–(Ag) Prospect, NWTurkey. Ore Geology Reviews, 70, 262-280.

Ozgenç, İ., İlbeyli, N. 2008. Petrogenesis of the Late Cenozoic Egrigöz Pluton in Western Anatolia, Turkey: Implications for Magma Genesis and Crustal Processes. International Geology Review, 50(4), 375-391.

Özkaymak, Ç., Sözbilir, H., Uzel, B. 2013. Neogene–Quaternary evolution of the Manisa Basin: Evidence for variation in the stress pattern of the İzmir-Balıkesir Transfer Zone, western Anatolia. Journal of Geodynamics 65, 117-135.

Pirajno, F. 1992. Hydrothermal Mineral Deposits. Berlin, Heidelberg: Springer. doi:10.1007/978-3-642-75671-9

Purvis, M., Robertson, A. 2005a. A puksed extension model for the Neogene-Recent E-W-trending Alaşehir graben and the NE-SW-trending Selendi and Gördes basins, W Turkey: IMplications for extensional processes. Sed. Feol., 174(1-2), 31-62.

Purvis, M., Robertson, A., Pringle, M. 2005b. 40Ar-39Ar dating of biotite and sanidine in tuffaceous sediments and related intrusive rocks: Implications for the Early Miocene evolution of the Gördes and Selendi basins, W Turkey. Geodinamica Acta, 18/3-4, 239-253. doi:10.3166/ga.18.239-253

Ring, U., Collins, A. S. 2005. U-Pb SIMS dating of synkinematic granites: timing of core complex formation in the northern Anatolide belt of western Turkey. Journel of the Geological Society, London, 301, 912-944.

Rossetti, F., Asti, R., Faccenna, C., Gerdes, A., Lucci, F., Theye, T. 2017. Magmatism and crustal extension: Constraining activation of the ductile shearing along the Gediz detachment, Menderes Massif (western Turkey). Lithos, 282, 145-162. doi:10.1016/j.lithos.2017.03.003

Sánchez, M. G., McClay, K. R., King, A. R., Wijbrams, J. R. 2016. Cenozoic Crustal Extension and Its Relationship to Porphyry Cu-Au-(Mo) and Epithermal Au-(Ag) Mineralization in the Biga Peninsula, Northwestern Turkey. Society of Economic Geologists, Special Publication 19, 113-156.

Sarıca, N. 2000. The Plio-Pleistocene age of Buyuk Menderes and Gediz grabens and their tectonic significance on N-S extensional tectonics in West Anatolia: Mammalian evidence from the continental deposits. Geological Journal, 35(1), 1-24. doi:10.1002/(SICI)1099-1034(200001/03)35:13.3.CO;2-1

Seghedi, I., Helvacı, C., Pecskay, Z. 2015. Composite volcanoes in the south-eastern part of İzmir-Balıkesir Transfer Zone, Western Anatolia, Turkey. Journal of Volcanology and Geothermal Research, 291. 72-85. doi: 10.1016/j.jvolgeores.2014.12.019

Semiz, B., Ersoy, E. Y., Özpınar, Y., Helvacı, C., Palmer, M. R., Billor, M. Z. 2015. Ar/Ar geochronology, geochemistry and petrology of volcanic rocks from the Simav Graben, western Turkey. Contrib Mineral Petrol, 170, 1-24. doi:10.1007/s00410-015-1178-8

Şener, K., Arar, M., Wedin, F., Goodman, S. 2009. Contrasting Styles of Epithermal Gold Mineralisation at the Kiziltepe and Tavsan Deposits, Western Turkey. Smart Science for Exploration and Mining, Proceedings of the Tenth Biennial SGA Meeting, Townsville, Australia (s. 848-850). Society for Geology Applied to Mineral Deposits, Geneva, Switzerland.

Şener, K., Menteş, B., Sarı, R., Saygılı, A., Tufan, V. 2006. Geological synthesis of epithermal gold deposits in the Sındırgı District, Balıkesir Province, Western Turkey. Workshop of IGCP-486, (s. 148-153). İzmir.

Seyitoğlu, G., Işık, V. 2015. Late Cenozoic Extensional Tectonics in Western Anatolia: Exhumation of the Menderes Core Complex and Formation of Related Basins. Bulletin of the Mineral Research and Exploration, 151, 47-106.

Seyitoğlu, G., Scott, B. 1991. Late Cenozoic crustal extension and basin formation in west Turkey. Geological Magazine, 128, 155-166.

Seyitoglu, G. and Scott, B.C. 1992. Late Cenozoic Volcanic Evolution of the Northeastern Aegean Region. Journal of Volcanology and Geothermal Research, 54, 157-176. doi: 10.1016/0377-0273(92)90121-S

Seyitoğlu, G., Scott, B. C. 1996. The cause of N-S Extentional Tectonics in Western Turkey: Tectonic escape vs back-arck spreading vs orogenic collapse. Geodynamics, 22, 145-153.

Seyitoglu, G., Isik, V., Cemen, I. 2004. Complete Tertiary exhumation history of the Menderes massif, western Turkey: an alternative working hypothesis. Terra Nova, 16, 358-364.

Sillitoe, R. H. 1993. Gold-rich porphyry copper deposits: geological models and exploration implications. Geol Ass Canada Spec Pap, 40, 465-478.

Sillitoe, R. H. 1999. Styles of high sulfidation gold, silver and copper mineralisation in porphyry and epithermal environments. PacRim Congress, (s. 28-44). 10-13 October 1999, Bali, Indonesia.

Sillitoe, R. H. 2015. Epithermal paleosurfaces. Mineralium Deposita, 50(7), 767-793. doi:10.1007/s00126-015-0614-z

Sillitoe, R. H., Hedenquist, J. W. 2003. Linkages between volcanotectonic settings, ore-fluid compositions and epithermal precious metal deposits. Soc Econ Geol Spec Publ, 10, 315-343.

Simmons, S. F., White, N. C., John, D. A. 2005. Geological characteristics of epithermal precious and base metal deposits. Econ Geol 100th Ann Vol, 485-522.

Sözbilir, H. 2001. Extensional tectonics and the geometry of related macroscopic structures: fi eld evidence from the Gediz detachment, western Turkey. Turkish Journal of Earth Sciences, 10, 51-67.

Sözbilir, H. 2002. Geometry and origin of folding in the Neogene sediments of Gediz graben, western Anatolia, Turkey. Geodinamica Acta, 15, 277-288.

Sözbilir, H., Sarı, B., Uzel, B., Sümer, Ö., Akkiraz, S. 2011. Tectonic implications of transtensional supradetachment basin development in an extension-parallel transfer zone: the Kocaçay Basin, western Anatolia, Turkey. Basin Research, 23, 423-448.

Stevens, D. 2012. Geology in the Kiziltepe area, Arzu Gap zone. Unpublished internal report on behalf of Ariana Resources.

Sümer, Ö., İnci, U., Sözbilir, H. 2013. Tectonic evolution of the Söke Basin: Extension-dominated transtensional basin formation in western part of the Büyük Menderes Graben, Western Anatolia, Turkey. Journal of Geodynamics 65, 148-175.

Taksavasu, T. 2017. Petrographic Analysis of Bonanza Epithermal Vein Textures at Buckskin National and Fire Creek Deposits, Northern Nevada. GSA Annual Meeting, (s. 65-1). Seattle, Washington, USA. doi:10.1130/abs/2017am-299537

Tatar-Erkül, S. 2012. Petrogenetic evolution of the Early Miocene Alaamda volcano-plutonic complex, northwestern Turkey: implications for the geodynamic framework of the Aegean region. International Journal of Earth Sciences, 101(1), 197-219. doi:10.1007/s00531-010-0632-0

Tepe Ç, Sözbilir H 2017. Tectonic geomorphology of the Kemalpaşa Basin and surrounding horsts, southwestern part of the Gediz Graben, Western Anatolia. Geodin Acta 29: 70-90.

Thomson, S. N., Ring, U. 2006. Thermochronologic evaluation of postcollision extension in the Anatolide orogen, western Turkey. Tectonics, 25, paper number TC3005.

Tosdal, R., Dilles, J. H., Cooke, D. R. 2009. From Source to Sinks in Auriferous Magmatic-Hydrothermal Porphyry and Epithermal Deposits. Elements, 5, 289-295. doi:10.2113/gselements.5.5.289

Ünal, A. and Altunkaynak, Ş. 2018. Nature and genesis of potassic high Ba-Sr granitoids associated with syn-convergent extension in NW Turkey. Lithos, 316-317, 261-277.

Uzel, B., Sözbilir, H., Özkaymak, Ç., Kaymakçı, N., Langereis, C. G. 2013. Structural evidence for strike-slip deformation in the İzmir–Balıkesir transfer zone and consequences for late Cenozoic evolution of western Anatolia (Turkey). Journal of Geodynamics, 65, 94-116.

van Hinsbergen, D. J. 2010. A key extensional metamorphic complex reviewed and restored: the Menderes Massif of western Turkey. Earth Science Reviews, 102, 60-76.

van Hinsbergen, D. J., Dekkers, M. J., Koç, A. 2010c. Testing Miocene Remagnetization of Bey Dağları: Timing and Amount of Neogene Rotations in SW Turkey. Turkish Journal of Earth Sciences, 19, 123-156.

van Hinsbergen, D. J., Dekkers, M. J., Bozkurt, E., Koopman, M. 2010a. Exhumation with a twist: Paleomagnetic constraints on the evolution of the Menderes metamorphic core complex, western Turkey. Tectonics, 29. doi:10.1029/2009TC002596.

van Hinsbergen, D. J., Kaymakcı, N., Spakman, W., Torsvik, T. 2010b. Reconciling the geological history of western Turkey with plate circuits and mantle tomography. Earth and Planetary Science Letters, 674-686.

Weatherley, D. K., Henley, R. W. 2013. Flash vaporization during earthquakes evidenced by gold deposits. Nature Geoscience. doi:10.1016/0375-6742(90)90063-G

White, N. C., Hedenquist, J. W. 1990. Epithermal environments and styles of mineralization: Variations and their causes, and guidelines for exploration. Journal of Geochemical Exploration, 36(1-3), 445-474. doi:10.1016/0375-6742(90)90063-G

White, N. C. and Hedenquist, J. W. 1995. Epithermal gold deposits: styles, characteristics and exploration. SEG Newsletter, 23, 1-13.

Yücel-Öztürk, Y. 2016. O, Sr and Nd Isotopic Constraints on Cenozoic Granitoids of Northwestern Anatolia, Turkey: Enrichment by Subduction Zone Fluids. Journal of African Earth Sciences 117, 12-28. doi: 10.1016/j.jafrearsci.2016.01.016

Yiğit, Ö. 2009. Mineral Deposits of Turkey in Relation to Tethyan Metallogeny: Implications for Future Mineral Exploration. Society of Economic Geologists, Inc. Economic Geology, 104, 19-51.

Yılmaz, H., F. N., Akay, E., Şener, A. K., Tufan, S. T. 2013. Low-sulfidation epithermal Au-Ag mineralization in the Sındırgı District, Balıkesir Province, Turkey. Turkish Journal of Earth Sciences, 22, 485-522.

APPENDICES

A. Raw Structural Data Used Paleostress Analyses

DOMAIN A

Fault-slip data			Input row data (User format)				Slip	Conf.	Weight	Activ.	Striae	Subset	Comments
	Properties		Orientation 1		Orientation 2		Sense	Level	Factor	Type	Intens.	Index	
Id	Format	Type	Ori1A	Ori1B	Ori2A	Ori2B							
1	13	1	84	160	57W		N	C	9.9	2	1	0.2	DOM_A
2	13	1	90	166	54W		N	C	9.9	2	2	0.2	DOM_A
3	13	1	60	155	49W		N	C	9.9	2	1	0.2	DOM_A
4	13	1	66	185	52W		N	C	9.9	2	1	0.2	DOM_A
5	13	1	45	175	72E		N	C	9.9	2	1	0.2	DOM_A
6	13	1	47	147	55S		N	C	9.9	2	1	0.2	DOM_A
7	13	1	52	145	55S		N	C	9.9	2	1	0.2	DOM_A
8	13	1	56	194	70E		N	C	9.9	2	1	0.2	DOM_A

DOMAIN B

Fault-slip data			Input row data (User format)				Slip	Conf.	Weight	Activ.	Striae	Subset	Comments
	Properties		Orientation 1		Orientation 2		Sense	Level	Factor	Type	Intens.	Index	
Id	Format	Type	Ori1A	Ori1B	Ori2A	Ori2B							
1	13	1	74	165	25E		S	C	9.9	2	1	0.2	DOM_B
2	13	1	74	186	50E		N	C	9.9	2	2	0.2	DOM_B
3	13	1	50	175	0		S	C	9.9	2	1	0.2	DOM_B
4	13	1	60	155	55E		N	C	9.9	2	1	0.2	DOM_B
5	13	1	51	153	49E		N	C	9.9	2	1	0.2	DOM_B
6	13	1	55	158	65E		N	C	9.9	2	1	0.2	DOM_B
7	13	1	58	169	10W		D	C	9.9	2	1	0.2	DOM_B

Compiled data Set 1 (Standard format)					Planes in Strike-Dip-Rake/Pitch format								Kinematic axes						WSM Regime			
Fault Plane		Slip Line		Slip	Plane 1				Plane 2				P	P	B	B	T	T	SHmax	Shmin	Regime	Regime
Dip	Dip-Dir	Azim.	Plunge	Sense	Strike	Dip	Rake	Pitch	Strike	Dip	Rake	Pitch	Azim.	Incl.	Azim.	Incl.	Azim.	Incl.	Azim.	Azim.	Code	Index
74	165	24	82	NS	75	74	-25	25					29	32	61	224	5	125	34	124	1.5	SS
74	186	47	114	NS	96	74	-50	50					45	47	39	263	19	157	60	150	0.5	NS
50	175	50	180	IS	85	50	87	87					5	177	2	87	84	331	177	87	2.5	TF
60	155	45	101	NS	65	60	-55	55					59	27	30	226	8	131	38	128	0.5	NF
51	153	36	99	NS	63	51	-49	49					59	38	31	214	2	305	36	126	0.5	NF
55	158	48	119	NS	68	55	-65	65					69	33	20	233	7	141	49	139	0.5	NF
58	169	8	254	ND	79	58	-171	9					28	297	57	152	16	36	122	32	1.5	SS

DOMAIN C

	Fault-slip data			Input row data (User format)				Slip	Conf.	Weight	Activ.	Striae	Subset	
	Properties			Orientation 1		Orientation 2		Slip	Conf.	Weight	Activ.	Striae	Subset	Comments
Id	Format	Type	Ori1A	Ori1B	Ori2A	Ori2B	Sense	Level	Factor	Type	Intens.	Index	
1	13	1	90	272	30S		S	C	9.9	2	1	0.2	DOM_C
2	13	1	68	282	90		N	C	9.9	2	2	0.2	DOM_C
3	13	1	70	44	0		D	C	9.9	2	2	0.2	DOM_C
4	13	1	75	45	90		N	C	9.9	2	2	0.2	DOM_C
5	13	1	50	98	90		N	C	9.9	2	2	0.2	DOM_C
6	13	1	72	106	35N		S	C	9.9	2	2	0.2	DOM_C
7	13	1	90	203	0		D	C	9.9	2	2	0.2	DOM_C
8	13	1	65	204	86E		N	C	9.9	2	2	0.2	DOM_C
9	13	1	90	205	11W		D	C	9.9	2	2	0.2	DOM_C
10	13	1	62	210	75NW		N	C	9.9	2	2	0.2	DOM_C
11	13	1	57	215	85S		N	C	9.9	2	2	0.2	DOM_C
12	13	1	56	215	45S		N	C	9.9	2	2	0.2	DOM_C
13	13	1	52	218	64S		N	C	9.9	2	2	0.2	DOM_C
14	13	1	67	222	90		N	C	9.9	2	2	0.2	DOM_C
15	13	1	50	224	65S		N	C	9.9	2	2	0.2	DOM_C
16	13	1	59	224	32N		D	C	9.9	2	2	0.2	DOM_C
17	13	1	66	228	35S		S	C	9.9	2	2	0.2	DOM_C
18	13	1	64	232	18S		S	C	9.9	2	2	0.2	DOM_C
19	13	1	61	235	52N		N	C	9.9	2	2	0.2	DOM_C
20	13	1	50	245	12S		S	C	9.9	2	2	0.2	DOM_C
21	13	1	75	246	35N		D	C	9.9	2	2	0.2	DOM_C
22	13	1	49	261	35S		S	C	9.9	2	2	0.2	DOM_C

QUARTZ VEINS

Fault-slip data			Input row data (User format)										
	Properties		Orientation 1		Orientation 2		Slip	Conf.	Weight	Activ.	Striae	Subset	Comments
Id	Format	Type	Ori1A	Ori1B	Ori2A	Ori2B	Sense	Level	Factor	Type	Intens.	Index	
1	13	4	78	66			T	C	9.9			0.2	qtz_Vein
2	13	4	81	49			T	C	9.9			0.2	qtz_Vein
3	13	4	80	34			T	C	9.9			0.2	qtz_Vein
4	13	4	80	262			T	C	9.9			0.2	qtz_Vein
5	13	4	85	260			T	C	9.9			0.2	qtz_Vein
6	13	4	63	235			T	C	9.9			0.2	qtz_Vein
7	13	4	69	265			T	C	9.9			0.2	qtz_Vein
8	13	4	80	192			T	C	9.9			0.2	qtz_Vein
9	13	4	79	227			T	C	9.9			0.2	qtz_Vein
10	13	4	81	218			T	C	9.9			0.2	qtz_Vein
11	13	4	90	220			T	C	9.9			0.2	qtz_Vein
12	13	4	79	212			T	C	9.9			0.2	qtz_Vein
13	13	4	80	212			T	C	9.9			0.2	qtz_Vein
14	13	4	84	222			T	C	9.9			0.2	qtz_Vein
15	13	4	70	217			T	C	9.9			0.2	qtz_Vein
16	13	4	60	191			T	C	9.9			0.2	qtz_Vein
17	13	4	70	191			T	C	9.9			0.2	qtz_Vein
18	13	4	80	206			T	C	9.9			0.2	qtz_Vein
19	13	4	76	210			T	C	9.9			0.2	qtz_Vein
20	13	4	71	212			T	C	9.9			0.2	qtz_Vein
21	13	4	75	208			T	C	9.9			0.2	qtz_Vein
22	13	4	74	214			T	C	9.9			0.2	qtz_Vein
23	13	4	82	207			T	C	9.9			0.2	qtz_Vein
24	13	4	74	224			T	C	9.9			0.2	qtz_Vein
25	13	4	78	212			T	C	9.9			0.2	qtz_Vein
26	13	4	59	215			T	C	9.9			0.2	qtz_Vein
27	13	4	85	201			T	C	9.9			0.2	qtz_Vein
28	13	4	70	206			T	C	9.9			0.2	qtz_Vein
29	13	4	59	217			T	C	9.9			0.2	qtz_Vein
30	13	4	60	203			T	C	9.9			0.2	qtz_Vein
31	13	4	64	224			T	C	9.9			0.2	qtz_Vein
32	13	4	64	204			T	C	9.9			0.2	qtz_Vein
33	13	4	71	223			T	C	9.9			0.2	qtz_Vein
34	13	4	69	211			T	C	9.9			0.2	qtz_Vein
35	13	4	58	256			T	C	9.9			0.2	qtz_Vein

Compiled data Set 1 (Standard format)					Planes in Strike-Dip-Rake/Pitch				Kinematic axes		WSM Regime			
Fault Plane		Slip Line		Slip	Plane 1				T	T	SHmax	Shmin	Regime	Regime
Dip	Dip-Dir	Azim.	Plunge	Sense	Strike	Dip	Rake	Pitch	Azim.	Incl.	Azim.	Azim.	Code	Index
78	66			TJ	336	78			12	246		246	1	TJ
81	49			TJ	319	81			9	229		229	1	TJ
80	34			TJ	304	80			10	214		214	1	TJ
80	262			TJ	172	80			10	82		82	1	TJ
85	260			TJ	170	85			5	80		80	1	TJ
63	235			TJ	145	63			27	55		55	1	TJ
69	265			TJ	175	69			21	85		85	1	TJ
80	192			TJ	102	80			10	12		12	1	TJ
79	227			TJ	137	79			11	47		47	1	TJ
81	218			TJ	128	81			9	38		38	1	TJ
90	220			TJ	130	90			0	40		40	1	TJ
79	212			TJ	122	79			11	32		32	1	TJ
80	212			TJ	122	80			10	32		32	1	TJ
84	222			TJ	132	84			6	42		42	1	TJ
70	217			TJ	127	70			20	37		37	1	TJ
60	191			TJ	101	60			30	11		11	1	TJ
70	191			TJ	101	70			20	11		11	1	TJ
80	206			TJ	116	80			10	26		26	1	TJ
76	210			TJ	120	76			14	30		30	1	TJ
71	212			TJ	122	71			19	32		32	1	TJ
75	208			TJ	118	75			15	28		28	1	TJ
74	214			TJ	124	74			16	34		34	1	TJ
82	207			TJ	117	82			8	27		27	1	TJ
74	224			TJ	134	74			16	44		44	1	TJ
78	212			TJ	122	78			12	32		32	1	TJ
59	215			TJ	125	59			31	35		35	1	TJ
85	201			TJ	111	85			5	21		21	1	TJ
70	206			TJ	116	70			20	26		26	1	TJ
59	217			TJ	127	59			31	37		37	1	TJ
60	203			TJ	113	60			30	23		23	1	TJ
64	224			TJ	134	64			26	44		44	1	TJ
64	204			TJ	114	64			26	24		24	1	TJ
71	223			TJ	133	71			19	43		43	1	TJ
69	211			TJ	121	69			21	31		31	1	TJ
58	256			TJ	166	58			32	76		76	1	TJ